University of Tennessee, Knoxville

TRACE: Tennessee Research and Creative Exchange

Doctoral Dissertations

Graduate School

5-2017

Creating and Operating the Nuclear Urban Kinetics Effects Simulator

Jerrad Phillip Auxier
University of Tennessee, Knoxville, jauxier1@vols.utk.edu

Follow this and additional works at: https://trace.tennessee.edu/utk_graddiss

Part of the Nuclear Engineering Commons

Recommended Citation

Auxier, Jerrad Phillip, "Creating and Operating the Nuclear Urban Kinetics Effects Simulator. " PhD diss., University of Tennessee, 2017.
https://trace.tennessee.edu/utk_graddiss/4379

This Dissertation is brought to you for free and open access by the Graduate School at TRACE: Tennessee Research and Creative Exchange. It has been accepted for inclusion in Doctoral Dissertations by an authorized administrator of TRACE: Tennessee Research and Creative Exchange. For more information, please contact trace@utk.edu.

To the Graduate Council:

I am submitting herewith a dissertation written by Jerrad Phillip Auxier entitled "Creating and Operating the Nuclear Urban Kinetics Effects Simulator." I have examined the final electronic copy of this dissertation for form and content and recommend that it be accepted in partial fulfillment of the requirements for the degree of Doctor of Philosophy, with a major in Nuclear Engineering.

Howard L. Hall, Major Professor

We have read this dissertation and recommend its acceptance:

Lawrence H. Heilbronn, Joseph R. Stainback IV, Thomas T. Meek

Accepted for the Council:

Dixie L. Thompson

Vice Provost and Dean of the Graduate School

(Original signatures are on file with official student records.)

Creating and Operating the Nuclear Urban Kinetics Effects Simulator

A Dissertation Presented for the

Doctor of Philosophy

Degree

The University of Tennessee, Knoxville

Jerrad Phillip Auxier

May 2017

Copyright © 2017 by Jerrad Phillip Auxier

All Rights Reserved.

Praise be to God and His Precious Son Jesus for giving me this small understanding of His creation and providing strength when I had none. Thanks to my father, John, and mother, Ruby, for providing me with the gift of education to my siblings, John David and Susanne, for all their support, encouragement, and love, and a special thanks to my loving family in Kentucky and Tennessee. Ya'lls prayers, love, guidance, and support are my greatest treasures.

Unless the Lord builds the house,
the builders labor in vain.
Unless the Lord watches over the city,
the guards stand watch in vain.
In vain you rise early
and stay up late,
toiling for food to eat—
for He grants sleep to those he loves….

Acknowledgements

I would first like to thank God and my Savior Jesus Christ for giving me the ability to understand a small portion of His creation. I would like to thank my father and mother, John and Ruby Auxier, for their undying support and love; I could not have completed this task without you. Thanks also to my brother and sister, John David and Susanne, you never stopped believing in me and would not allow me to stop until I had achieved what I thought I could not; and to the rest of my family in Kentucky and Tennessee, your constant prayers and support have kept me going.

I would especially like to thank my doctoral advisor, Dr. Howard Hall, for providing the resources and research motivation to accomplish this work. I would like to thank Dr. Joseph Stainback, Dr. Laurence Heilbronn, and Dr. Thomas Meek for being on my committee and providing me research insight for developing NUKES. A special thanks to Dr. John Auxier II for the daily research advice and encouragement to complete my research. The advice he gave on the project was priceless. I also want to thank my mentors Dr. Drew Kornreich and Dr. Adam Davis from Los Alamos National Labs (LANL) for the insight provided in creating this research project scope; their help was invaluable. They helped to improve the computational abilities of NUKES, and provide real application for my project. A special thanks for CPT Boone Gilbreathe, Dr. Matthew Cook, LTC Mike Shatton, and the members of the research group for providing daily support and insight in overcoming various research challenges. Thanks to Andy Giminaro for providing the groundwork needed to create this research project, and I would also like to thank my undergraduate research assistant Beau Badon for help in creating the libraries necessary for the completeness of the project; in order to complete this project, his assistance was essential and the work that he contributed to this project should be recognized.

Abstract

The ability to create an accurate method for determining the composition of post-detonation debris in an urban environment is an essential component of a proper nuclear forensics program. The methods necessary to create a high fidelity computer for modeling urban debris matrix creation is addressed. These methods include detonations varying in location in the lower 48 continental states and the yield of the weapon.

The ultimate goal of the research conducted in this area is to provide the nuclear forensics community with an effects modeling code that generates accurate urban surrogate recipes to be analyzed in laboratories. This code can be scaled to incorporate other blast scenarios that alter the final matrix composition.

Table of Contents

Chapter 1: Introduction and Motivation 1
Methodology 2
Energy Output 2
Thermal Effects 3
Chapter Summary 6
Chapter 2: Review of Current Nuclear Fallout Codes 7
Overview 7
Introduction 7
Code Overview 9
DELFIC (FPT) 11
HPAC 11
HYSPLIT 12
FDC 15
NARAC (KDFOC) 15
Code Validation Method 16
Results 20
Comparison of HPAC, HYSPLIT, DELFIC, and FDC 20
Comparison of HPAC and NARAC 25
Chapter Summary 26
Chapter 3: Soil Library Development 29
Overview of Chapter 29
Soil Composition Prediction 29
Crater Modeling 32
Chapter 4: Blast Effects Basics 37
Overview of the Chapter 37
Introduction 37
Varying Types of Bursts 39
Air Burst 39
Underwater Burst 40
Underground Burst 40

Surface Burst 41
Surface Burst Selection 41
Detonation Process 42
Neutron Production 42
Fission Fragments 45
Electron Production 47
Photon Production 48
Chapter Summary 50
Chapter 5: Blast Calculations 51
Introduction 51
Electron and Photon Energy Range 51
Photon Energy Deposition Calculations 54
Mean Free Path Assumptions 55
Chapter Summary 58
Chapter 6: Building Library 59
Overview of Chapter 59
Introduction 59
Making the Library 59
Adding the Skyscrapers 66
Adding Cars 67
Brick and Reinforced Concrete 67
Weighting Factor 67
Chapter 7: Utilizing Edge Finding Masks to find Urban Building Boundaries 70
Introduction 70
Automate Edge Finding Capabilities 70
Edge Finding Methods and Results 70
The Black and White Filter 72
The Sobel Method 74
The Prewitt Method 76
The Roberts Method 78
The Laplacian of Gaussian Method 80

The Canny Method 81
Chapter Summary 82
Chapter 8: Results 84
Chapter Overview 84
Soil Variation 84
Crater Size Variation 88
Annapolis Structure 92
Conclusion 105
List of References 107
Appendix 111
NUKES_Elements 117
NUKES_GE_Out 119
NUKES_Build_Comp 120
Vita 123

List of Tables

Table 2-1: Distribution of Nuclear Weapons Tests Worldwide[3] 8
Table 2-2: A short overview of prevalent nuclear fallout prediction codes 10
Table 2-3: Nuclear Fallout Prediction Capabilities of HYSPLIT 14
Table 2-4: Data from each nuclear test that was used in comparing the fallout codes [13] 20
Table 2-5: Compares the MOE for 3 different weather patterns to actual fallout data from the GEORGE test [16] 21
Table 2-6: Average NAD values for the codes for all nuclear tests simulated 27
Table 2-7: The average of all MOEx, MOEy, and NAD values from the 6 nuclear tests 27
Table 2-8: Average MOE values for NARAC and HPAC 30 minutes after release time [14] 28
Table 4-1: An overview of a Chemical Explosion versus Nuclear Explosion[23] 38
Table 4-2: Neutron population of a bare plutonium sphere with a 2cm reflector of U-238[23] 44
Table 4-3: The change of material phase depending upon the temperature and generation 45
Table 4-4: Shows the distribution of fission energy from either U-235 or Pu-239[23] 46
Table 4-5: The number of orbital shell electrons released from Pu atoms as a function of temperature [23] 48
Table 5-1: The thermal partition factor (f) for varying bursts [21] 58
Table 6-1: Shows the various buildings recognized by the EIA in an urban environment 60
Table 6-3: Shows the Data from a sample of buildings found in various cities. [26] 62
Table 6-4: Material composition of the buildings found in the specific cities (kg/m3 gross volume) [28] 63
Table 6-5: The material mass breakdown of these buildings [27] 64
Table 6-6: Actual numerical values of the buildings used in the model [27] 65
Table 6-7: The molecular composition of the selected buildings 69
Table 6-8: The elemental composition of the selected buildings 69
Table 8-1: The change in crater dimensions as a function of soil type. The crater volume calculation utilizes the varying soil densities to predict the volume of vaporized soil 92
Table 8-2: The composition difference between actual Trinitite and the debris output from NUKES 100
Table 8-3: The elemental differences between actual trinitite and NUKES' debris output prediction 101
Table 8-4: Table of debris composition vs crater depth. NUKES debris composition predictor based upon soil crater depth 102
Table 8-5: A molecular comparison between NUKES' deeper crater output and NUKES' shallow output with original tower modeled 104

List of Figures

Figure 1-1: Infrastructure in Hiroshima that survived under 0.5 miles from ground zero 2
Figure 1-2: The energy distribution from nuclear weapons 3
Figure 1-3: Damage areas from a nuclear detonation as modeled using DELFIC; blue is light damage, yellow is moderate damage, and red is severe damage 5
Figure 2-1: Time-Reversed Disc Tosser Model used in KDFOC3 16
Figure 2-2: Fallout areas that determine the accuracy of a code [16] 17
Figure 2-3: Prediction model demonstrating a changing of false positive values or false negative values, decreases in false positive values or false negative values is not a conclusive factor in determining fallout code accuracy [13] 18
Figure 2-4: NAD values associated with the isolines [16] 19
Figure 2-5: Actual Test Data from the George test [13] 22
Figure 2-6: GW method to predict the fallout pattern from the GEORGE test [13] 22
Figure 2-7: PRF method to predict the fallout pattern from the GEORGE test [13] 23
Figure 2-8: NAD value vs. Contours (Dose Rate) for the GEORGE nuclear test [13] 24
Figure 2-9: A comparison of NARAC and HPAC models when modeling the different gas types. The colors denote type of gas (Red=Stable, Blue=Neutral, and Green=Unstable), and the circle size demonstrates the changing dose rates modeled. A larger circle indicates more dose was modeled [14] 26
Figure 3-1: A soil profile with the depths of each horizon indicated [20] 30
Figure 3-2: Diagram of the Crater that is formed during a surface detonation[21] 32
Figure 3-3: Specific soil types versus changes in radius of crater[21] 34
Figure 3-4: Crater depth as a function of depth of burst and type of soil [21] 35
Figure 4-1: Distribution of energy from a fission style WMD [21] 39
Figure 4-2: A diagram of the gun type design of a fission weapon [22] 42
Figure 4-3: The initial reaction that kick-starts the fission reaction[23] 43
Figure 4-4: The fission fragment distribution from a prompt critical Plutonium apparatus[23] . 47
Figure 4-5: The Maxwell-Boltzmann distribution of particle speed during a fission detonation[23] 49
Figure 4-6: Fireball surface temperature as a function of time after a 20KT burst [23] 50
Figure 5-1: The Planckian energy distributions of photons emitted from a nuclear weapon at generations 40 and 41 [23] 52
Figure 5-2: The radiant power of black-body radiation as a function of wavelength, energy and temperatures [21] 53
Figure 5-3: The transmittance factor to a target on a clear day [21] 57
Figure 6-1: Mass ratio of each construction component for the modeled buildings 65
Figure 6-2: Diagram of the skyscraper model used for the buildings portion 66
Figure 7-1: Original format of the Google Earth image 71
Figure 7-2: Grayscale format of the Google Earth image 72
Figure 7-3: Google Earth image after the Poisson filter was applied 73

Figure 7-4: Google Earth Image after the Poisson filter was applied to change the image to black and white 73
Figure 7-5: Original grayscale image and the Strobel edge finding method 75
Figure 7-6: Original grayscale image and the Prewitt edge finding method 77
Figure 7-7: Original grayscale image and the Roberts edge finding method 79
Figure 7-8: Original grayscale image and the Laplacian/Gaussian edge finding method 80
Figure 7-9: Original grayscale image and the Canny edge finding method 82
Figure 8-1: Soil structure composition from the soil and the chemical molecules are actual rock stratus that can be found 85
Figure 8-2: Soil molecular composition. This is the molecules that can be added from the laboratory facilities 86
Figure 8-3: The elemental composition of the soil in Los Angeles, CA 86
Figure 8-4: The molecular composition of the soil in Knoxville, TN 87
Figure 8-5: The elemental composition of the soil in Knoxville, TN 87
Figure 8-6: Crater Dimensions of a 20kt blast in dry soil (Dry Soft Rock) 89
Figure 8-7: Crater Dimensions of a 20kt blast in wet soil (Wet Soft Rock) 89
Figure 8-8: Crater Dimensions of a 20kt blast in dry hard rock 90
Figure 8-9: Dimensions of a 20KT weapon detonated in wet hard rock 91
Figure 8-10: A simulated urban environment in which a 20KT fissile WMD was detonated 93
Figure 8-11: The elemental soil composition from Annapolis, MD 94
Figure 8-12: The elemental urban debris composition for Annapolis, MD 95
Figure 8-13: The molecular composition of the soil in Annapolis, MD 96
Figure 8-14: The molecular composition of the urban matrix from Annapolis, MD 97
Figure 8-15: The Trinity crater, where the darker area surrounding the crater is the trinitite glass 99
Figure 8-16: The tower on which the gadget was placed. 103

List of Acronyms used in Dissertation

USA – United States of America

NFAA – Nuclear Forensics Allocaion Act

NNSA – National Nuclear Security Agency

SSAP – Stewardship Science Academic Program

DHS – Department of Homeland Security

DELFIC – Department of Defense Fallout Prediction System

USDA – United States Department of Agriculture

KDFOC – K-Division Defense Nuclear Agency Fallout Code

NARAC – National Atmospheric Release Advisory Center

CTBT – Comprehensive Test Ban Treaty

FPT – Fallout Planning Tool

CRM – Cloud Rise Model

HPAC – Hazard Prediction and Assessment Capability

DTRA – Defense Threat Reduction Agency

NWI – Nuclear Weapon Incident

RWPN – Radiological WeaPoN

WMD -- Weapon of Mass Destruction

SCIPUFF – Second-Order Closure Integrated Puff

HYSPLIT – Hybrid Single Particle Lagrangian Integrated Trajectory

NOAA – National Oceanic and Atmospheric Administration

FDC – Fallout Dispersion Code

LLNL – Lawrence Livermore National Laboratories

ADAPT – Atmospheric Data Assimilation and Parameterization Tool

LODI – Lagrangian Operational Dispersion Integrator

GZ – Ground Zero

NTS – Nevada Test Site

HOB – Height of Burst

APR – Fallout Area Path

AOB – Area of the observed

AOV – Area of Overlap

AFN – Area of False Negatives

AFP – Area of False Positives

MOE – Measure of Effectiveness

NAD – Numerical Absolute Difference

DNA – Defense Nuclear Agency

HOB – Height of Burst

PRF –Average Weather Profile

GW – Ground Wind

KT- kiloton

SNM – Special Nuclear Material

NOAA -- National Oceanic and Atmospheric Administration

USDA -- United States Department of Agriculture

DELFIC -- Defense Land Fallout Interpretive Code

KDFOC -- K-Division Defense Nuclear Agency Fallout Code

NARAC -- National Atmospheric Release Advisory Center

DELFIC- FPT -- Defense Land Fallout Interpretative Code and Fallout Planning Tool

NUKES -- Nuclear Urban Kinetics Effects Simulator

DOB – Depth of Burst

IND – Improvised Nuclear Device

SNM – Special Nuclear Material

Chapter 1: Introduction and Motivation

Since the creation of nuclear weapons in the 1940's, the United States of America (USA) has worked to improve their nuclear forensics capabilities. These techniques include improvements in nuclear material characterization when interdicted material is found at border crossings, in the analysis of nuclear facilities to ensure that illicit nuclear material is not being created, and in the analysis of post-detonation debris. As part of post-detonation efforts, scientist are developing techniques to map fallout of surrogate melt glass from a nuclear detonation, and in shortening the analysis time required to properly characterize these samples.

To improve the US nuclear forensics capabilities, congress signed the Nuclear Forensics Allocation Act (NFAA). This act supplies funds to the Department of Homeland Security (DHS), the National Nuclear Security Agency (NNSA), and the Stewardship Science Academic Program (SSAP) to improve the nation's forensics capabilities. As stated, "…it is necessary to have a robust capability to acquire samples in a timely manner, analyze and characterize samples, and compare samples against known signatures of nuclear and radiological material."[1]

The NFAA's purpose for part of the increased funding is to shorten the analysis time of the surrogate melt glass that is created during a nuclear detonation. There are two steps to shortening this analysis time: 1) developing instruments that improve the data collected from each piece of surrogate glass collected and 2) create accurate fallout maps of this melt glass in reference with the topography and city infrastructure where the detonation will occur. By creating these updated fallout maps, the probability that the collection team is able to find glass samples containing useful fragments of the detonated bomb during the initial 24 hrs increases, therefore, decreasing the overall analysis time for the event.

This thesis discusses the work that was completed to help update current fallout maps produced by programs similar to the Department of Defense Fallout Prediction System (DELFIC). These maps were updated to account for the infrastructure and topography of the affected city. As shown in Figure 1-1, some of the cities infrastructure from the Hiroshima attack survived even when located within 0.4 miles from ground zero.

Figure 1-1: Infrastructure in Hiroshima that survived under 0.5 miles from ground zero

To ensure that the city is properly modeled, a separate code was developed to determine which buildings and structures were still standing after sustaining damage from the blast and shock effects. Depending on the structures remaining after detonation, the displacement of the large particulates of melt glass throughout the city was predicted. The code automatically calculated the urban matrix of soil from the area of detonation with a weighted soil composition from each horizon. Then it analyzed the energy distribution from the nuclear weapon as it propagated throughout the city infrastructure. Based on the buildings that were demolished, the building compositions were added to the urban soil matrix.

Methodology

Energy Output

The first part of the code that was developed calculated the total energy released during the nuclear detonation. The initial code only calculated the unhindered radius of the bomb, assuming a flat detonation plane. From these radii, the effect on the buildings from the blast was calculated to determine which buildings were vaporized and which buildings were left standing. The crater dimensions were used to calculate the soil volume and composition in the

area where the bomb was detonated. Depending upon the yield the user inputted into the code, the code produced weighted averages of the soil compositions from the following three different horizons: horizon A, horizon C, and bedrock. This helps to calculate the energy absorption of the soil from the nuclear weapon. The energy consumed by the soil was subtracted from the total energy of the weapon. The resulting difference was the energy used to calculate the thermal effects on the buildings. The radii for severe, moderate, and light damage ratios were altered as a function of the number of buildings added by the user.

Thermal Effects

In order to calculate the thermal effects, the total thermal energy (x-ray and heat energy) of the bomb was calculated. Figure 1-2 shows the fractionation of energy distribution from nuclear weapons. The amount of energy consumed by the evaporation of the soil is quantified by using calculations similar to those used by Giminaro et al[2].

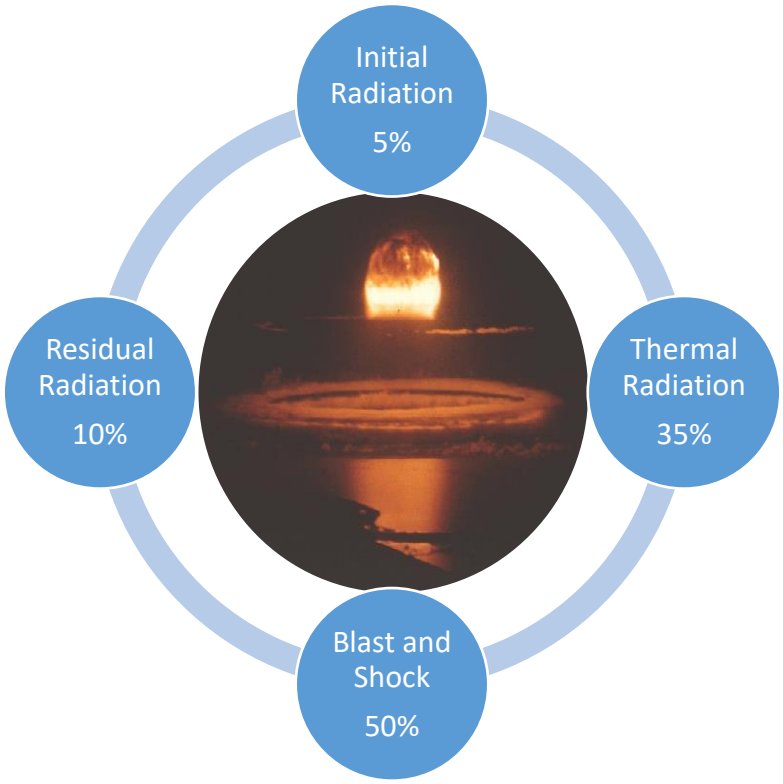

Figure 1-2: The energy distribution from nuclear weapons

The code accesses data from the geographical surveys conducted by the United States Department of Agriculture (USDA) from across the USA. When the user inputs the latitude and longitude of a specific location, the code selects the soil samples data from the areas nearest that coordinate. This data gives the user an elemental break down of the soil located at this area. The boiling temperatures of these elements are used to calculate an accurate model of energy consumed by the soil from the blast. Improvements in this code from previous fallout models, include more accurate calculations for crater size dependent upon yield, soil density, and current weather in the selected area. For example, if it is raining on the day of the detonation, the soil will be assumed to be densely packed, wet soil; therefore, decreasing the size of the crater and consuming more energy from the weapon. Once crater size is calculated, the volume is multiplied by the density of the soil to result in total mass. By using the mass ratios and the soil total mass, the result is an accurate model of the soil affected by the thermal effects of the weapon. Once total mass is calculated, the energy requirement to vaporize soil can also accurately be determined. This quantity is subtracted from the total energy released by the bomb which gives the resulting energy that is available for vaporizing or damaging the buildings.

When the soil calculations are completed, the code analyzes the energy requirement to vaporize catalogued building types. The code incorporates pre-programmed building structures that are user selectable to analyze for the different yields. These building structures are modeled after the most common building types located in an urban environment. Some building types reinforced concrete buildings, primarily stainless steel structures, and brick buildings. The models contain the material compositions of each building and the concentrations of each element; the material compositions are used to calculate the energy required to vaporize the buildings. The specifications for each building is entered into the code as well as including over-pressure maximum, dimensions of the building, and location of the building in relation to ground zero. By including these values, the code accurately predicts which building type will survive in the three main damage areas. Modeling codes typically show the three damage areas where damage from the bomb occurs. As shown in Figure 1-3, the areas are highlighted as light, moderate and severe damage regions. Due to code access

restrictions, the main codes that are used to calculate these damage radii are DELFIC and K-Division Defense Nuclear Agency Fallout Code (KDFOC) / National Atmospheric Release Advisory Center (NARAC).

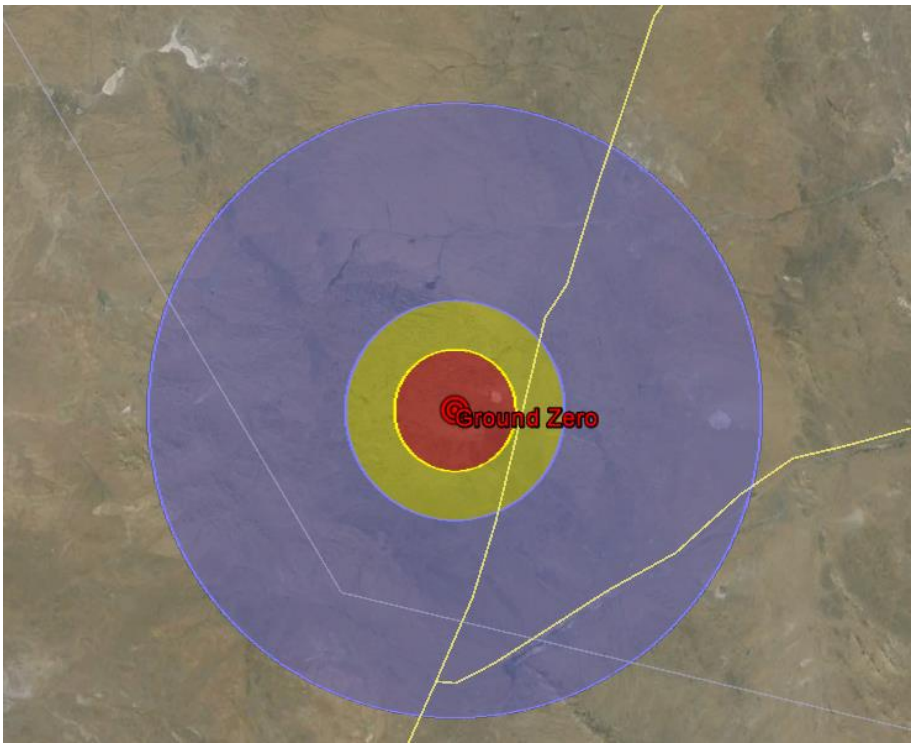

Figure 1-3: Damage areas from a nuclear detonation as modeled using DELFIC; blue is light damage, yellow is moderate damage, and red is severe damage

The code uses energy looping to continually account for energy lost per each building inside the weapon affects area. For this code, it was assumed that the blast expands isotropically from the weapon, and the user specified the buildings and locations of these buildings from ground zero. As the thermal wave expanded from ground zero the x-rays and thermal energy was attenuated by the urban environment setup by the user. Each building that the wave engulfs absorbed energy from the weapon, thereby affecting the final blast diameter. The blast diameter (dependent on the urban environment) was no longer be a round circle, but a somewhat deformed area where the buildings have absorbed the energy from the weapons.

The resulting map will contain the dimensions of the remaining buildings and damaged structures from the nuclear blast.

Chapter Summary

The first deliverable was a code that accurately predicted the soil composition of the city depending upon the latitude and longitude entered into the program. This accounted for the 3 different soil horizons and computed the weighted averages of the soil materials depending upon the depth of the crater and the depth of the horizon. The second deliverable was a code that modeled generic buildings mapped on a flat surface and this code accurately modeled the thermal effects experienced on those buildings for different yields of weapons and different layouts of buildings. The final deliverable allows the user to change the dimensions of the buildings, and predicts buildings that were destroyed, again dependent upon their location within the blasé zone. This provides an accurate map to use in determining the dispersion of large particulates from the nuclear blast.

By conducting this research, it will help shorten the collection time required for teams to find particulates that contain fragments from the detonated weapon. This will in turn shorten the analysis time; therefore, decreasing the required time for the USA to retaliate against potential nuclear attacks.

Chapter 2: Review of Current Nuclear Fallout Codes

Overview

The importance of developing a robust nuclear forensics program to combat the illicit use of nuclear material that can be used as an improvised nuclear device is widely accepted. In order to decrease the threat to public safety and improve governmental response, government agencies have developed fallout-analysis codes to predict the fallout particle size, dose, and dispersion. This paper will review the different codes that have been developed for predicting fallout from both chemical and nuclear weapons. This will decrease the response time required for the government to respond to the event.

Introduction

Since the development of nuclear weapons in the 1940's, the USA along with other countries, have detonated several atmospheric, surface, and underground nuclear devices. Table 2-1 shows the distribution of tests that have been conducted worldwide. Nuclear weapons tests were banned in 1996 under the Comprehensive Nuclear Test-Ban Treaty (CTBT). However, with rumors of other countries either developing nuclear weapons technologies or conducting actual tests, it is crucial that the US update their nuclear forensic technologies to guarantee proper response in the case of nuclear attack. [1]

Table 2-1: Distribution of Nuclear Weapons Tests Worldwide[3]

Country	Number of Events	Official Listing
China	45	CT (partial)
France	198	CEA/DAM (partial)
India	3	
Pakistan	2	
Soviet Union	715	RFAE
United Kingdom	21-24 Joint USA-UK	BLACKNEST
	24 Joint USA - UK	NV209
United States	1032	NV209
Unknown/ Disputed	1	
Total	2041	

These technologies include improvement of nuclear material characterization when interdicted material is found at border crossings; such as the analysis of nuclear facilities to ensure adherence with counter-proliferation procedures, and the analysis of post-detonation debris. A segment of improving post-detonation debris includes response and analysis requirements; to improve response in these areas, codes have been developed that map the potential path of fallout and predict placement of surrogate melt glass debris from a nuclear detonation. [4] By advancing methods to predict both path and placement of the debris, the time required for collection and analysis of sample materials decreases. [5]

To help improve the US's nuclear forensics capabilities, congress, in 2011, signed the NFAA. This act supplied funds to the Department of Homeland Security (DHS), the (NNSA, and the SSAP to improve the nation's forensics capabilities. As stated, "…it is necessary to have a robust capability to acquire samples in a timely manner, analyze and characterize samples, and compare samples against known signatures of nuclear and radiological material." [1]

One area in which the NFAA significantly increased funding was for improving forensic capabilities in the area of decreasing data-collection time of the glass surrogate created in the nuclear detonation. To shorten the analysis time required, further development is needed on the instrumentation used in evaluating the debris, and accurate fallout maps for the debris must be improved/ coded. By creating updated fallout maps, the probability that a collection

team is able to find glass samples containing useful fragments of the detonated bomb material during the initial 24 hours increases; therefore, decreasing the overall analysis time for the event.

Code Overview

Multiple codes have been developed by different government agencies to predict nuclear fallout. This section outlines the purpose of the codes developed, and the calculation methodology used to accurately calculate the fallout. Additionally, an in-depth analysis of the existing front-running codes is discussed; Table 2-2 gives a brief overview of all the fallout codes.

Table 2-2: A short overview of prevalent nuclear fallout prediction codes

Fallout Code	Lab Developer	Nuclear Yield	Dispersion Model	Weather Model	Blast Effects	Urban Environment	Temporal GIS
DELFIC	ORNL	Yes	Stabilized Cloud Model	Wind Direction	N/A	N/A	N/A
NARAC	LLNL	Yes	Stabilized Cloud Model	Wind Direction/Pressure and Density	N/A	Being Researched	Being Researched
KDFOC	ORNL	Yes	Stabilized Cloud Model	Wind Direction/Pressure and Density	N/A	N/A	N/A
HotSpot	LLNL	Yes	Stabilized Cloud Model	Wind Direction	N/A	N/A	N/A
HYSPLIT	NOAA/ARL	NO	Stabilized Cloud Model	Wind Direction	N/A	N/A	Terrain Following Coordinate
ERAD	SNL	Yes (maybe)	Stabilized Cloud Model/Focus on Small particles	Wind Direction	N/A	N/A	Surface Roughness
HPAC	LANL	NO (Case Study)	Two Methods: Cloud Rise, Radiation Transport	Wind Direction	N/A	N/A	For a specific area
RASCAL	LANL/NRC	NO (Dispersion Modeling)	Two Methods: Cloud Rise, Radiation Transport	Wind Direction	N/A	N/A	For a specific area

DELFIC (FPT)

Oak Ridge National Labs in conjunction with the Defense Nuclear Agency participated in the development of the DELFIC and Fallout Planning Tool (FPT). DELFIC development began in the mid 1960's with the purpose of becoming the standard for fallout prediction especially when applied to population safety in the event of dispersion [6]. DELFIC is a numerical fallout code that computes the cloud rise, growth, stabilization and transport of radioactive particles from a nuclear weapon detonation. DELFIC utilized the cloud rise module (CRM) and differs from other codes discussed in this paper, which start their debris calculation in the post cloud stabilization period.

DELFIC mainly utilizes information gathered from nuclear tests conducted in the 40's thru the 90's; however, to remain a competitive code, the CRM module was added to adjust the atmospheric parameters to better model the detonation scenario. After the user specifies the detonation conditions (i.e. barometric pressure, temperature in the area, and humidity levels), DELFIC begins calculations after the over-pressure wave reaches an equilibrium. By utilizing a fourth-order Rung-Kutta differential equation, the cloud rise from the Improvised Nuclear Device (IND) can be accurately calculated. The code can output up to 18 maps relating to the specific blast. Recently, due to the work done by Hopkins Et al.[7], the DELFIC code was updated from using a spatially constant wind field to using wind vectors. This capability was developed to work with wind data stored at the National Oceanic and Atmospheric Administration (NOAA). This expedites the computational time required by autonomously adding pressure, temperature, and wind vectors based upon data compiled at NOAA, assuming the blast occurred previously to the date. With the addition of the various modules and by using data taken from nuclear tests conducted, DELFIC is a competitive fallout code. [8]

HPAC

Hazard Prediction and Assessment Capability (HPAC) is a modeling software primarily developed by the Defense Threat Reduction Agency (DTRA) for military and civilian emergency response purposes to predict atmospheric dispersion from biological, chemical, or radiological attacks. The Nuclear Weapon Incident (NWI) and Radiological Weapon (RWPN) modules were

added to HPAC to insure accurate fallout prediction of fallout during a Weapon of Mass Destruction (WMD) detonation. The NWI primarily focuses on predicting radiological dispersion from radioactive material attached to a chemical explosive. The NWI module allows the user to specify the chemical weapon system used to detonate the IND in which the modules will provide HPAC with an accurate source term. The RWPN module allows the user to specify the mass and type of explosive used to disperse the radioactive material. These parameters are used to calculate the source term. The HPAC uses the data entered by the user to develop a model of the formation of the smaller particles distributed during a nuclear detonation. To predict the distribution, HPAC uses the Second-order Closure Integrated Puff (SCIPUFF) model; which is based from the Gaussian plume model distribution. [9]. The output of this program is a map that shows effects of the incident with respect to dose rate and particle size distribution. [10]

HYSPLIT

Hybrid Single-Particle Lagrangian Integrated Trajectory (HYSPLIT) Model was developed by the National Oceanic and Atmospheric Administration (NOAA) to calculate air particle trajectories and their dispersion and/or deposition. This code was originally created to aid in finding the fallout plumes from Soviet nuclear weapons tests. The original method for calculating the path of fallout was by using wind data gathered from balloons and applying this to the back trajectories method. By following the wind vectors this method allowed the U.S to track the Soviet fallout path within 5% error. [11] As computational capabilities improved the back trajectories method was replaced with the Gaussian plume model; however, the wind vectors were still used to predict the path of the fallout cloud.

In recent years, the modeling method in HYSPLIT was changed to incorporate a time step function for higher fidelity modeling. Table 2-3 shows the nuclear fallout capabilities that HYSPLIT possesses. Instead of the Gaussian plume model, the code was upgraded to incorporate the modified discrete-time Langevin equation. This equation utilizes the velocity calculated from the wind vectors and denoted in Eq.2-1 and 2-2 as U' and W'. The X_{mean} and Z_{mean} are the average particle position in the previous generation of time (t-Δt).

$$X_{final}(t + \Delta t) = X_{mean}(t + \Delta t) + U'(t + \Delta t)\Delta t \quad (2\text{-}1)$$

$$Z_{final}(t + \Delta t) = Z_{mean}(t + \Delta t) + W'(t + \Delta t)\Delta t \quad (2\text{-}2)$$

By using the discrete-time Langevin equations, this allows the user to accurately predict the particle path in real-time. HYSPLIT was modified recently to model fallout patterns from detonated nuclear weapons. Because the code models fallout based individual particle tracking, the weapons are assumed to be single particle distribution sources. [6] In order to accurately model each nuclear weapon, the yield of the weapon was based upon the number of particles the weapon was predicted to produce. To simulate weather in a specific area, HYSPLIT uses gridded meteorological data; therefore, the wind vectors are loaded into the computer code. [12]

Table 2-3: Nuclear Fallout Prediction Capabilities of HYSPLIT

Application	Location	Brief Description	Reference(s)
Radionuclides	Marshall Islands (central Pacific), Nevada Test Site (United States), Semipalatinsk Nuclear Test Site (Kazakstan)	Deposition of fallout from atmospheric nuclear tests	Moroz et al. (2010)
	Areva NC La Hague nuclear processing plant (northwestern France)	Krypton-85 air concentrations	Connan et al. (2013)
	Fukishima and adjacent prefectures (Japan)	Air Parcel transport and dispersion to interpret iodine, tellurium, and cesium measurements	Kinoshita et al. (2011)
	80-km range around Fukshima Reactor (Japan)	Temporal behavior of plume trajectory, concentration deposition and radiation dosage of cesium-137	Challa et al. (2012)
	Global	Transport, dispersion and deposition of Xenon-133	Bowyer et al. (2013)
	Metropolitan area of Seoul, South Korea	Radiological dispersion devices (RDD's) terrorism containing cesium-137	H. Jeong et al. (2013)
	Fukishima (Japan) and global	Emissions, transport, dispersion, deposition, and dosage of cesium-137 Iodine-131	Draxler and Rolph (2012) Draxler et al. (2013)
	Nevada Test Site	Dispersion from Nuclear Test	Rolph et al. (2014)

FDC

Fallout Dispersion Code (FDC) is a code developed by the United States Air Force Institute of Technology in 2009. FDC utilizes the best capabilities from both DELFIC and HPAC to predict the fallout pattern [13]. Instead of using the yield of the weapon to predict fallout, FDC uses a particle size distribution of 100 particles; then uses wind and cloud modules to simulate the weather during the nuclear explosion. By adding a fallout modules and a time step routine, accurate dose- rate contours can be produced. [14]

NARAC (KDFOC)

The National Atmospheric Release Advisory Center (NARAC) is a center that is comprised of multiple fallout modeling codes primarily used by Lawrence Livermore National Laboratories (LLNL). The center mainly focuses on mapping hazardous airborne particles as they are dispersed from the plume. Users may submit their input decks to NARAC's server in which real-time calculations are completed and sent directly back to the user. NARAC has multiple applications such as average plume dispersal or a detailed dispersion depending on the hazardous material release scenario. In order to successfully predict fallout in these various scenarios, NARAC utilizes the Atmospheric Data Assimilation and Parameterization Tool (ADAPT) metrological data model. This model accounts for the temperature, turbulence, pressure, and other factors to interpolate the location of the hazardous material fallout. The second system which allows NARAC to predict fallout with varying topography and geology is the Lagrangian Operational Dispersion Integrator (LODI) dispersion model. This accounts for all the factors included in the ADAPT model with addition to topography and geological factors. This process requires more time and computational requirements; however, it does produce a high fidelity fallout map.

The main fallout module that is incorporated into NARAC is the KDFOC3 nuclear fallout assessment capability. KDFOC3 is unique from the other fallout codes in that it primarily focuses on the spread of gamma-ray activation products produced during the detonation. It is an empirical code which utilizes and compares output to similar Nevada Test Site (NTS) data that has been collected during the nuclear tests. To optimize run time of KDFOC, an integration

of all fission products is conducted and only the long lived nuclides that are produced are used to model the fallout. By using a reverse-time disc-tosser model, the model will back calculate cloud rise based upon the time and displacement relationship as shown in Figure 2-1. To verify that this method can successfully predict cloud rise, it is compared with pertinent NTS data.

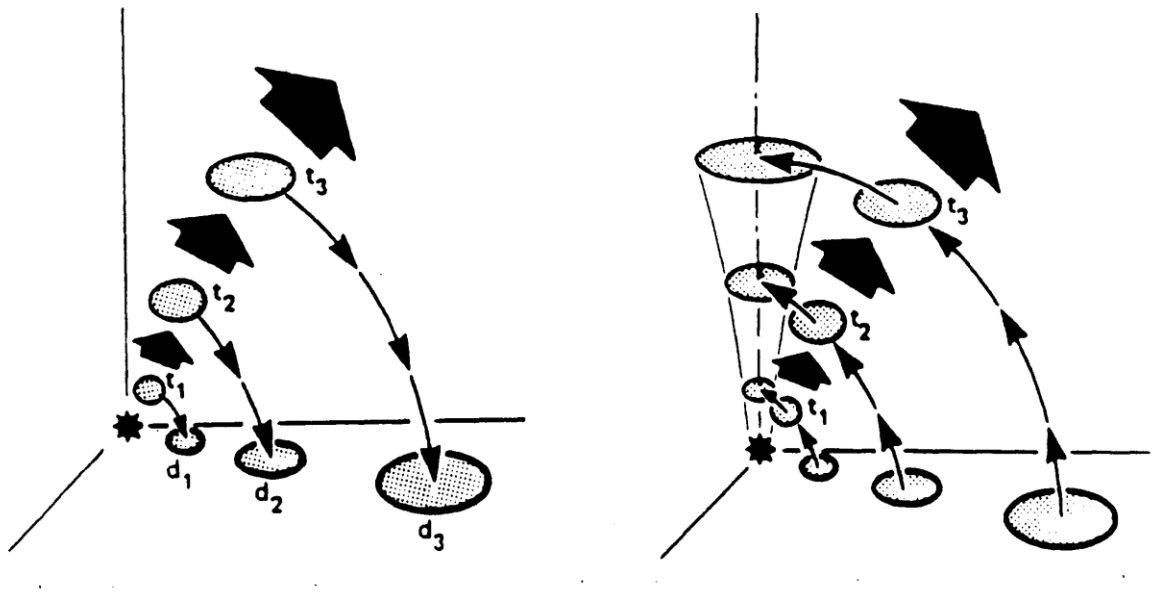

Figure 2-1: Time-Reversed Disc Tosser Model used in KDFOC3

Capabilities of other Codes

Code Validation Method

To validate nuclear fallout codes, the simulated data must be accurately compared to observed data. The codes must also be tested with varied detonation scenarios that include variation in height of burst (HOB), weapon yield, and meteorological data. [15] For each set of parameters, the predicted fallout area path (APR) is printed onto a map, and the area of the observed fallout (AOB) from the actual weapon test is overlaid onto that same map. The two

areas are calculated, and the area of overlap (AOV) between the APR and AOB is calculated and graphically shown in Figure 2-2.

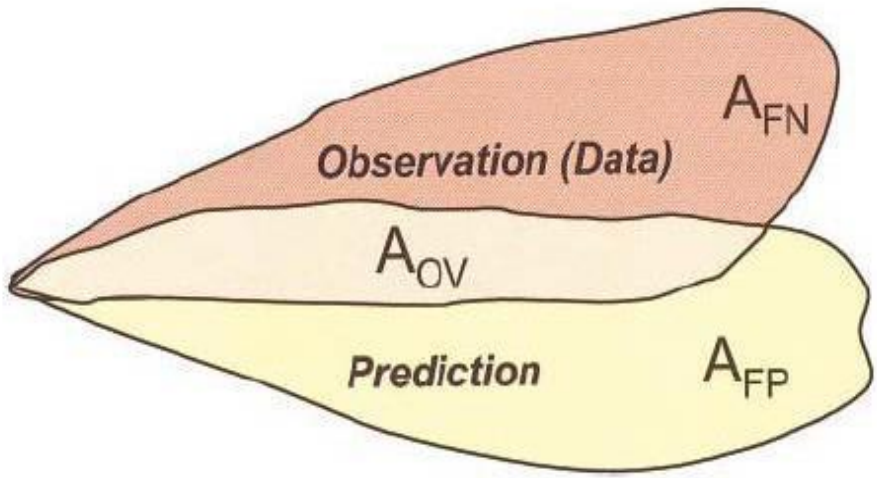

Figure 2-2: Fallout areas that determine the accuracy of a code [16]

The area that is in the APR but is not in the AOV is counted as the area of false positives (AFP); similarly, the area that is not in the AOV but is AOB is considered to be an area of false negative (AFN). By calculating these area values, the Warner and Platt's Measure of Effectiveness (MOE) can be used to visually demonstrate the codes that most accurately predict fallout (Eq.2-3).[17] As shown in Figure 2-23, beginning with a model prediction, shown as point A, the MOE is used to determine how the changes in false positives and false negatives changes the accuracy of the model predictions. If during a specific run, there is a decrease in both false positives and false negatives the MOE indicates the model is getting "better" as shown by points B and D. If there is a decrease in false negatives but not a significant change in false positives, or if there is a decrease in false positives but not a significant change in the false negatives the MOE is not decisive in indicating the accuracy improvement in the code as shown by point C, or in the "not decisive region in the upper left hand portion of Figure 2-3.

$$MOE = \left(\frac{AOB - AFN}{AOB}\right), \left(\frac{APR - AFP}{APR}\right) \tag{2-3}$$

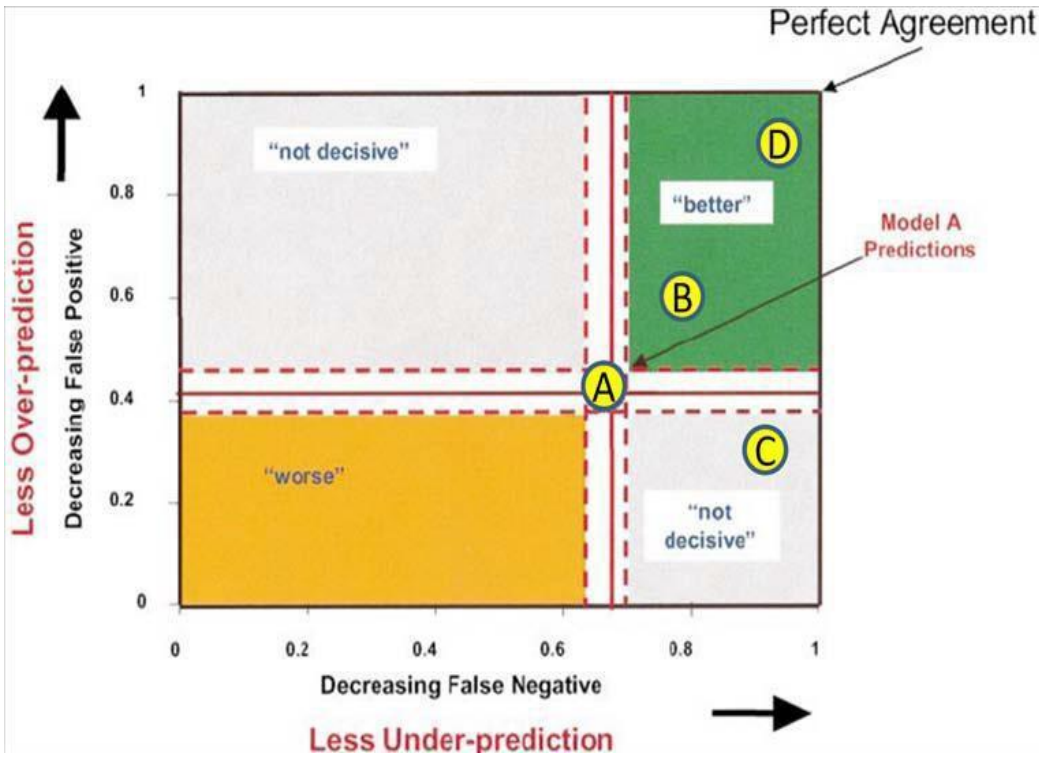

Figure 2-3: Prediction model demonstrating a changing of false positive values or false negative values, decreases in false positive values or false negative values is not a conclusive factor in determining fallout code accuracy [13]

In order to solve this problem, a numerical absolute difference (NAD) technique was used to improve the comparison between the codes. Eq.2-4 is used to calculate a NAD value for different codes, and this provides an actual numerical value to determine accuracy. This method depends more on the AFP and AFN values to improve accuracy in the comparison. Figure 2-4 shows isolines that are generated from the NAD values; these values show the correlation between AFN, AFP, and the overall predicted accuracy of the fallout code.

$$NAD = \frac{AFN+AFP}{2AOV+AFN+AFP} \tag{2-4}$$

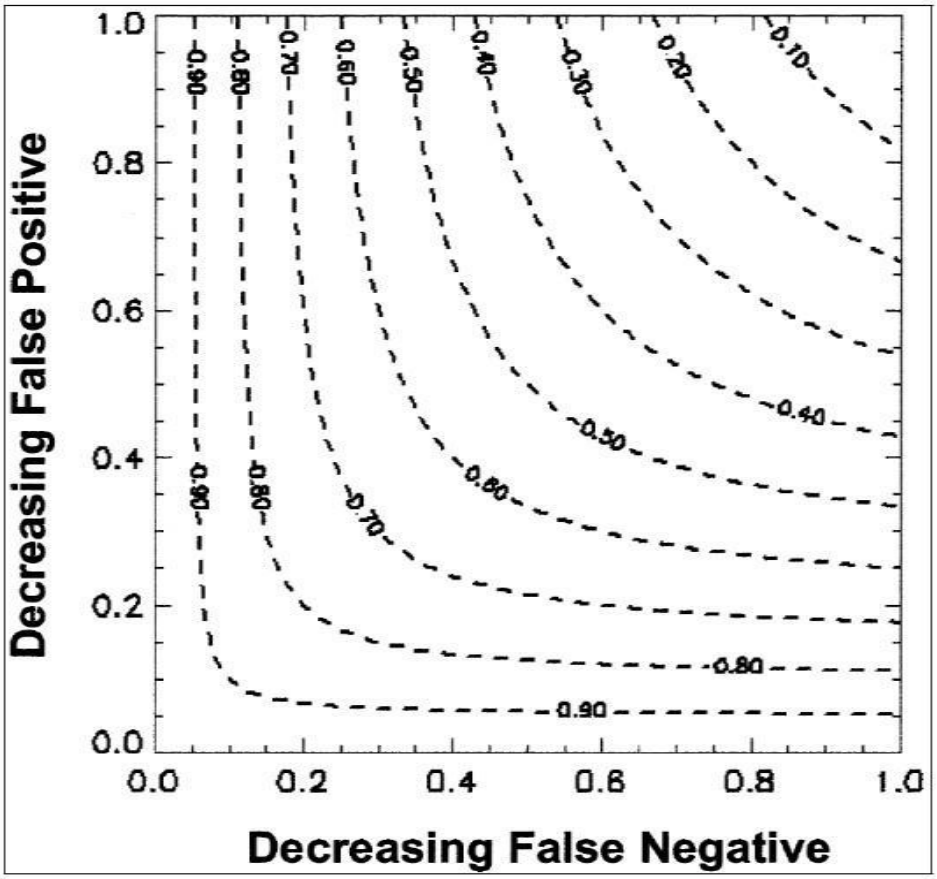

Figure 2-4: NAD values associated with the isolines [16]

By using the NAD values for comparison, multiple codes can be compared against a common standard to compare accuracy predictions. Also by using both the MOE and NAD, an accurate comparison of the codes may be completed. [18]

Results

Comparison of HPAC, HYSPLIT, DELFIC, and FDC

In order to test the codes, 6 different nuclear test shots were used. These test shots substantially varied in HOB and yield as shown in Table 2-4. Fallout maps generated from the fallout codes were compared with actual fallout maps collected by the Defense Nuclear Agency (DNA) [3] at the time of the test.

Table 2-4: Data from each nuclear test that was used in comparing the fallout codes [13]

Operation: Test	Date Time Group (Zulu)	Location (DD.MM.SS)		Yield (kT)	HOB (ft)	HOB (m)
		Lat	Lon			
Tumble Snapper: George	011155Jun1952	37.02.53	116.01.16	15	300	91.44
Teapot: Ess	232030Mar1955	37.10.06	116.02.38	1	-67	-20.4216
Teapot: Zucchini	1501200May1955	37.05.41	116.01.26	28	500	152.4
Plumbbob: Priscilla	241330Jun1957	36.47.53	115.55.44	37	700	213.36
Plumbbob: Smoky	311240Aug1957	37.11.14	116.04.04	44	700	213.36
Sunbeam: Johnnie Boy	111645Jul1962	37.02.21	116.19.59	0.5	-2	-0.6096

The 4 different codes were modified to account for these varying conditions, and the weather was modeled from data obtained from NOAA. Because each code varies on weather

simulation techniques, each code was run 3 times using different wind vector displays. These wind display conditions included the following: ground wind (GW), averaged weather profile (PRF), and a combination of GW and PRF. For each different weather simulation, the MOE and NAD value was calculated. The weather simulation that contained the lowest NAD value was used as the code validation number. Table 2-5 shows data from the GEORGE test in comparison to three different weather simulations using DELFIC. Figure 2-5 shows the fallout patterns from the actual test and the fallout pattern simulation of the two weather conditions with the lowest NAD value.

Table 2-5: Compares the MOE for 3 different weather patterns to actual fallout data from the GEORGE test [16]

	MOEx	MOEy	NAD
GW	0.59	0.98	0.26
PRF	0.33	0.97	0.50
GW(2hr)-PRF	0.33	0.95	0.51

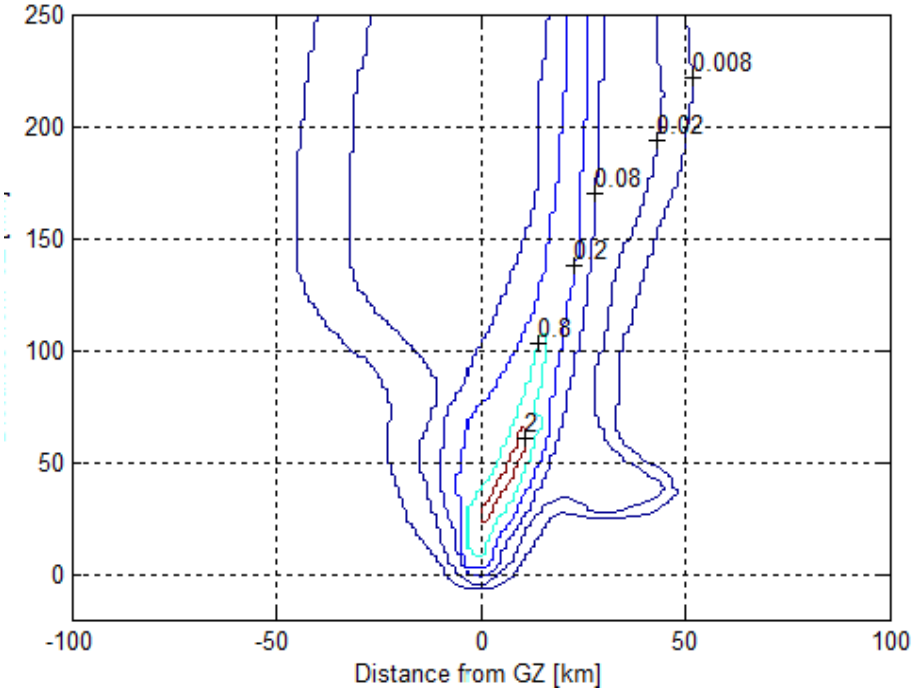

Figure 2-5: Actual Test Data from the George test [13]

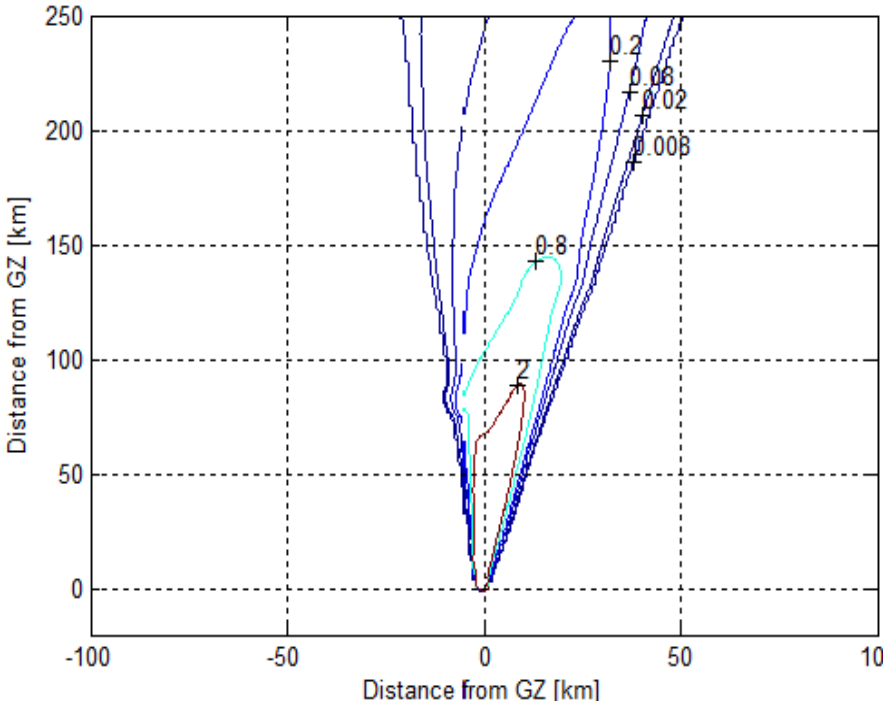

Figure 2-6: GW method to predict the fallout pattern from the GEORGE test [13]

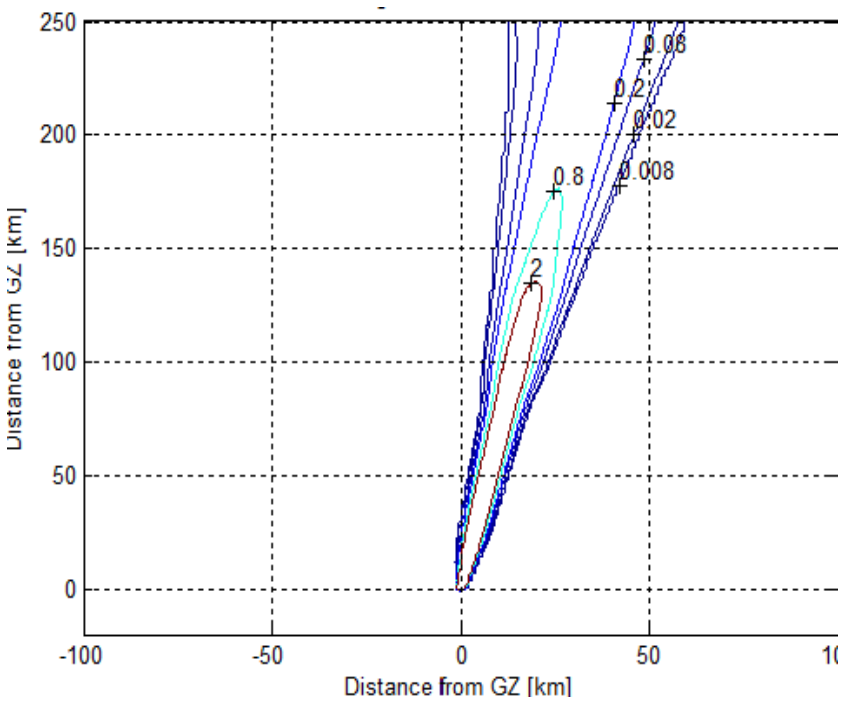

Figure 2-7: PRF method to predict the fallout pattern from the GEORGE test [13]

After all tests were run using the weather pattern that achieved the lowest NAD value, the data was plotted in Figure 2-8. This demonstrates how the NAD value changes in value depending on dispersion of fallout growth.

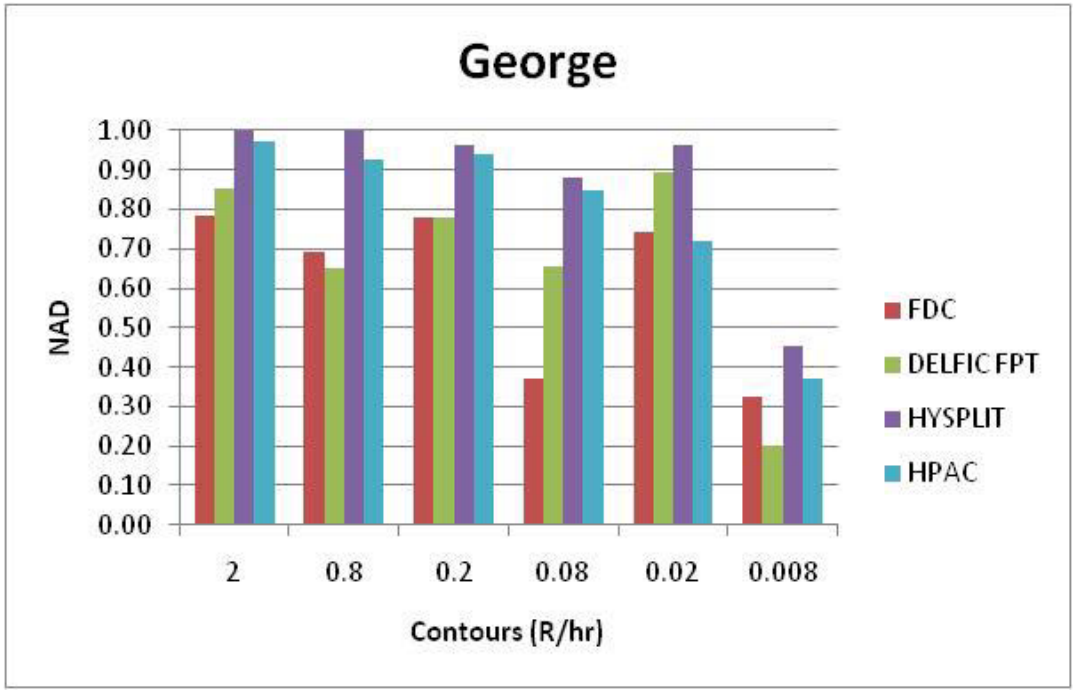

Figure 2-8: NAD value vs. Contours (Dose Rate) for the GEORGE nuclear test *[13]*

After successfully running all weather patterns for the 6 nuclear tests, it is conclusive that as the cloud dispersion increases, the NAD value consistently decreases. Therefore, most of the fallout codes are reliable for post-cloud stabilization after a 24hr period of time. Table 3 shows the average NAD values for the 6 different nuclear tests. In conclusion, the newly developed FDC received the lowest NAD values for 3 of the tests; however, DELFIC and NAD received the lowest NAD average value. Therefore, the best fallout codes to use in assessing a post-detention scenario is either FDC or DELFIC.

Comparison of HPAC and NARAC

By utilizing the same method of code comparison previously highlighted the HPAC and NARAC codes predicted contour dose plots in comparison to known dose curves. To insure all a high-fidelity comparison nine scenarios were simulated and modeled in which runs 1-3 of the scenarios were stable cases, runs 4-6 were close-to stable (neutral) scenarios, and runs 7-9 were unstable cases. Table 5 highlights the MOE values for the 9 runs used to test NARAC and HPAC. Figure 2-9 demonstrates how NARAC and HPAC compare when modeling the stable, neutral, and unstable gas types after 30 minutes from the release time.

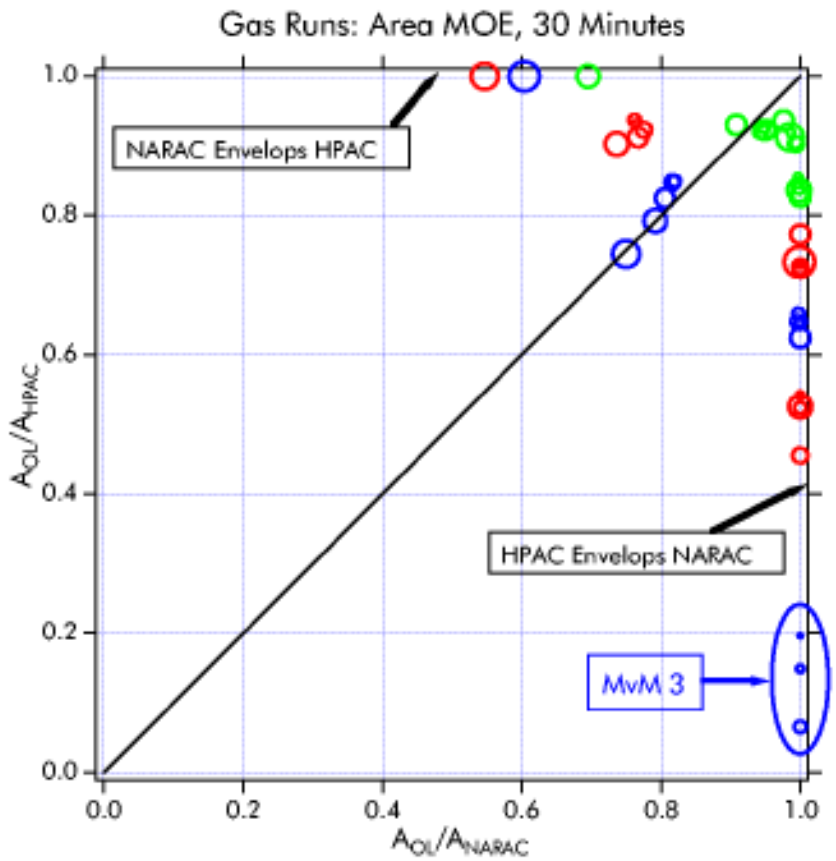

Figure 2-9: A comparison of NARAC and HPAC models when modeling the different gas types. The colors denote type of gas (Red=Stable, Blue=Neutral, and Green=Unstable), and the circle size demonstrates the changing dose rates modeled. A larger circle indicates more dose was modeled [14]

Chapter Summary

In conclusion, the first comparison was completed by comparing the MOE and NAD values from DELFIC, HPAC, HYSPLIT, and FDC. These codes were benchmarked against 6 actual nuclear weapons tests and the fallout patterns produced by these weapons. The lower NAD values point toward the fallout code that best matched the empirical fallout pattern collected at the NTS. The lowest NAD values are highlighted in Table 2-6. It is shown that FDC more closely matched the fallout pattern from the 3 out of 6 weapons. However, DELFIC and FDC had the same average NAD values for all 6 tests. Therefore, FDC more accurately predicts weapons fallout, but DELFIC is a close competitor.

Table 2-6: Average NAD values for the codes for all nuclear tests simulated

	Ess	**George**	**Zucchini**	**Priscilla**	**Smoky**	**Johnnie Boy**	**Average NAD**
DELFIC FPT	0.75	0.26	0.44	0.28	0.30	0.33	0.39
FDC	0.72	0.14	0.16	0.54	0.44	0.31	0.39
HYSPLIT	0.37	0.23	0.35	0.52	0.80	0.49	0.46
HPAC	0.83	0.56	0.63	0.95	0.99	0.98	0.82

In the second comparison only the MOE was used to determine the accuracy of NARAC and HPAC. In order to accurately compare all the codes focused on in this paper, an average of all MOE values for all the codes were compiled in Table 2-7. These values were compared to the values located in Table 2-8. After looking at the MOE values NARAC, FDC, and DELFIC are comparable in accuracy.

Table 2-7: The average of all MOEx, MOEy, and NAD values from the 6 nuclear tests

	MOEx	MOEy	NAD
HYSPLIT	0.32	0.49	0.46
FDC	0.56	0.75	0.39
DELFIC	0.56	0.77	0.39
HPAC	0.11	0.66	0.82

Table 2-8: Average MOE values for NARAC and HPAC 30 minutes after release time [14]

Contour Level (kg s/m 3)	**HPAC Area (km2)**	**NARAC Area (km2)**	**Overlap Area (km2)**	**MOE(x)**	**MOE(y)**
1.00E-10	42.53	44.05	36.13	0.82	0.85
1.00E-09	34.79	36.1	29.47	0.816	0.847
1.00E-08	26.9	27.55	22.19	0.806	0.825
1.00E-07	18.74	18.77	14.86	0.792	0.793
1.00E-06	9.75	9.68	7.26	0.75	0.745

Overall, the codes reviewed in this paper are impressive and can accurately model fallout; however, FDC, DELFIC, and NARAC are more accurate when predicting nuclear fallout.

Chapter 3: Soil Library Development

Overview of Chapter

It is crucial that the collection time, for surrogate melt glass that is created during a nuclear detonation, is shortened to help decrease the total analysis time required. Fallout maps generated using programs similar to the Department of Defense Fallout Prediction System need to be updated to accurately depict damage from the thermal and shock effects of a weapon in an urban environment. This system should be updated to aid in determining accurate melt glass matrices created from that urban location. This will enables future researchers to predict where the desired material will be deposited in specific cities. To complete this task, the software packages were updated to account for city infrastructure, geographical topography, and weather conditions during the detonation.

Soil Composition Prediction

In order to accurately predict both the blast kinematics and surrogate debris composition it was crucial to have accurate soil data for the affected area(s). Data for the soil composition was acquired from the U.S. Geological Survey (USGS); the USGS has collected approximately 4,841 soil samples from the lower 48 continental United States. These soil samples were taken from horizon O, A, B, and C of the soil with the corresponding latitude and longitude location and are representative of soils found in urban areas near the sample points. As shown in Figure 3-1 the depth of each horizon extends specific distances beneath the surface of the ground; however, the depth of horizon C depends on the location at which the soil samples were collected. It is concluded that horizon C does not extend past 150cm regardless of the location in which the soil samples were collected [19]. Since the crater depth of a nuclear weapon surface burst exceeding yields of 0.001 KT surpasses a depth of 150cm, it is important that soil composition-prediction methods be utilized to help determine soil compositions at larger depths. As shown in Figure 3-1 the layer of soil beneath the horizon C layer is bedrock.

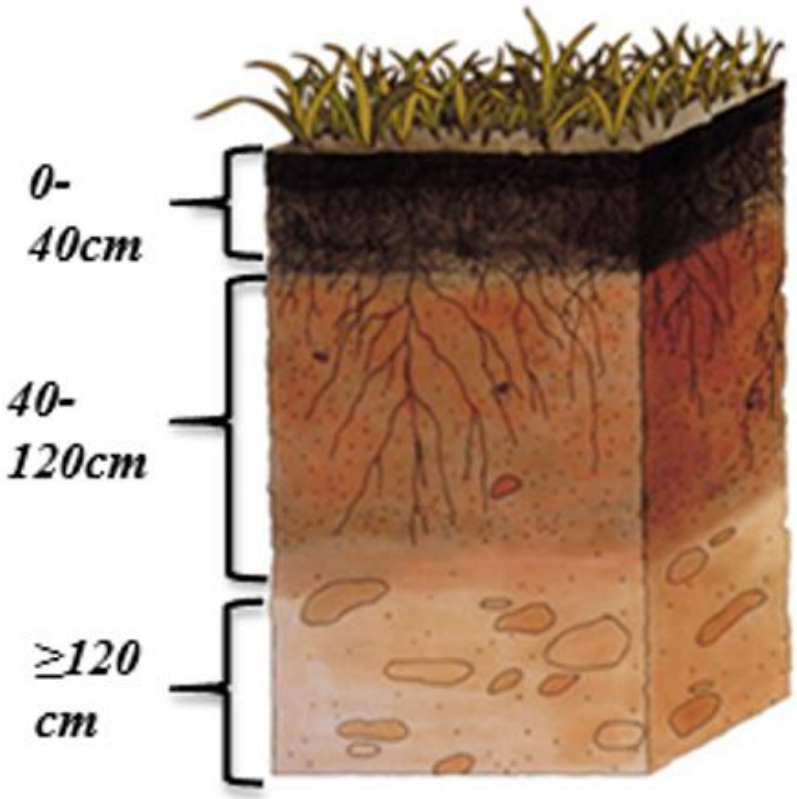

Figure 3-1: A soil profile with the depths of each horizon indicated [20]

Horizon C soil is mostly comprised of particulates that have been broken from the bedrock crust with small contaminates from the O, A, and B horizons. By calculating the largest contributing chemical compositions of the horizon C soil, this composition was used to predict the type of bedrock found beneath horizon C. There are limited forms of bedrock located in the continental United States, therefore by using the mineralogical composition obtained from USGS data of horizon C the algorithm determines the bedrock composition that closely matches the horizon C composition.

For example, it was reasonably estimated that any C horizon with silica content higher than 75% has an underlying bedrock layer that is sandstone, siltstone, mudstone, chert, quartzite or other silica-rich bedrock type. Sandstone, for instance, is almost entirely silica. Though sandstone is estimated at 96% silica, the C horizon above this bedrock layer likely has silica content lower than 96% unless it is entirely sand. This is due to erosion or other

transportation methods of the weathered bedrock (sandstone in this case) and transporting the material elsewhere. Some nutrients, organic matter, other sediments also leach into the C horizon from layers above. Additionally, silica readily leaches from the soil. It was reasonably estimated, however, that since silica leaches so readily, anything above 75% silica is a silica-rich bedrock type. This is because there are no other bedrock types with chemical percent compositions with a silica content greater than 74.5% that isn't considered a "silica-rich" bedrock. This was tested by using a sample soil from 35.6519 N 88.8448 W (Jackson, TN) whose percent silica content for the C horizon was 97.4% or entirely sand. This sand, however, does not originate from the bedrock; but rather from when the land was a prehistoric shallow sea. The bedrock in the western part of TN is buried a few thousand feet below the surface according to some studies. So another test was run on a sample with a silica content of 76.4% at the location with a latitude of 35.8203 and a longitude of -85.4205. According to the hypothesis, the bedrock at this location would be a silica-rich bedrock. The location was just outside of Doyle, TN, which sits atop the Cumberland Plateau, a geologic formation that stretches from northeastern Alabama to eastern Kentucky. This geologic formation is present due to a sandstone cap that is highly resistant to weathering. This evidence upholds the hypothesis that a C horizon silica content of at least 75% sits on top of a bedrock that is silica-rich, such as sandstone. In the case of the bedrock that is several thousand feet under the surface due to the alluvial floodplain, that bedrock composition is not relevant to this study on surface detonations.

As it stands, C horizons with at least 50% calcite have a bedrock of limestone. Pure limestone is chemically pure calcite; however, most limestone deposits are not pure and have other oxides within their composition and each limestone deposit is unique in that aspect. The conclusion at this point of 50% calcite being derived from limestone was taken due to the observation of a 58.4% calcite composition in Seligman, Arizona, which sits atop either the Redwall or Kaibab Limestone formations of north-central Arizona. Through further research it may be discovered that limestone bedrocks can produce a parent material in the C horizon with less than 50% calcite.

Crater Modeling

After the soil libraries were updated in the algorithm, an accurate simulation of the crater development and growth was modeled to help predict the soil composition distribution factors in surrogate matrices. Because the Nuclear Urban Kinetics Effects Simulator (NUKES) uses a weighted average of soil contribution based upon crater depth, it was crucial to account for the varying soil densities that occur in different areas around the continental US. As shown in Figure 3-2, the important dimensions calculated are the actual depth (D_a) and R_A. By calculating these dimensions, a volume of the crater was calculated to understand the mass of soil contributing to the urban glass matrix. This will help to understand the amount of energy deposited into the soil from the WMD.

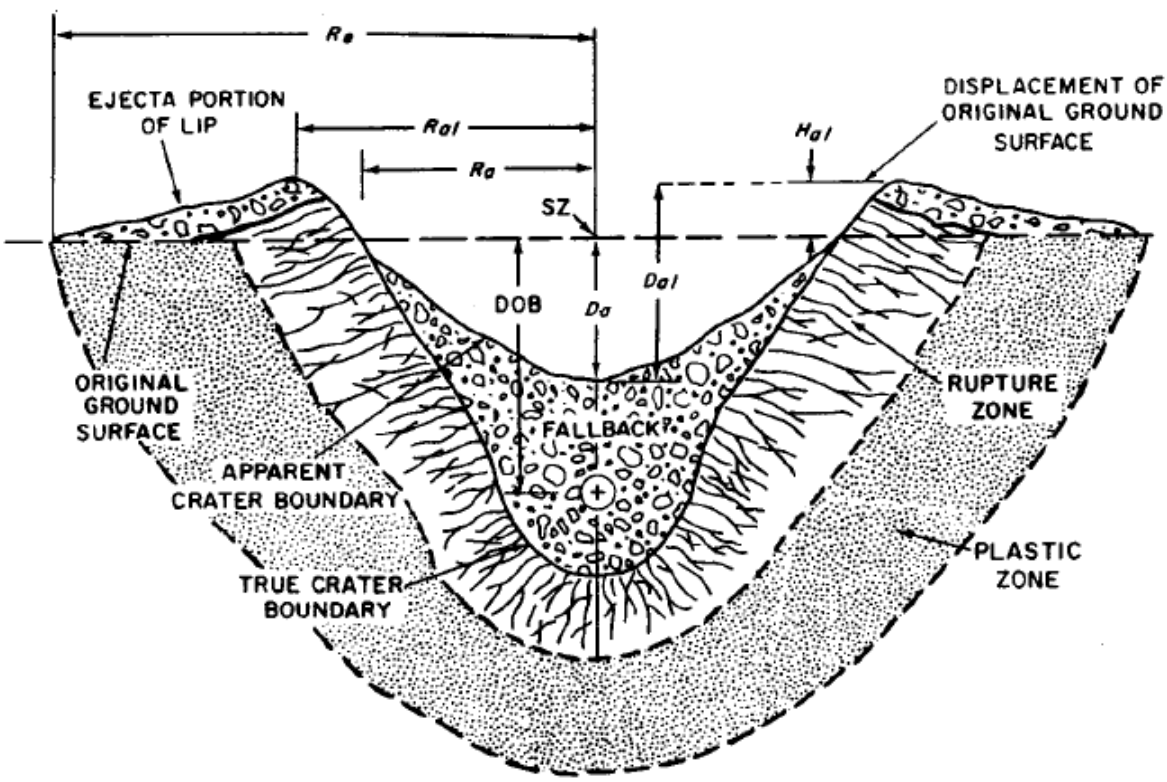

Figure 3-2: Diagram of the Crater that is formed during a surface detonation[21]

The crater dimensions are calculated from the Glasstone book *Effects of Nuclear Weapons [21]*, and the crater is assumed to be a half sphere going into the ground. Although the crater does not have as wide a radius at the bottom as it does at the top, the difference in the calculations are negligible. The user has the option to choose 4 of the following types of soil and density surrounding ground zero: wet soil (wet soft rock), dry soil (dry soft rock), wet hard rock, and dry hard rock. Since building structures must be built upon packed soil/bedrock this will exhibit similar blast behavior as the concrete of buildings; therefore, this will not drastically affect the shape of the crater. However, this will change the soil recipe that NUKES outputs to the user. The data displayed in Figure 3-3 and Figure 3-4 shows the changes of the crater diameter depending depth of burst. The changes in crater size are discussed in Chapter 8.

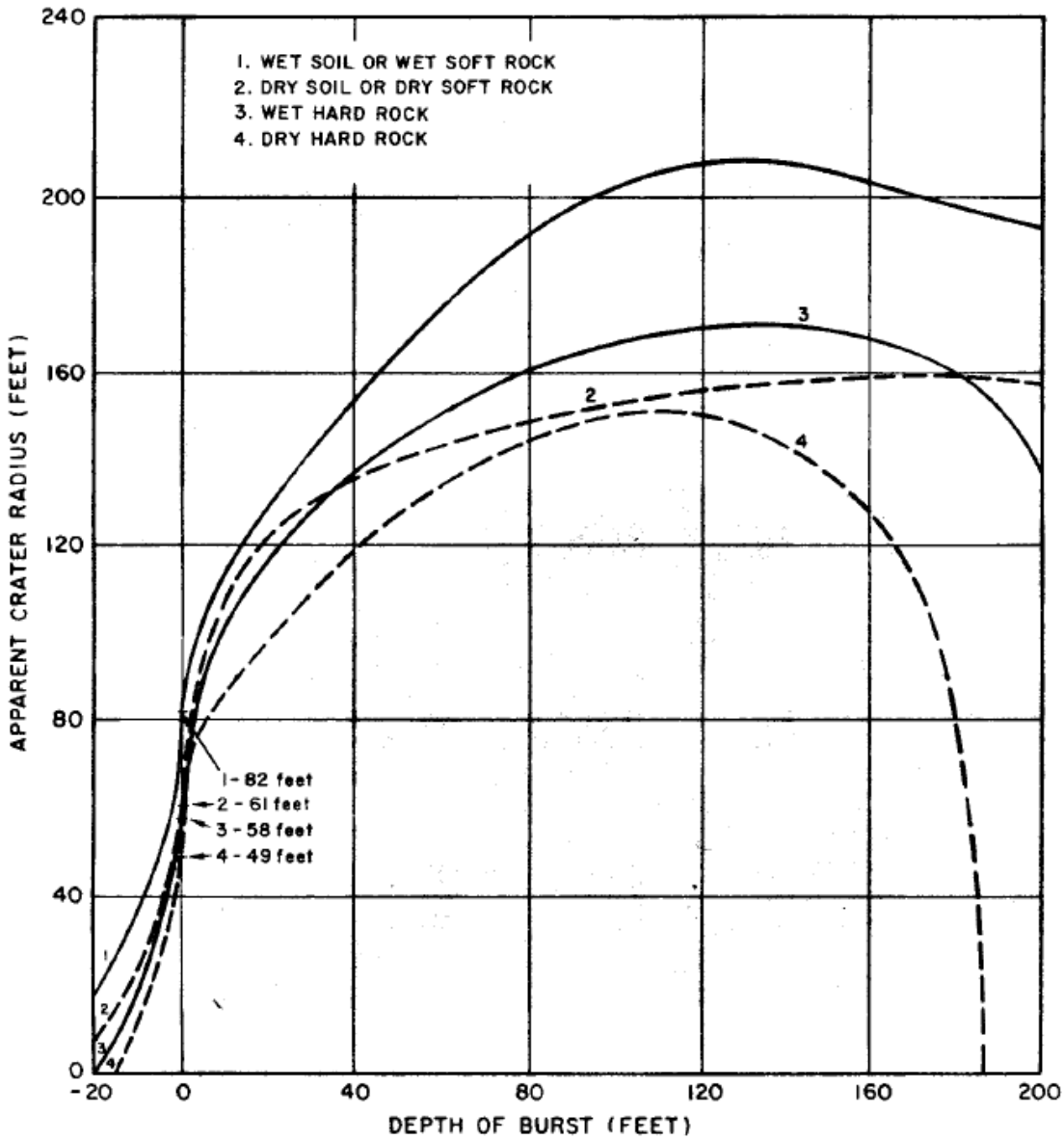

Figure 3-3: Specific soil types versus changes in radius of crater[21]

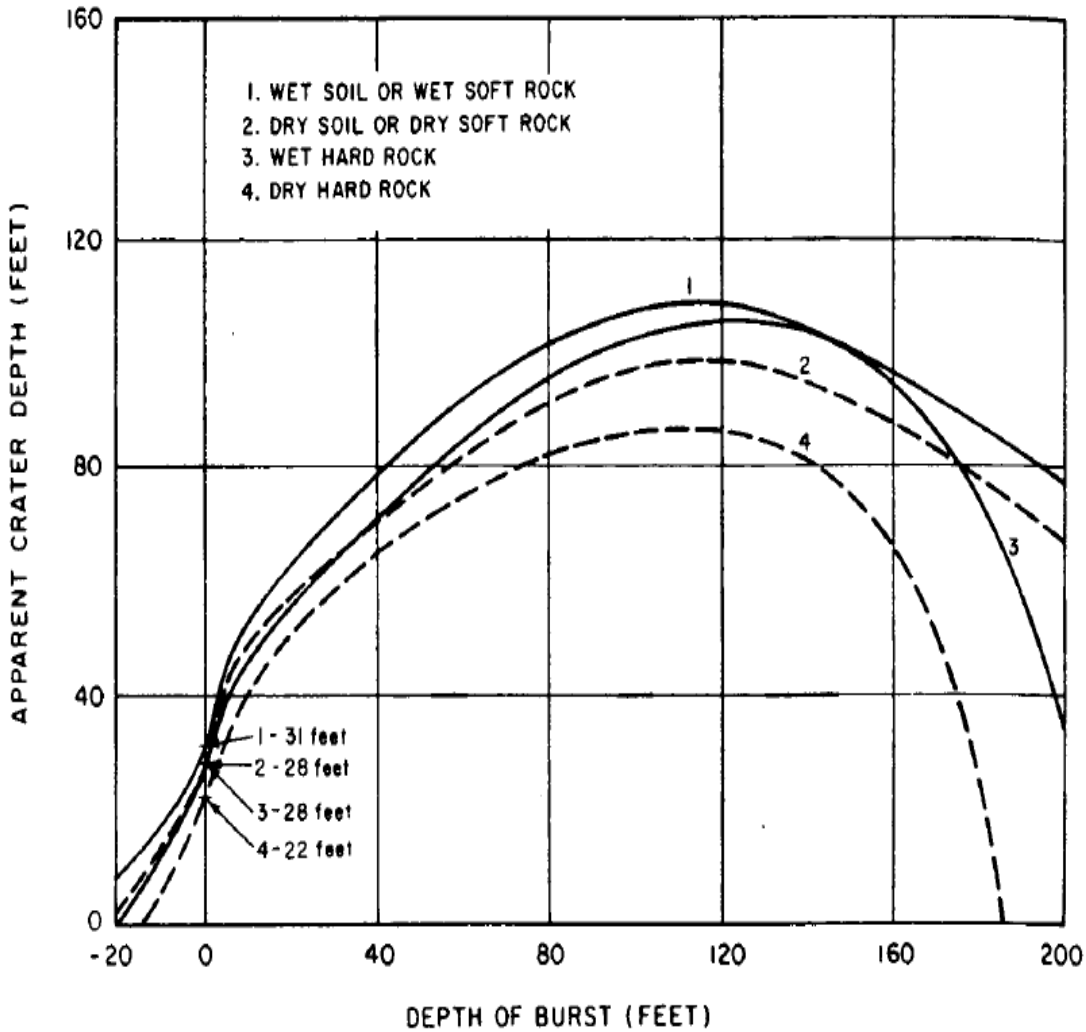

Figure 3-4: Crater depth as a function of depth of burst and type of soil [21]

The crater dimensions were calculated by using Eq.3-1 and Eq.3-2, where R_a is the actual radius of the crater, R_{ap} is the apparent radius of the crater, W is the yield of the weapon in KT, D_a is the actual depth, and D_{ap} is the apparent depth.[21] Although the original Glasstone equations used EST measurements, the program will output all values in the metric system values. This will ensure versatility if the program is incorporated into other programs. The growth of the crater was modeled using a mesh grid.

$$R_a = R_{ap} * W^{0.3} \tag{3-1}$$

$$D_a = D_{ap} * W^{0.3} \tag{3-2}$$

After the crater depth and radius was calculated, the volume of the crater was calculated by using the actual radius and actual depth (R_a, D_a). The density that the user specifies or selects from the menu is multiplied by the volume of the crater, see equation 3-3, to determine the total amount of soil that is vaporized. The total amount of energy deposition can be calculated and subtracted from the total yield. The soil mass will also be used to complete the urban matrix calculations.

$$V_C = \frac{1}{2} * \pi * R_a^2 \, D_a \tag{3-3}$$

The final calculation that is made for the crater dimensions are the radius of ejecta (R_e) where R_{ap} is the apparent radius of the crater and W is the yield of the WMD. This value, calculated in equation 3-4, gives an estimation of the radius of large particulate distribution. This equation was based upon actual test data recorded during US tests.

$$R_e = 2.15 * R_{ap} * W^{0.3} \tag{3-4}$$

Chapter 4: Blast Effects Basics

Overview of the Chapter

This chapter focuses on the nuclear weapons modeled in the NUKES code. An overview of the different types of bursts and varying weapons' designs drastically change the effects of the weapons. Therefore, an in-depth understanding of the nuclear weapon detonations will improve the model.

Introduction

The phrase "nuclear explosion" is in fact a misnomer when discussing the prompt critical fission process that creates the WMD. When comparing current chemical explosives to a nuclear explosion, truly the only term that these processes share is the term explosion.

Chemical Explosives can be characterized based upon the energy distribution released during detonation. This distribution can be divided into two portions; the first being kinetic energy and the other being internal energy. Kinetic energy is defined by the energy or motion of electrons, atoms, and molecules. Internal energy is defined by the internal energy of the previously mentioned particles. As electron bonds are broken during the explosion, the internal change that the atoms or molecules experience is the internal energy. Nuclear weapons have both of these energy components; however, the nuclear reaction that begins the fission process adds the thermal radiation component. The thermal radiation emitted from the WMD is what creates the drastic difference between nuclear and chemical explosives[22].

Current chemical explosives utilize the breaking of chemical bonds to release energy. Since the chemical interactions depend on the breaking of electron bonds between molecules, the resulting energy released per reaction is relatively 1E6 cal/kg of material. The temperature that is achieved during this type of reaction only achieves a maximum temperature of 5,000^{o}K.

However, when dealing with fission type nuclear weapons, the nuclear reactions that occur release 1E6 times more energy per reaction when compared to conventional chemical explosives. Therefore, the amount of nuclear material required to produce an equivalent chemical explosion is significantly decreased. Due to the large amount of energy released per

reaction, the energy per kg release rate is roughly 1E13 cal and the weapon can achieve temperatures of 1E7—5E7 K. Table 4-1 shows a brief overview of the energy released from chemical and nuclear weapons.

Table 4-1: An overview of a Chemical Explosion versus Nuclear Explosion[23]

Chemical versus nuclear explosions.		
	Chemical	Nuclear
Yield	1x10^6 cal	1x10^13 cal
Fuel Mass Consumed	1kg	1kg
Temperature	5000K	1 ×10^7 →5 ×10^7 K
Burning Time	1x10^-5 sec	1x10^-7 sec
Specific Heat	200 cal/kg-K	1x10^6 cal/kg-K

The aforementioned temperatures are achieved quickly and create a significant increase in pressure. The materials that are near the core of the WMD are quickly heated causing the orbital shell electrons to be stripped and creates a plasma. The atomic imbalance accelerates these freed electrons exponentially resulting in Bremsstrahlung radiation. This creates an increase in electromagnetic radiation resulting in a mix of gamma rays, x-rays, heat radiation, infrared, visible light, and ultraviolet. The x-rays are what deposits most of the energy onto the face of the structures inside the fireball. The photon and electron burst make up 70% - 80% of the energy expended during a WMD detonation. [23]. Table 4-1 shows the energy distribution for nuclear weapons.

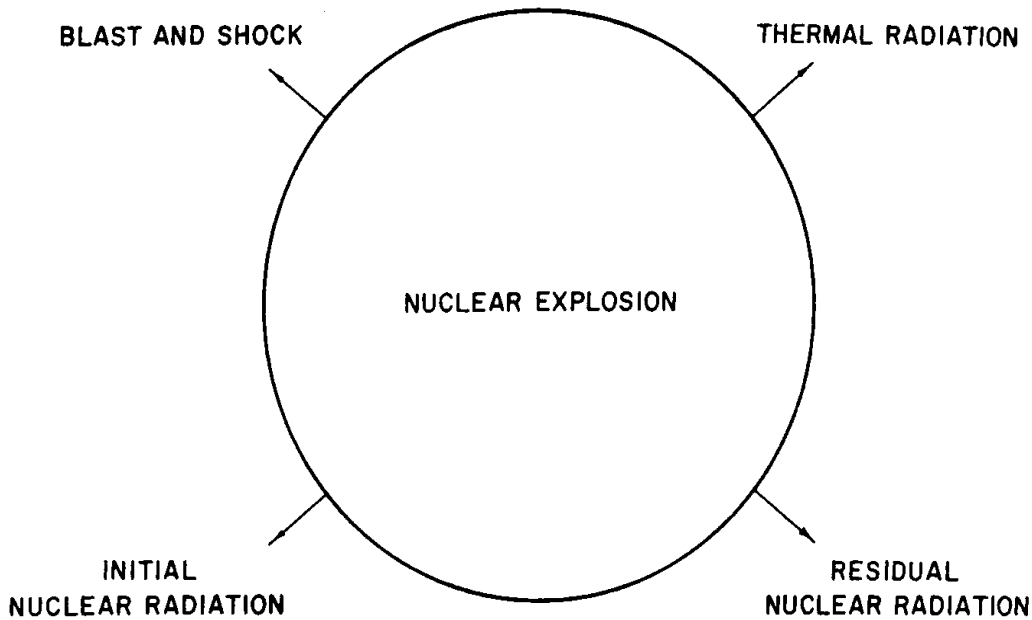

Figure 4-1: Distribution of energy from a fission style WMD [21]

Varying Types of Bursts

When evaluating nuclear weapons burst, the location of the detonation drastically changes the energy deposition to the surrounding area. This also affects the resulting melt glass matrix that forms after the detonation. The funding for this research is focused on nuclear security with respect to terrorism response. The most likely scenario in which a fission type WMD will be detonated is a surface burst. [23]

Air Burst

An air burst is a weapon that is detonated at an altitude such that the fireball does not touch the surface of the earth. Because the thermal radiation burst gets absorbed before interacting with the earth's surface, the only aspect of the weapon that inflicts damage is from the blast front and pressure wave. Subsequently the air in the atmosphere surrounding the weapon rapidly expands creating a pressure wave. The pressure wave is what interacts with the earth's surface. Since the fireball does not make contact, little to no melt glass is formed during this event. Due to the challenges faced with creating a successful airburst, this burst was not modeled in the NUKES code.

Underwater Burst

An underwater burst is a weapon that is detonated in water. The depth can range from a shallow detention (roughly the surface of the water), to depths exceeding 1000m. Depending on the location of the underwater burst, the thermal radiation is mostly attenuated and significantly hinders that growth of the fireball. However; if the weapon is detonated at the surface of the water, the blast dynamics of the weapon will behave similarly to a surface burst. Therefore, if ships, harbors, or other urban environments are taken into the blast radius, this debris will create a matrix similar to trinitite. Due to the complexity of modeling the fluid dynamics of water, which is beyond the scope of this thesis, water burst will be molded as surface burst in the NUKES code.

Underground Burst

An underground burst is a weapon that is detonated beneath the surface of the earth. It is challenging to differentiate between an underground burst and a shallow surface burst. As shown in Eq. 5-1 the depth of the crater, Dc, in an underground burst is dependent solely upon the yield of the weapon. If the depth of burst (DOB) exceeds the Dc, then it is an underground burst. Dc is the required depth to be classified as an underground burst and *W* is the yield of the weapon.

$$Dc = 5 * W^{0.3} \tag{5-1}$$

Most of the thermal radiation is contained in the cavity that weapon creates during detonation. The soil moderates the electromagnetic radiation that is emitted from the weapon, and only small amounts of dust and melt glass are ejected from the test. The challenge in modeling this type of burst is in understanding the temperature and pressure effects upon the thermal radiation. Due to the containment, the temperatures and pressures can drastically increase which will affect the thermal radiation and soil moderation. Although the threat of an Improvised Nuclear Device, (IND) being detonated in a subway system or in the sub-urban infrastructure is probable, more study understanding the properties of an underground burst must be determined.

Surface Burst

A Surface burst is a weapon that is detonated at or around the surface of the earth. If a weapon is detonated and the fireball touches the surface of the earth or if the weapon is detonated at a depth less than the distance specified in Eq.5.1, then the resulting detonation is a surface burst. Since the majority of the thermal radiation interacts with either the air or the surrounding environment this would theoretically be the best burst to model. Also, the probability is high that a terrorist group would detonate a fission type WMD at or near the surface burst range. Either in a sub-urban infrastructure or in a building, the surface burst is the most likely type of detonation. After creating a surface burst model for urban detonations, the results can be verified with the trinitite that was collected after the Trinity test.

Surface Burst Selection

As stated previously the surface burst is the most probable method of detonation in regards to a terrorist group. Therefore, the code models only surface bursts. Also, due to the challenges associated with creating a hydrogen weapon, it will be assumed that the design of the weapon is a fission style weapon. The assumed model will work similarly to the U-235 gun type weapon used during World War II. Fig.5.2 shows a schematic of the weapon design that is modeled.

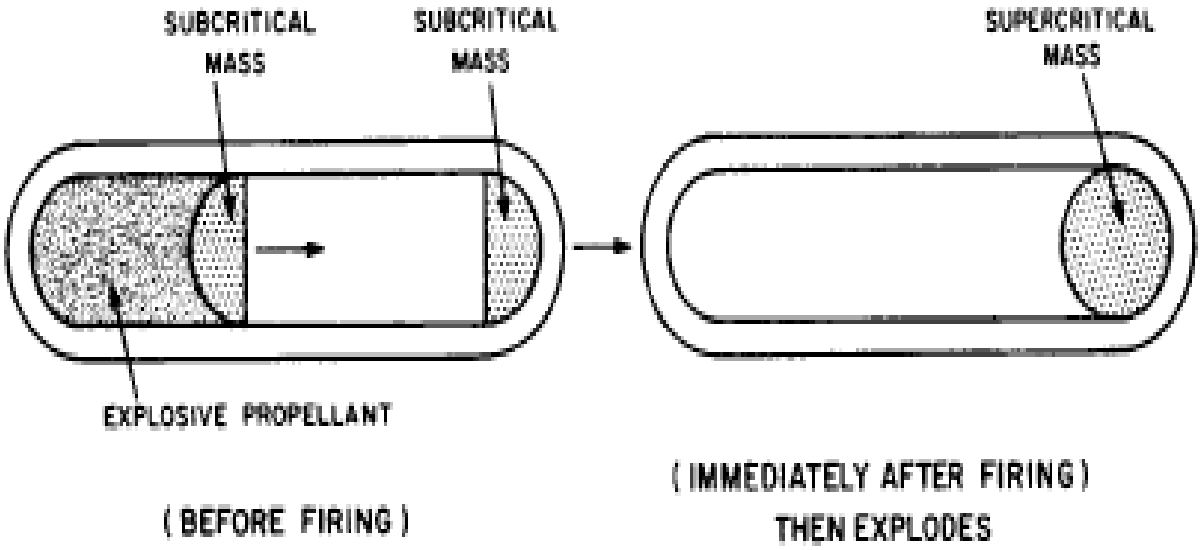

Figure 4-2: A diagram of the gun type design of a fission weapon [22]

Detonation Process

Neutron Production

The gun type fission device is the simplest design for nuclear weapons. Therefore, it is assumed that this style of device would be used during a terrorist attack. The gun type weapon has two sub-critical masses setting at each end of a barrel. One of the sub-critical masses will be rapidly accelerated toward the other by using a high explosives. As the two half spheres collide, the apparatus instantly attains a prompt critical state. The initial neutron flux that is created from special nuclear material (SNM) rapidly generates a mixture of gamma rays and neutrons (Figure 4-3). On average, roughly 2.53 neutrons are emitted per collisions with the SNM.

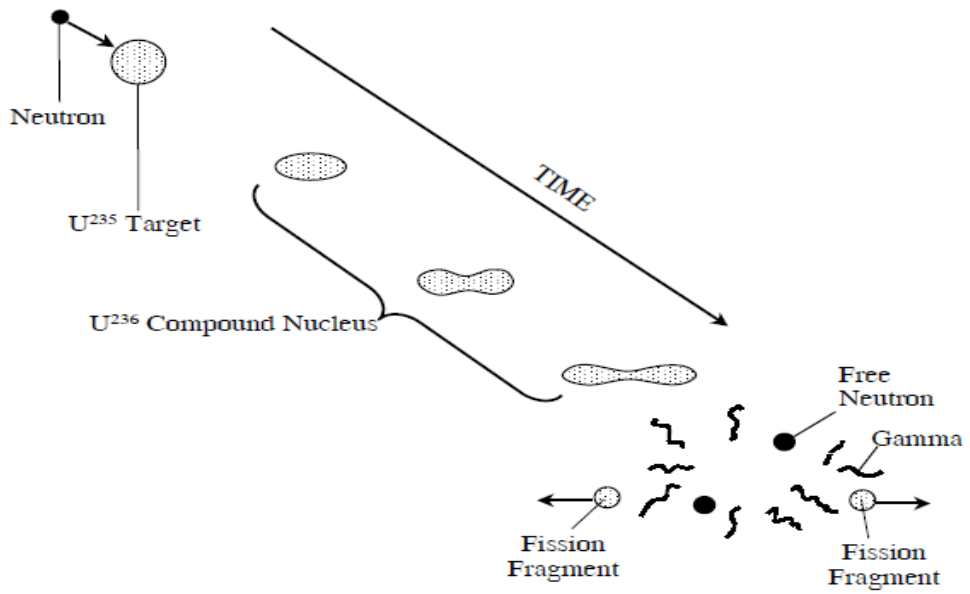

Figure 4-3: The initial reaction that kick-starts the fission reaction[23]

As shown in Table 4-2, the number of neutrons that are released within the first microsecond exponentially increases, incidentally, forcing the number of fission fragments that are created to also increase exponentially. On average the energy released per neutron caused fission is 2.5E6 joules of energy per reaction. Therefore, the temperatures achieved within the first microsecond rival the temperatures of the sun (1E7 K). The fission process continues until the Special Nuclear Material (SNM) vaporizes and loses critical geometry. This process stops around the 61st generation of neutrons, at which point the SNM has become a gas as shown in Table 4-3.

Table 4-2: Neutron population of a bare plutonium sphere with a 2cm reflector of U-238[23]

g	k	burnup	neutron population	yield (KT)	surface velocity	radius
1	1.85	0	2.35E+03	0.00E+00	0.00E+00	0.035
5	1.85	0	7.16E+04	5.42E-19	3.01E-04	0.035
10	1.85	0	5.13E+06	4.01E-17	2.59E-03	0.035
15	1.85	0	3.67E+08	2.87E-15	2.19E-02	0.035
20	1.85	0	2.63E+10	2.05E-13	1.85E-01	0.035
25	1.85	0	1.88E+12	1.47E-11	1.57E+00	0.035
30	1.85	0	1.34E+14	1.05E-09	1.33E+01	0.035
35	1.85	0	9.62E+15	7.52E-08	1.12E+02	0.035
36	1.85	0	2.26E+16	1.77E-07	1.72E+02	0.035
37	1.85	0	5.31E+16	4.15E-07	2.63E+02	0.035
38	1.85	0	1.25E+17	9.75E-07	4.04E+02	0.035
39	1.85	0	2.93E+17	2.29E-06	6.19E+02	0.035
40	1.85	0	6.87E+17	5.38E-06	9.48E+02	0.035
41	1.85	0	1.61E+18	1.26E-05	1.45E+03	0.035
42	1.85	0	3.78E+18	2.96E-05	2.23E+03	0.035
43	1.85	0	8.86E+18	6.95E-05	3.41E+03	0.035
44	1.85	0	2.07E+19	1.63E-04	5.22E+03	0.035
45	1.84	0	4.84E+19	3.81E-04	7.98E+03	0.035
46	1.84	0	1.12E+20	8.88E-04	1.22E+04	0.035
47	1.83	0	2.60E+20	2.06E-03	1.86E+04	0.035
48	1.82	0	5.97E+20	4.77E-03	2.82E+04	0.035
49	1.8	0	1.35E+21	0.01	4.28E+04	0.035
50	1.76	0	3.00E+21	0.02	6.43E+04	0.036
51	1.71	0	6.44E+21	0.05	9.57E+04	0.036
52	1.63	0.001	1.32E+22	0.12	1.40E+05	0.037
53	1.49	0.002	2.47E+22	0.24	2.00E+05	0.038
54	1.25	0.004	4.05E+22	0.45	2.75E+05	0.04
55	0.87	0.006	5.20E+22	0.76	3.57E+05	0.044
56	0.5	0.009	4.57E+22	1.09	4.26E+05	0.049
57	0	0.011	2.77E+22	1.33	4.71E+05	0.061

Table 4-3: The change of material phase depending upon the temperature and generation

Generation	Yield/Mass (cal/g)	Temperature (K)	Phase or State
1	6.66E-13	293	alpha
5	3.49E-11	293	alpha
10	2.53E-09	293	alpha
15	1.80E-07	293	alpha
20	1.29E-05	293	alpha
25	9.18E-04	293	alpha
30	6.54E-02	296	alpha
31	0.2	299	alpha
32	0.4	307	alpha
33	0.8	327	alpha
34	2	373	alpha
35	4.6	416	beta
36	10.9	645	delta
37	25.6	1154	liquid
38	60	3528	liquid/gas
39	140.8	3528	liquid/gas
40	330.2	15073	gas
41	774.5	50613	gas

Fission Fragments

From the time that the SNM is pushed into a critical state until the 61st generation of neutrons, high energy gammas and large amounts of fission fragments are produced. Although these gamma rays add to the total spectra of photon energies, the fission fragments generate the most energy inside the weapon (Table 4-4). The fission fragments normally follow a distribution with atomic number around 92 and 150 (Figure 4-4). In higher atomic number elements, the number of electrons is correspondingly higher in the orbital shells. As the temperature quickly increases these electrons are released from the atom thus generating the atomic energy portion of the weapon.

Table 4-4: Shows the distribution of fission energy from either U-235 or Pu-239[23]

Energy Form	U-235	Pu-239
Fission Fragment Kinetic Energy	168	172
Neutron Kinetic Energy	5	6
Prompt Gamma Energy	7	7
Total Prompt Energy (Mev)	180	185
Delayed Beta Energy	8	8
Delayed Gamma Energy	7	7
Anti-neutrino Energy	12	12
Total Delayed Energy (Mev)	27	27
Total Energy Per Fission (Mev)	207	212

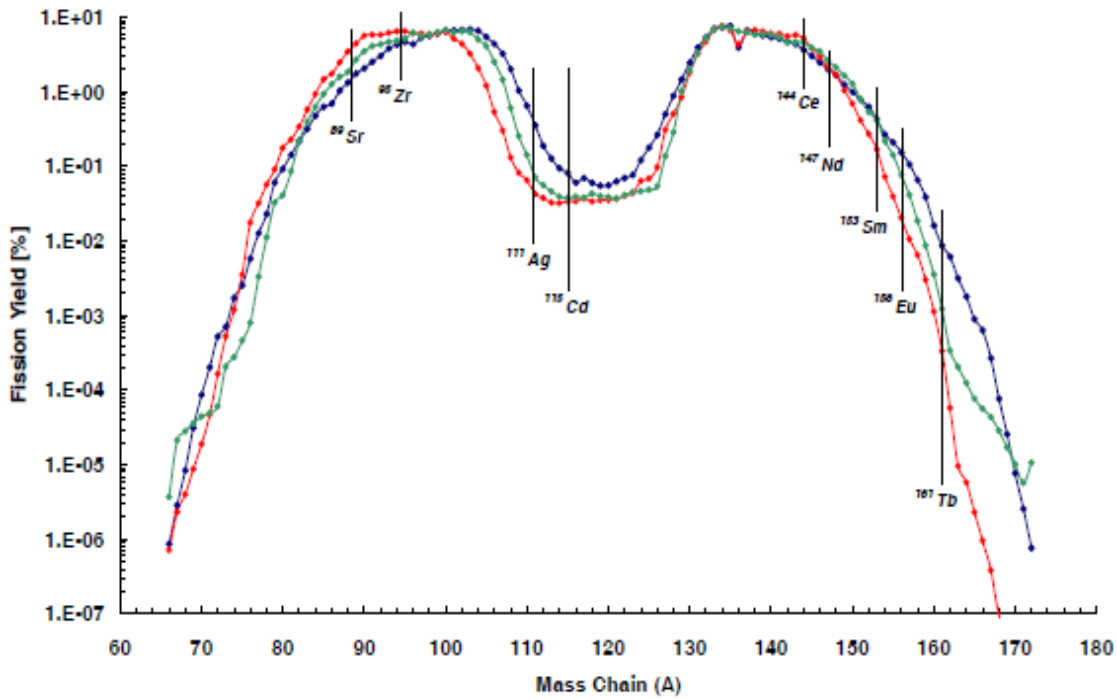

Figure 4-4: The fission fragment distribution from a prompt critical Plutonium apparatus[23]

Electron Production

On average the energy released per neutron caused fission is 2.5E6 joules of energy per reaction. Therefore, the temperatures achieved within the first microsecond rival the temperatures of the sun (1E7 K). The numerous nuclear reactions and high temperatures strip all the orbital shell electrons of the nucleus. This creates a charge imbalance in the nucleus which further accelerates the recently liberated electrons. The electrons bend around the magnetic field created by the charged nucleus creating Bremsstrahlung radiation (or breaking radiation). As the electrons bend around nucleus, they slow down, therefore releasing a broad spectrum of electromagnetic radiation. These electrons and electromagnetic radiation would be defined as atomic reactions instead of a nuclear reaction. Table 4-5 shows the number of electrons potentially released from a plutonium atom as a function of time. Mathematically speaking, the numbers of free electrons quickly outnumber the number of neutrons and fission fragments.

Table 4-5: The number of orbital shell electrons released from Pu atoms as a function of temperature [23]

Temp		Average Number of Bound Electrons by Orbit								Free Electrons per atom
degrees	eV	K	L	M	N	O	P	Q	R	
0	0.0	2.0	8.0	18.0	32.0	23.0	9.0	2.0	0.0	0.0
5x105	43.0	2.0	8.0	18.0	32.0	34.0	0.0	0.0	0.0	0.0
8x105	69.0	2.0	8.0	18.0	32.0	31.8	0.5	0.6	0.8	0.2
1x106	86.0	2.0	8.0	18.0	32.0	24.4	2.1	2.8	3.5	2.2
2x106	172.0	2.0	8.0	18.0	31.5	5.4	5.0	6.6	8.4	9.3
5x106	431.0	2.0	8.0	18.0	8.3	5.3	5.4	7.1	0.0	40.1
8x106	690.0	2.0	8.0	18.0	3.3	3.1	3.5	4.6	0.0	51.9
1x107	862.0	2.0	8.0	18.0	2.2	2.6	2.7	3.5	0.0	55.6
2x107	1732.0	2.0	8.0	17.1	0.7	0.8	1.1	1.4	0.0	63.4
5x107	4310.0	2.0	6.8	0.8	0.2	0.3	0.4	0.5	0.0	83.2
8x107	6900.0	2.0	1.1	0.2	0.1	0.1	0.2	0.2	0.3	89.8
1x108	8620.0	2.0	0.4	0.1	0.1	0.1	0.1	0.2	0.2	90.8
2x108	17200.0	1.0	0.0	0.0	0.0	0.0	0.1	0.1	0.1	92.7
5x108	43100.0	0.1	0.0	0.0	0.0	0.0	0.0	0.0	0.0	93.9

Photon Production

As previously discussed the number of free electrons inside the plasma of the fireball is large; and subsequently the number of photons emitted from the electron transitions is very high. Roughly 80% of the damage created by the nuclear weapon is generated from the electromagnetic radiation from these free electrons [23]. The purpose of the NUKES code is to accurately model the fireball propagation in an urban environment and predict the buildings that are vaporized thus adding to the urban matrix. Figure 4-5 shows the Maxwell-Boltzmann Speed distribution of the particle speeds that occur inside the fireball at generation 40 and 41. The weapon depending upon construction will begin to vaporize at this point, which will stop

the fission process. Therefore, the surface temperature of the fireball will closely match the 50,613°K used for the particle speed distribution (see Figure 4-6). Depending on the size of yield from the WMD, the distribution under the peak will broaden, but the speeds achieved by the particles will be assumed to not increase.

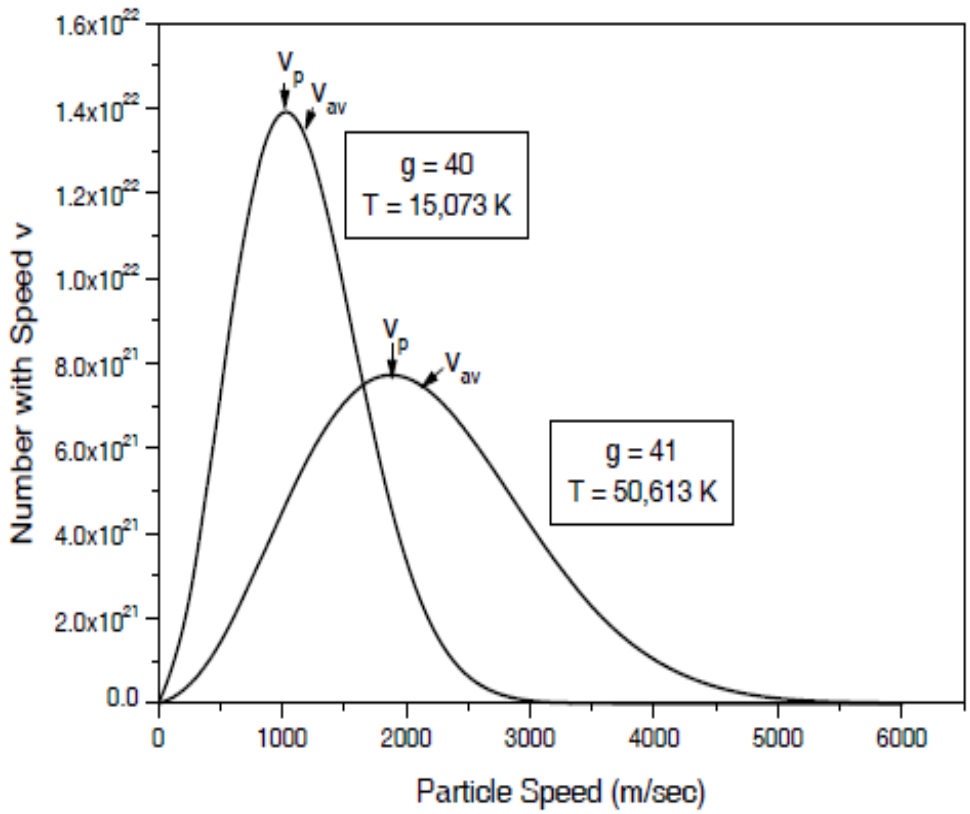

Figure 4-5: The Maxwell-Boltzmann distribution of particle speed during a fission detonation[23]

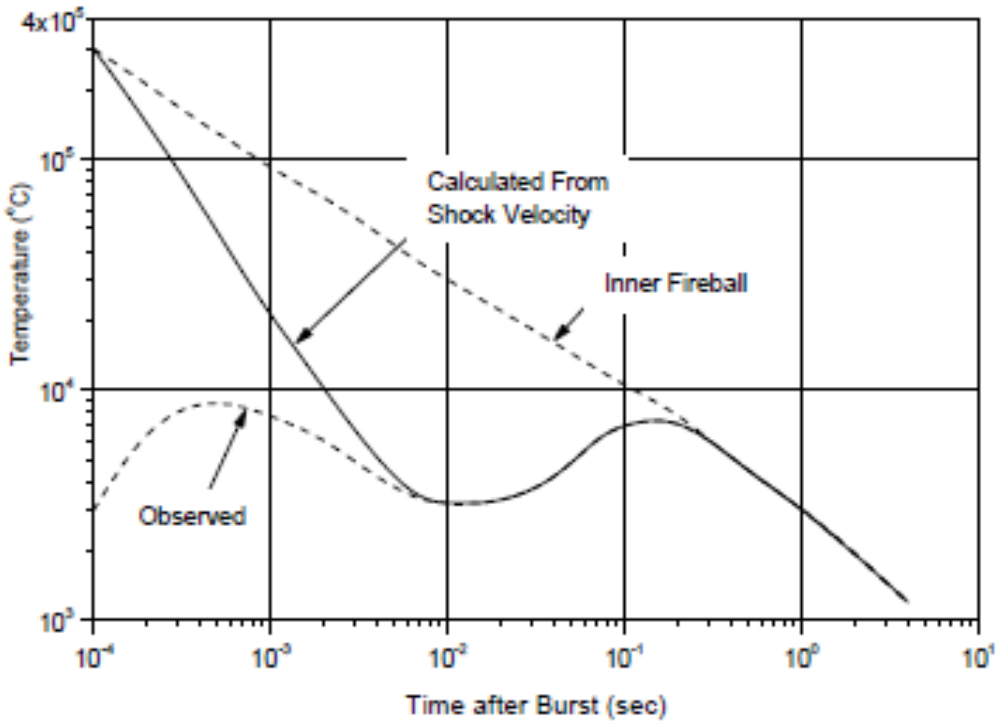

Figure 4-6: Fireball surface temperature as a function of time after a 20KT burst [23]

Chapter Summary

After an in-depth investigation of the WMD fission process, it can be assumed that the electromagnetic radiation emitted from the fission fragments accounts for 80% of the energy interaction with the urban environment. Also, the speeds of the neutrons, fission fragments, and electrons do not match the photon speeds, and the mean free path of the particles emitted from the weapons (neutrons, alphas, and fission fragments) are significantly shorter than the photons. Therefore, the photons have a higher probability of traveling far enough to interact with the surrounding environment. They will deposit all their energy on the urban structure before the particles interact with any portion of the environment. From these conclusions, the fireball growth and energy deposition will only account for the photon and blackbody radiation from the weapon.

Chapter 5: Blast Calculations

Introduction

As discussed in the previous chapter, fission starts the process. This causes the SNM to fission, thus causing a tremendous number of neutrons to be generated. The neutrons, in conjunction with the elevated temperatures and pressures, strip those orbital shell electrons off the atom. These free electrons, as they move around the nucleus, create a magnetic imbalance of the nucleus forcing the electrons to bend around nucleus. This bend causes the electrons to decelerate forcing them to emit high energy photons. The spectrum of photons varies by the yield of the weapon, but the photon spectrum is comprised of gamma, x-ray, ultraviolet, visible, and infrared radiation. Since 85% of the damage done to the environment is from the photon burst, NUKES only model the photon deposition in the urban area. This chapter discusses the equations used to model this blast effect. According to Glasstone et.al [22] these blast calculations can be assumed to be accurate within 25% error.

Electron and Photon Energy Range

Since the electrons that are freed from the nucleus are from the orbital shells, the amount of energy contained in these electrons is lower when compared to nucleus electrons. Also, the surface temperature of the fireball will statistically not exceed the temperatures attained from generations 40 and 41. Toward the center of the fireball the temperatures are roughly 1E7 K, which will excite the photons to a higher energy potential (see Figure 5-1). However, as temperatures decrease, the energy range of the photons that cause damage is between 120 eV to 120 keV. Thus, the electromagnetic radiation emitted from these electrons will most likely be equal to or less than an x-ray energy. Per Figure 5-2, the photon distribution will follow a Planckian energy distribution.

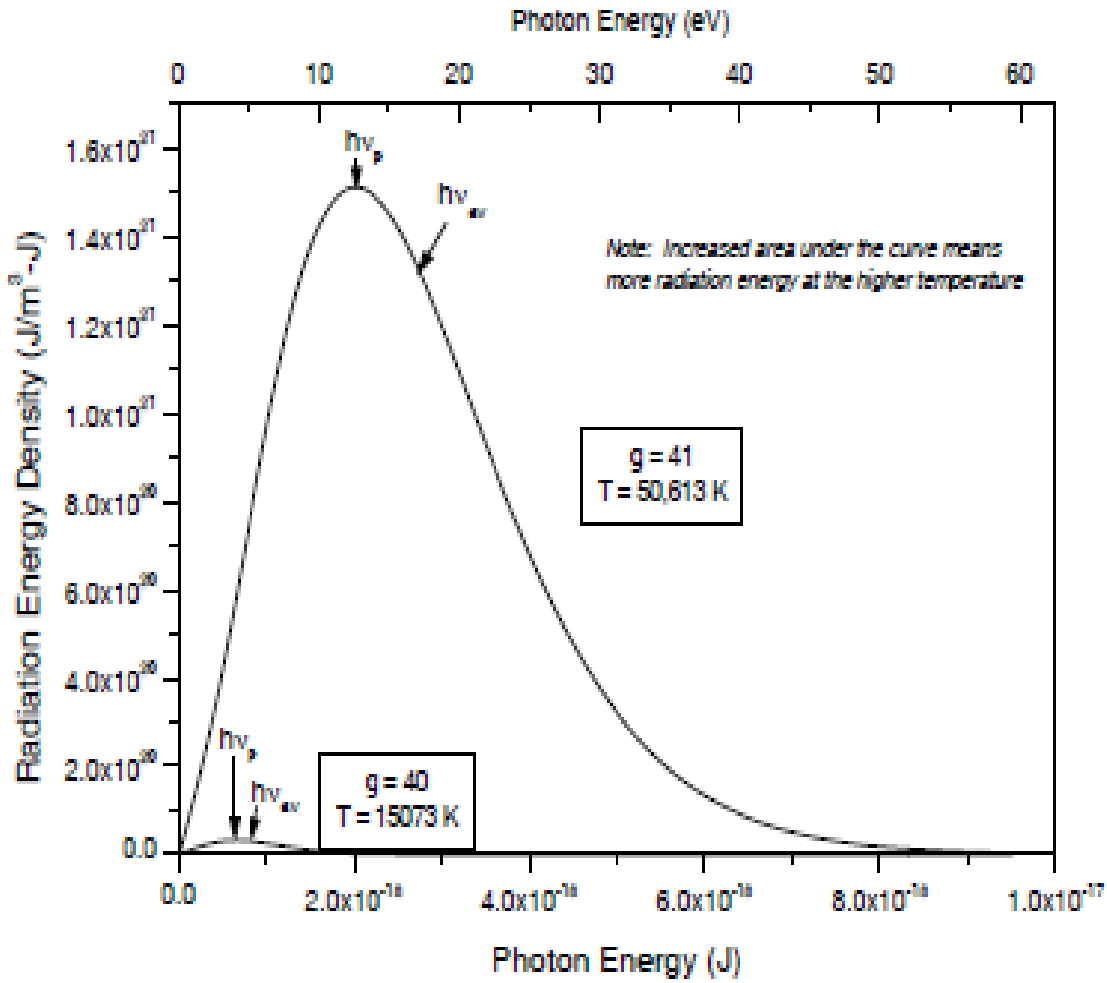

Figure 5-1: The Planckian energy distributions of photons emitted from a nuclear weapon at generations 40 and 41 [23]

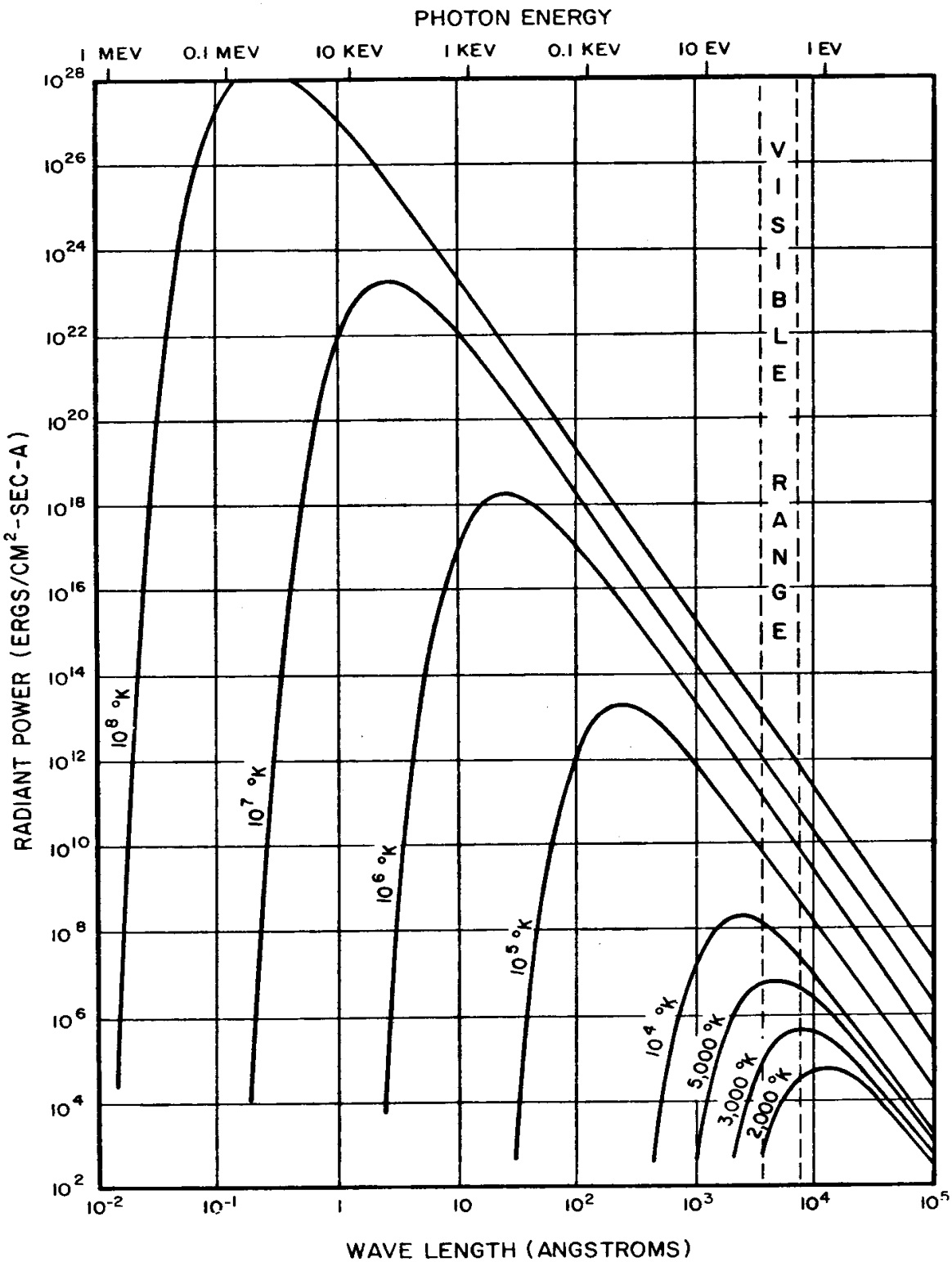

Figure 5-2: The radiant power of black-body radiation as a function of wavelength, energy and temperatures [21]

Photon Energy Deposition Calculations

Normally, standard black-body radiation of longer wavelength, roughly 5,500A or larger, corresponds to higher black-body radiation deposition. However, a nuclear weapon fireball does not behave in a manner resembling other black-body problems. As shown in Figure 5-2, the photon energy deposition is dependent upon wavelength and temperature. Therefore, with certain assumptions the black-body problem can be used as an accurate model for fireball growth and thermal radiation emission characteristics. In standard black-body problems, Planck's radiation equation (Eq. 5-1) can be used to calculate the rate of radiant energy transfer as a function of temperature and wavelength, where *h* is Plank's constant, *c* is the speed of light, λ is wavelength in angstroms, *K* is Boltzmann's constant, and *T* is in absolute temperature.

$$E_\lambda = \frac{8\pi hc}{\lambda^5} * \frac{1}{e^{\frac{hc}{\lambda KT}} - 1} \tag{5-1}$$

By integrating this equation over the energy distribution from 0 to infinity, it is possible to find total energy deposition. Equation 5-2 shows this relationship where *dλ* is the incremental change in wavelength.[21]

$$E_T = E_\lambda * d\lambda \tag{5-2}$$

From this equation, it is important to calculate the fluence of energy deposition of the weapon with respect to the wavelength. Equation 5-3 shows this relationship where J_A is in units of energy (ergs) per unit area (cm^2) per unit time (s), *c* is the speed of light, and E_λ is the energy transfer of the photons.

$$J_\lambda = \frac{c}{4} E_\lambda \tag{5-3}$$

Mean Free Path Assumptions

Toward the center of the fireball the temperatures are roughly 1E7 K. Since the electrons that are freed from the nucleus are from the orbital shells, the amount of energy contained in these electrons is lower than compared to nucleus electrons. Also, the surface temperature of the fireball will statistically not exceed the temperatures attained at generation 40 and 41. However, as temperature decreases, the energy range of the photons that cause damage is between 120 eV to 120 keV. Thus, the electromagnetic radiation emitted from these electrons will mostly be equal to or less than x-ray energy. This is the basis of the statement made earlier that the primary thermal radiation from a nuclear explosion consists largely of X-rays. As previously established, the energy of the photon depends upon the wavelength. Therefore, to develop accurate blast capabilities the photon deposition was adjusted to function with respect to temperature. The thermal radiation received at a distance from a nuclear explosion is assumed to be characteristic of a black-body at a temperature of about 6,000 to 7,000^{o}K, although somewhat depleted in the ultraviolet and other shorter wavelengths.

It is important for accurate blast calculations that the wavelength modeled matches the temperature of the blast. Therefore, it is assumed that the wavelength corresponds with the hottest portion of the surface of the fireball. Thus Eq.4 is the result of differentiating Eq. 5-4 with respect to the wavelength and setting the result equal to 0. In this equation λ_m is the maximum wavelength achieved during the blast at a specified temperature, *C* is a constant equal to 2.90E7.

$$\lambda_m = \frac{C}{T} \tag{5-4}$$

Additionally, it is assumed that the air is at standard room temperature during the blast, and the mean free path is adjusted when the photons are traveling through the materials. However, the average mean free path of the photons ranging from 0.5 keV to 15 keV can be averaged to the following equation, where E is the average photon energy in keV.

$$Mean\ Free\ Path \approx \frac{E^3}{5} cm \tag{5-5}$$

After calculating the photon distributions and mean free paths for the photons, the final process was to calculate the radiant exposure rate to the buildings as a function of solid angle. To simplify the model, the blast was treated as a point source emitting radiation isotopically. Therefore, the energy flux received from the fireball was determined by Eq. 5-6, where E_{tot} is the total energy from the weapon, and *D* is the distance from the buildings.

$$E_R = \frac{E_{tot}}{4\pi D^2} \tag{5-6}$$

Next, it is important to determine the attenuation coefficients surrounding the burst. This drastically affects radiation exposure rate. Starting from an initial assumption that the atmosphere is uniform, a simple modification can be made to Eq.5.6 to account for the atmospheric attenuation. Eq.5-7 shows the factor added to account for uniform attenuation, where *K* is an average attenuation coefficient, D is the distance from the buildings, and E_{tot} is the energy from the weapon. Also E_R is changed to *Q* to represent the radiant energy exposure with units of energy per unit squared.

$$Q = \frac{E_{tot}}{4\pi D^2} * e^{-xD} \tag{5-7}$$

Sadly, the urban environment in which most weapons are detonated cannot be treated as a uniform atmosphere; therefore, Eq. 5-7 was altered to account for the scattering and attenuation caused by the urban environment. The transmittance factor τ was added to Eq. 5-7, which factors in distance traveled by the radiation, the radiation that is absorbed, and the radiation that is scattered. Another form in which E_{tot} can be written is $E_{tot} = fW$. This changes the energy calculations to be a function of yield instead of just energy, and the *f* determines the thermal partition of the radiation depending on whether it is an air or surface burst.

$$Q = \frac{fW\tau}{4\pi D^2} \tag{5-8}$$

The values used for the transmittance and thermal partition are observed values obtained from Glasstone's, *The Effects of Nuclear Weapons*[21]. The transmittance values were calculated from the data in Figure 5-3, and the thermal partition values for a surface burst is given in Table 5-1.

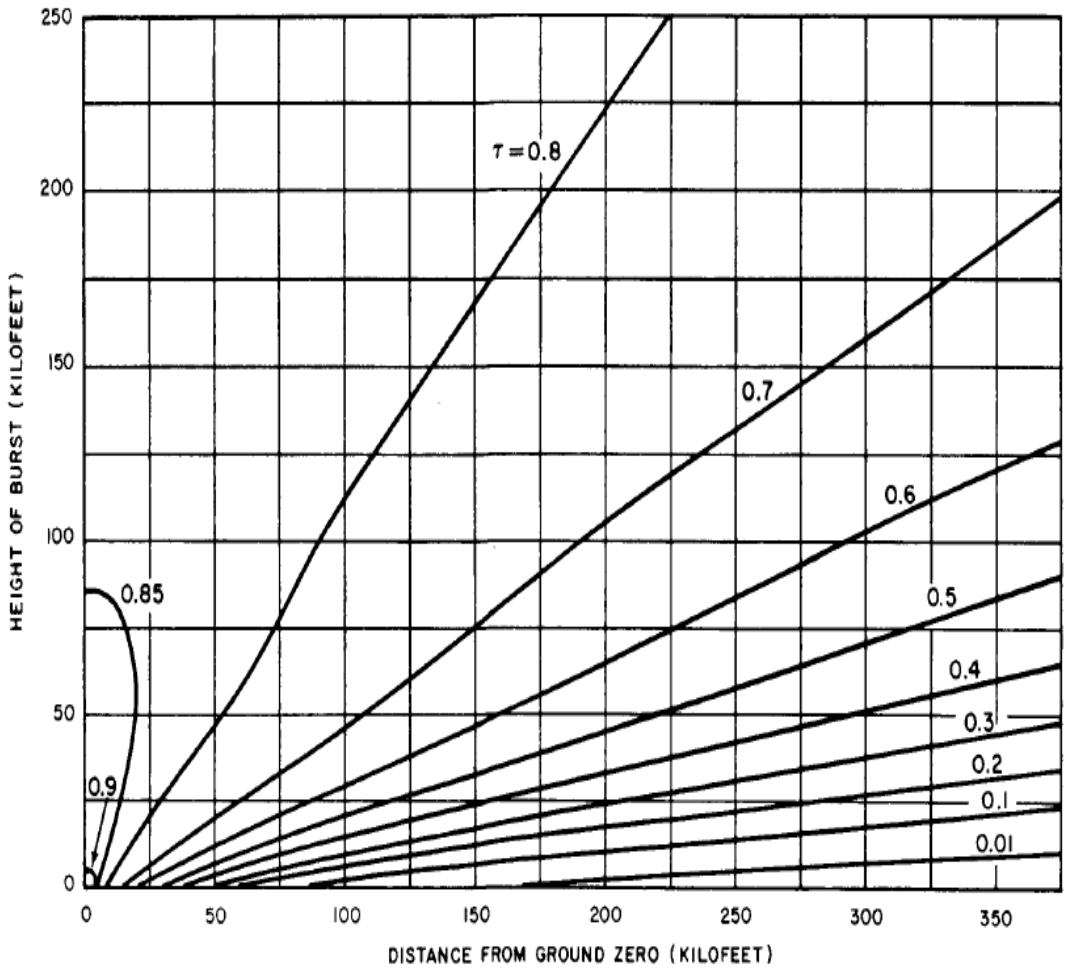

Figure 7.98. Transmittance, τ, to a target on the ground on a typical clear day (visibility = 12 miles).

Figure 5-3: The transmittance factor to a target on a clear day *[21]*

Table 5-1: The thermal partition factor (f) for varying bursts *[21]*

	Total Yield in KT				
Height of Burst (M)	I	10	100	I,000	10,000
20	0.19	*	*	*	*
40	0.21	0.19	*	*	*
70	0.23	0.21	0.19	*	*
100	0.26	0.22	0.2	*	*
200	0.35	0.25	0.21	0.19	*
400	**	0.33	0.25	0.21	0.19
700	**	**	0.28	0.24	0.21
1,000	**	**	0.34	0.26	0.22
2,000	**	**	**	0.34	0.26
4,000	**	**	**	**	0.33
7,000	**	**	**	**	0.35
*These may be treated as contact surface burst, with f=0.18					
** See another table					

Chapter Summary

After finding the radiation exposure rate for surface bursts, it is possible to calculate the energy deposition on the face of buildings. By using a mesh for each building modeled, NUKES, systematically steps through a building accounting for material and mass to determine if the building is vaporized, thus adding to the final urban debris matrix. This also prints out a map of the damaged or vaporized buildings from the NUKES code. This helps other developers improve on shock wave propagation and large particulate distribution. Although some of the assumptions made are broad, the NUKES code is based upon overserved data from nuclear tests. Also, this helps to shorten computational time for running the code.

Chapter 6: Building Library

Overview of Chapter

This is an overview of the buildings that were selected to be modeled in NUKES. This chapter discusses why these particular type of buildings were chosen, the composition of these buildings, and the library that was constructed to interface with NUKES.

Introduction

In order to produce a code that accurately predicts urban debris composition for nuclear forensic application, the urban environment where the weapon is detonated must be modeled accurately. Due to the significant increase in building size in numerous US cities, the building size and structure would alter the fireball propagation; therefore, changing the composition of the debris.

Making the Library

To build this library, the first thing that had to be compiled was the number of buildings that would be modeled in the code. The Energy Information Administration (EIA) has compiled a table (Table 6-1) that highlights the different buildings located in an urban environment.[24]

Table 6-1: Shows the various buildings recognized by the EIA in an urban environment

Building type	Definition	Includes these sub-categories from the CBECS questionnaire
Education	Buildings used for academic or technical classroom instruction, such as elementary, middle, or high schools, and classroom buildings on college or university campuses. Buildings on education campuses for which the main use is not classroom are included in the category relating to their use. For example, administration buildings are part of "Office," dormitories are "Lodging," and libraries are "Public Assembly."	elementary or middle school, high school, college or university, preschool or daycare, adult education, career or vocational training, religious education
Food Sales	Buildings used for retail or wholesale of food.	grocery store or food market, gas station with a convince store, convenience store
Food Service	Buildings used for preparation and sale of food and beverages for consumption.	fast food, restaurant or cafeteria, bar, catering service or reception hall, coffee, bagel, or doughnut shop, ice-cream, or frozen yogurt shop
Health Care (Inpatient)	Buildings used as diagnostic and treatment facilities for inpatient care.	hospital, inpatient rehabilitation
Health Care (Outpatient)	Buildings used as diagnostic and treatment facilities for outpatient care. Medical offices are included here if they use any type of diagnostic medical equipment (if they do not, they are categorized as an office building).	medical office (see previous column), clinic or other outpatient health care, outpatient rehabilitation, veterinarian
Lodging	Buildings used to offer multiple accommodations for short-term or long-term residents, including skilled nursing and other residential care buildings.	motel or inn, hotel, dormitory, fraternity, sorority, retirement home, nursing home, assisted living, other residential care, convent, monastery, shelter, orphanage, children's home, halfway house
Mercantile	Buildings used for the sale and display of goods other than food.	retail store, liquor store, rental center, dealership, studio gallery
Mercantile	Shopping malls comprised of multiple connected establishments.	enclosed mall, strip shopping center
Office	Buildings used for general office space, professional office, or administrative offices. Medical offices are included here if they do not use any type of diagnostic medical equipment (if they do, they are categorized as an outpatient health care building).	administrative or professional office, government office, mixed-use office, bank, financial institution, medical office, sales office, contractors office, non-profit services, city hall, city center, religious office, call center
Public Assembly	Buildings in which people gather for social or recreational activities, whether in private or non-private meeting halls.	community center, lodge, meeting hall, convention center, senior center, gymnasium, health club, bowling, alley, ice rink, field house,

Building type	Definition	Includes these sub-categories from the CBECS questionnaire
		museum, theater, cinema, sports arena, casino, night club, library, funeral home, student activities, armory, exhibition hall, broadcasting studio, transportation terminal
Public Order and Safety	Buildings used for the preservation of law and order or public safety.	police station, fire station, jail, reformatory, penitentiary, courthouse, probation office
Religious Worship	Buildings in which people gather for religious activities, (such as chapels, churches, mosques, synagogues, and temples).	No subcategories collected
Service	Buildings in which some type of service is provided, other than food service or retail sales of goods	vehicle service, repair shop, vehicle storage/ maintenance, dry cleaner or laundromat, post office, postal center, car wash, gas station, photo processing shop, beauty parlor, barber shop, tanning salon, copy cneter, printing shop, kennel
Warehouse and Storage	Buildings used to store goods, manufactured products, merchandise, raw materials, or personal belongings (such as self-storage).	refrigerated warehouse, non-refrigerated warehouse, distribution center
Other	Buildings that are industrial or agricultural with some retail space; buildings having several different commercial activities that, together, comprise 50 percent or more of the floor space, but whose largest single activity is agricultural, industrial/ manufacturing, or residential; and all other miscellaneous buildings that do not fit into any other category.	airplane hangar, crematorium, laboratory, telephone switching, agriculture, manufacturing, data center, sever farm
Vacant	Buildings in which more floor space was vacant than was used for any single commercial activity at the time of interview. Therefore, a vacant building may have some occupied floor space.	No subcategories collected, but a question was asked to determine whether the building was completely vacant

Due to the large number of buildings that is recognized by the EIA, a commonality between these buildings was found to limit the number of options posed to the user. The commonalities were based upon power consumption, building use, design, and size. Once the

urban categories were selected, these categories were used to evaluate the structures at the Nevada Test Site (NTS).[21] By utilizing actual structures that were affected by nuclear weapons, this helped to develop a better model for damage. The Urban categories were also used to find relevant information pertaining to the construction materials used in the buildings. After conducting this comparison and reading these studies, Table 6-2 shows the selected buildings with the average size and purpose. [25]

Table 6-2: Shows the Data from a sample of buildings found in various cities. [26]

	CS1	CS2.1	CS2.2	CS2.3	CS3	CS4
Building Use	Residential	Administration Hospital	Hospital	Hospital	Industrial Production	Commercial Residential
Construction Material	Reinforced Concrete	Brickwork	Reinforced Concrete, Brickwork	Reinforced Concrete	Steel, Brickwork	Brickwork
Completion	1970	1870	1960	2003	1900	1859
Gross Volume (m3)	60000	62000	7200	11000	21000	37000
Gross Floor Area (m2)	18000	13400	2200	2500	3900	1100

After the types of buildings were selected multiple studies were reviewed to determine building composition [27]. In these studies, the debris from construction and demolition had been analyzed from cities located in Florida and Austria. The average of the construction and debris composition from these buildings was used to predict the total composition of the buildings. Table 6-3 shows the density distribution of construction materials used to create the selected buildings.

Table 6-3: Material composition of the buildings found in the specific cities (kg/m3 gross volume) [28]

	CS1:1970	CS2.1:1890	CS2.2:1960	CS2.3:2003	CS3:1900	CS4:1859
Minerals (bricks, concrete, gravel, sand)	430	420	410	320	260	450
Cement Asbestos	1.5	0.04	-	-	0.14	-
Steel	7.6	5.1	4.6	9.5	5.8	0.97
Aluminum	0.22	0.049	0.057	0.22	0.03	0.16
Copper	0.11	0.15	0.16	0.24	0.0019	0.062
Wood	2.3	4.3	2.2	0.62	3.6	20
PVC	0.52	0.19	0.21	0.18	0.0093	0.2
Various Plastics	1.3	0.16	0.35	4.9	0.14	0.46
Others (e.g. Mineral Wool, Bitumen, Linoleum	1.1	0.54	1.2	0.54	0.43	0.13
Total	440	430	420	340	270	470

By taking the average size of the buildings and multiplying it to the density distribution, this gives the mass of construction materials used in the selected buildings. Table 6-4 shows the material mass breakdown of these buildings that were selected.

Table 6-4: The material mass breakdown of these buildings *[27]*

	CS1	CS2.1	CS2.2	CS2.3	CS3	CS4
Building Use	Residential	Administration Hospital	Hospital	Hospital	Industrial Production	Commercial Residential
Construction Material	Reinforced Concrete	Brickwork	Reinforced Concrete, Brickwork	Reinforced Concrete	Steel, Brickwork	Brickwork
Gross Volume (m3)	6.00E+04	6.20E+04	7.20E+03	1.10E+04	2.10E+04	3.70E+04
Composition of (kg)						
Bricks, concrete, aggregate	2.58E+07	2.60E+07	2.95E+06	3.52E+06	5.46E+06	1.67E+07
Cement Asbestos	9.00E+04	2.48E+03	0.00E+00	0.00E+00	2.94E+03	0.00E+00
Steel	4.56E+05	3.16E+05	3.31E+04	1.05E+05	1.22E+05	3.59E+04
Aluminum	1.32E+04	3.04E+03	4.10E+02	2.42E+03	6.30E+02	5.92E+03
Copper	6.60E+03	9.30E+03	1.15E+03	2.64E+03	3.99E+01	2.29E+03
Wood	1.38E+05	2.67E+05	1.58E+04	6.82E+03	7.56E+04	7.40E+05
PVC	3.12E+04	1.18E+04	1.51E+03	1.98E+03	1.95E+02	7.40E+03
Various Plastics	7.80E+04	9.92E+03	2.52E+03	5.39E+04	2.94E+03	1.70E+04
Others (e.g. Mineral Wool, Bitumen, Linoleum	6.60E+04	3.35E+04	8.64E+03	5.94E+03	9.03E+03	4.81E+03
Total	2.64E+07	2.67E+07	3.02E+06	3.74E+06	5.67E+06	1.74E+07

Then by dividing the mass of each construction material by the total mass of the buildings the weighted average of construction material was determined. These values are shown in Figure 6-1. These values were normalized from 0 to 1 to ensure that all components of the urban matrix would be accounted. Table 6-5 shows the actual numerical values of the building structural materials used in the NUKES library.

Table 6-5: Actual numerical values of the buildings used in the model [27]

	CS1	CS2.1	CS2.2	CS2.3	CS3	CS4
Minerals (bricks, concrete, gravel, sand)	97.215 %	97.172 %	97.617%	94.117 %	96.273 %	95.445 %
Cement Asbestos	0.241%	0.091%	0.100%	0.010%	0.048%	0.010%
Steel	1.629%	1.087%	1.395%	3.684%	2.050%	0.196%
Aluminum	0.050%	0.089%	0.087%	0.055%	0.089%	0.024%
Copper	0.075%	0.065%	0.062%	0.061%	0.099%	0.003%
Wood	0.423%	0.901%	0.424%	0.172%	1.235%	4.246%
PVC	0.018%	0.056%	0.050%	0.043%	0.097%	0.033%
Various Plastics	0.196%	0.063%	0.017%	1.431%	0.048%	0.088%
Others (e.g. Mineral Wool, Bitumen, Linoleum)	0.150%	0.026%	0.186%	0.149%	0.059%	0.018%
Total	100.00 %	99.55%	99.94%	99.72%	100.00 %	100.06 %

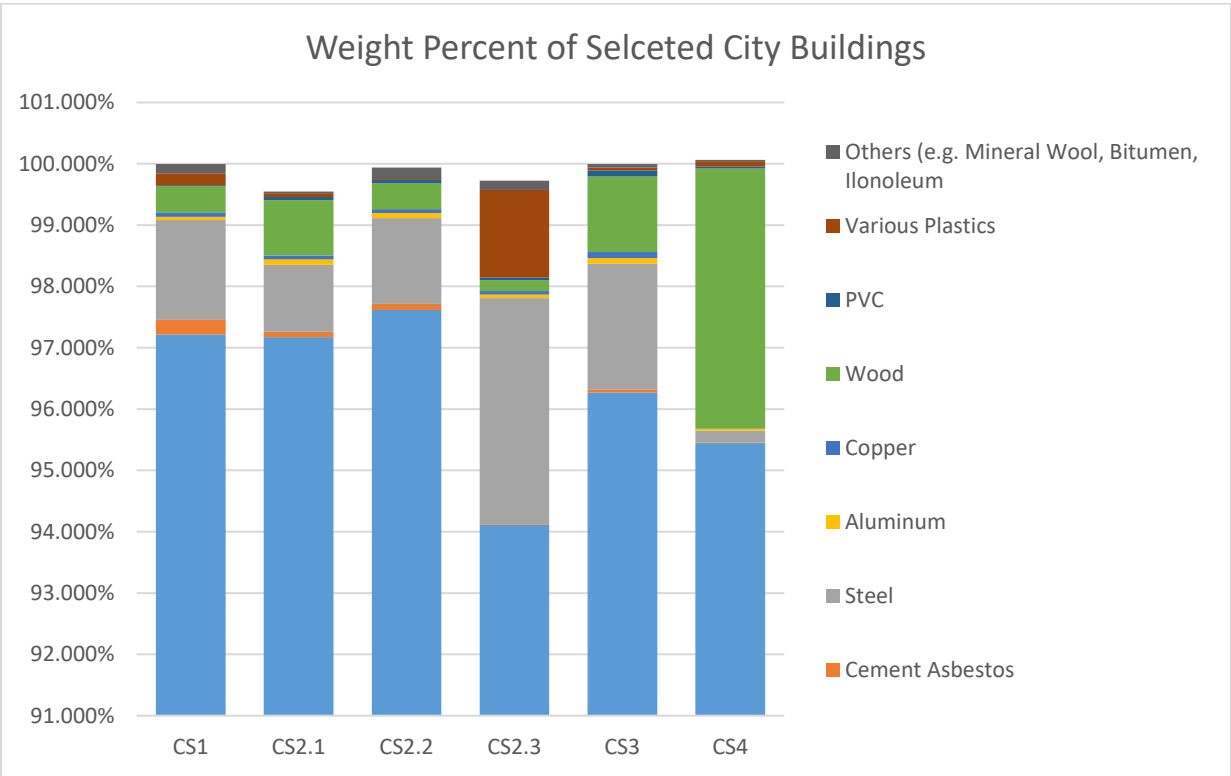

Figure 6-1: Mass ratio of each construction component for the modeled buildings

Adding the Skyscrapers

Due to the addition of skyscrapers to the urban environment, a new type building needed to be added to the building library. These particular buildings contain reinforced concrete and steel construction. The amount of steel utilized in these buildings exceed any values given in the previous tables; therefore, this type of structure had to be added to the library. As shown in Figure 6-2 the ratio of steel to concrete would relatively be equal. [29]

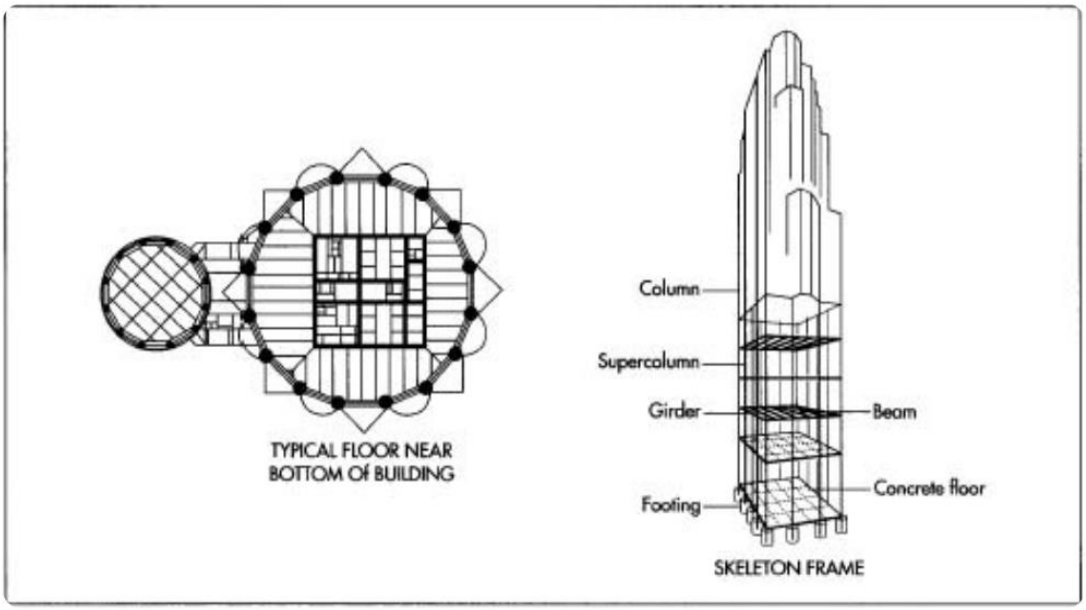

Figure 6-2: Diagram of the skyscraper model used for the buildings portion

Per the MIT Department of Civil and Environmental Engineering most of the stainless steel used in building a skyscraper or other structures, the alloy is a high-strength quenched and tempered (Q&T) alloy. The yield strength of this material is 90-100ksi. The composition of this material is primarily iron; however, it has quantities of chromium and nickel to add ductility and strength.

Adding Cars

Another factor that altered the urban matrix during detonation was the number of cars located around the blast. Giminaro et.al[2]. estimated this value based upon the percent cover of the transportation. However, if the cars are parked in a garage, this evaluation would be incorrect. Therefore, to more accurately capture the average number of automobiles, the number of automobiles was determined based upon the type of building where the cars were parked. For example, the number of cars at a single-residential home, was assigned a value of two cars.

Brick and Reinforced Concrete

Because there is no differentiation from bricks and reinforced concrete, is assumed that they are similar in composition. Therefore, the matrix was not affected based upon the formation. The only difference between brick and reinforced concrete is that the concrete is reinforced with steel structure. Therefore, to account for this difference, an element of steel is added into the building composition library. [30], [31]

Weighting Factor

To complete the building library, the basic construction materials of the buildings were determined from various studies. These construction materials include the following materials: concrete, brickwork, steel, copper, and various materials. After compiling these libraries, the construction materials were broken down into more basic molecules that can be purchased and used in the laboratory. The composition of these construction materials was determined from multiple studies.[32], [33],[34]

Table 6-6: The molecular composition of the selected buildings

	SiO2	Al2O3	CaCo3	Fe2O3	FeO	MgO	H2O	CaO	Na2O	K2O	SO3	Carbon	CrO	NiO	CuZn5
CS2.1	0.310	0.072	0.154	0.034	0.010	0.077	0.000	0.304	0.007	0.015	0.006	0.010	0.002	0.002	0.007
CS1	0.263	0.054	0.136	0.147	0.009	0.067	0.000	0.235	0.006	0.013	0.004	0.007	0.029	0.027	0.001
CS2.2	0.288	0.059	0.146	0.091	0.009	0.072	0.000	0.271	0.007	0.014	0.005	0.005	0.016	0.015	0.001
CS2.3	0.152	0.031	0.077	0.391	0.005	0.038	0.000	0.137	0.003	0.007	0.002	0.020	0.087	0.082	0.001
CS3	0.304	0.063	0.151	0.040	0.010	0.075	0.000	0.298	0.007	0.015	0.006	0.014	0.003	0.003	0.001
CS4	0.304	0.062	0.152	0.039	0.010	0.076	0.000	0.299	0.007	0.015	0.006	0.044	0.003	0.003	0.000

Table 6-7: The elemental composition of the selected buildings

	Fe	Si	Ca	S	C	Na	K	Al	Mg	Cr	Cu	Zn	Ni
CS2.1	0.044	0.311	0.458	0.006	0.010	0.007	0.015	0.072	0.077	0.002	0.006	0.000	0.002
CS1	0.156	0.290	0.372	0.004	0.007	0.006	0.013	0.054	0.067	0.029	0.001	0.000	0.027
CS2.2	0.101	0.302	0.417	0.005	0.005	0.007	0.014	0.059	0.072	0.016	0.001	0.000	0.015
CS2.3	0.396	0.234	0.214	0.002	0.020	0.003	0.007	0.031	0.038	0.087	0.001	0.000	0.082
CS3	0.050	0.307	0.449	0.006	0.014	0.007	0.015	0.063	0.075	0.003	0.001	0.000	0.003
CS4	0.049	0.307	0.450	0.006	0.044	0.007	0.015	0.062	0.076	0.003	0.000	0.000	0.003

Chapter 7: Utilizing Edge Finding Masks to find Urban Building Boundaries

Introduction

In order for accurate urban blast calculations to be made, the composition, location, and dimensions of the buildings were determined. This chapter will discuss multiple edge finding methods which would automate populating a NUKES city model. This chapter discusses and highlights the importance of developing a dependable edge finding algorithm for NUKES that communicates with the data stored on Google Earth. It also discusses the multiple edge finding techniques that were explored to determine which method most accurately fit the original Google Earth image.

Automate Edge Finding Capabilities

It was beneficial to explore edge finding methods that helped determine location and dimensions of buildings surrounding ground zero (GZ). As previously discussed, when an IND is detonated within a city, the fireball quickly vaporizes the surrounding area. Because city infrastructure can be quite complex and detonation yield of specific weapons can affect a sizable radius, it is crucial that the urban environment be quickly modeled in NUKES. Google Earth has complied a large database of building locations and dimensions that can be accessed by most of the public. The public's dependency on apps such as Google Earth, Google Maps, and Location Finding is continually increasing. Therefore, databases that contain building locations and dimensions will continue to develop and grow. It is essential that new fallout codes and NUKES incorporates this easily accessible information. One method of utilizing this information is by using edge finding methods to determine the dimensions and locations of these buildings. However, the challenge of using edge finding methods for modeling purposes is that the methods must match the original images.

Edge Finding Methods and Results

Multiple edge finding methods were studied to determine if this process would be an effective way to populate the NUKES model. Pictures are currently stored on computers by a

certain [m x n] matrix of pixel size. Each pixel of the image corresponds with an RBG color. These RGB colors can be used to help find edges based upon the distribution of color. For example, when looking at the distribution of RGB numbers from an area of an image depicting the top of a flat building, the numerical variation is minor. However, when approaching an edge of the building, the RBG colors will change to either values close to 0 or 255. An algorithm was written to analyze numerical variation based upon different statistical distributions. The best matching statistical distribution depends on the coloring of the image. To accurately compare the different edge finding methods a single image was selected from Google earth and analyzed (Fig.7.1). For this study seven different edge finding methods were used to find the edges of buildings located in Figure 7-1. In order to limit the variation of RGB values and decrease the noise in the images, the Google Earth image was converted into a grayscale format as shown in Figure 7-2 for all edge finding method tests. The grayscale matrix varied from 0 to 255 (or white to black), instead of varying 0 to 255 for three different colors. [35]

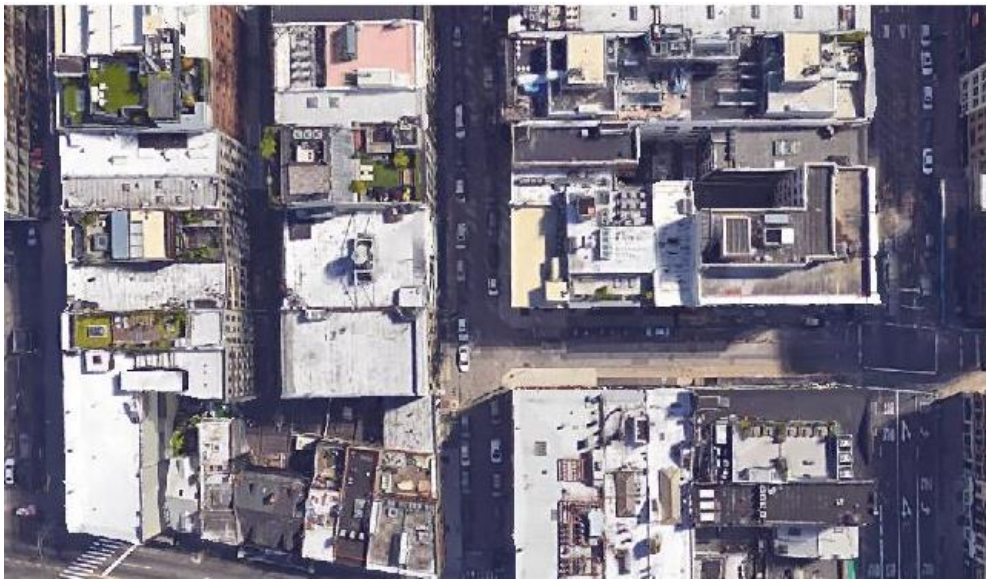

Figure 7-1: Original format of the Google Earth image

Figure 7-2: Grayscale format of the Google Earth image

The Black and White Filter

This Black and White filter method is the most basic method of edge finding. After the image was converted to grayscale, an algorithm was written (Appendix B) to rid the image of the many slight color variations it contains. A small sample of pixels surrounding the color variation were taken and fit to a Poisson distribution. The Poisson distribution was selected because the pixel sample did not exceed more than 25 samples. If the pixels containing and surrounding the color variation was within a standard deviation of the average, the pixels were changed to the average pixel color. However, if the color variation was a large edge, the color change would exceed the standard deviation. Thus, the color of the pixel would not be changed. Once the Poisson filter was applied to the image and the color variations were removed the resulting image was apparent is shown in Figure 7-3.[36]

Figure 7-3: Google Earth image after the Poisson filter was applied

Although this is an improvement from the grayscale image for edge detecting, the areas containing windows and utilities on top of the buildings can still be seen and mistaken for edges of buildings. Another Poisson filter was applied to the image to remove more of the noise. By taking a small sample of pixels in an area, the major color, whether black or white, was determined. The resulting image is shown in Figure 7-4.

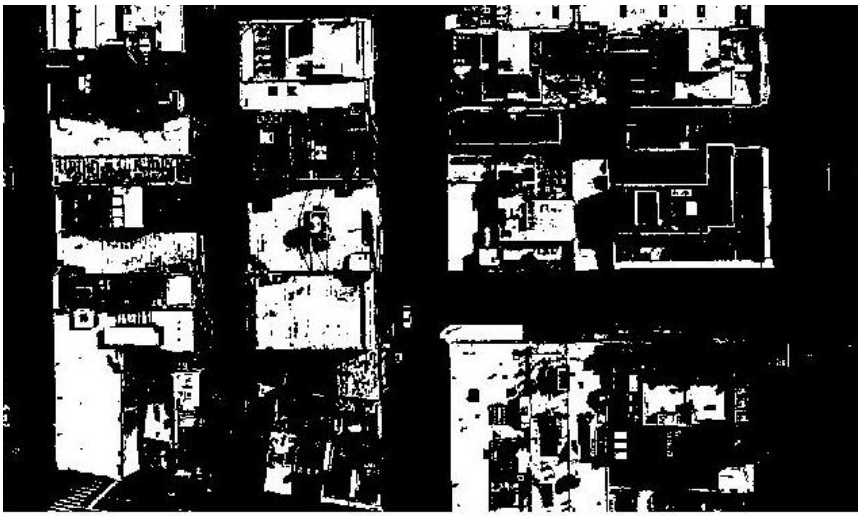

Figure 7-4: Google Earth Image after the Poisson filter was applied to change the image to black and white

The Sobel Method

The Sobel method finds edges using the Sobel approximation to the derivative. This method utilizes two, 3X3 matrix image gradient operators (G_x,G_y). These operators are used in conjunction with a 2-demensional signal processing convolution operator to accurately predict edges in the image. Equation 7.1 and 7.2 shows this operation where A is the pixel matrix of the image, and the 3x3 matrix is the threshold setting for the method. Equation 7.3 and 7.4 shows how the final gradients of the image are calculated. The Sobel method returns edges at those points where the gradient (Θ) of the image is zero. The default threshold is chosen heuristically in a way that depends on the input data. The best way to vary the threshold is to run edge once, capturing the calculated threshold as the second output argument. Then, starting from the value calculated from the edges. [37]

$$G_x = \left(\begin{bmatrix} +1 & 0 & -1 \\ +2 & 0 & -2 \\ +1 & 0 & -1 \end{bmatrix}\right) * (A) \tag{7.1}$$

$$G_y = \left(\begin{bmatrix} +1 & +2 & +1 \\ 0 & 0 & 0 \\ -1 & -2 & -1 \end{bmatrix}\right) * (A) \tag{7.2}$$

$$G = \sqrt{G_x^2 + G_y^2} \tag{7.3}$$

$$\Theta = \operatorname{atan}\left(\frac{G_y}{G_x}\right) \tag{7.4}$$

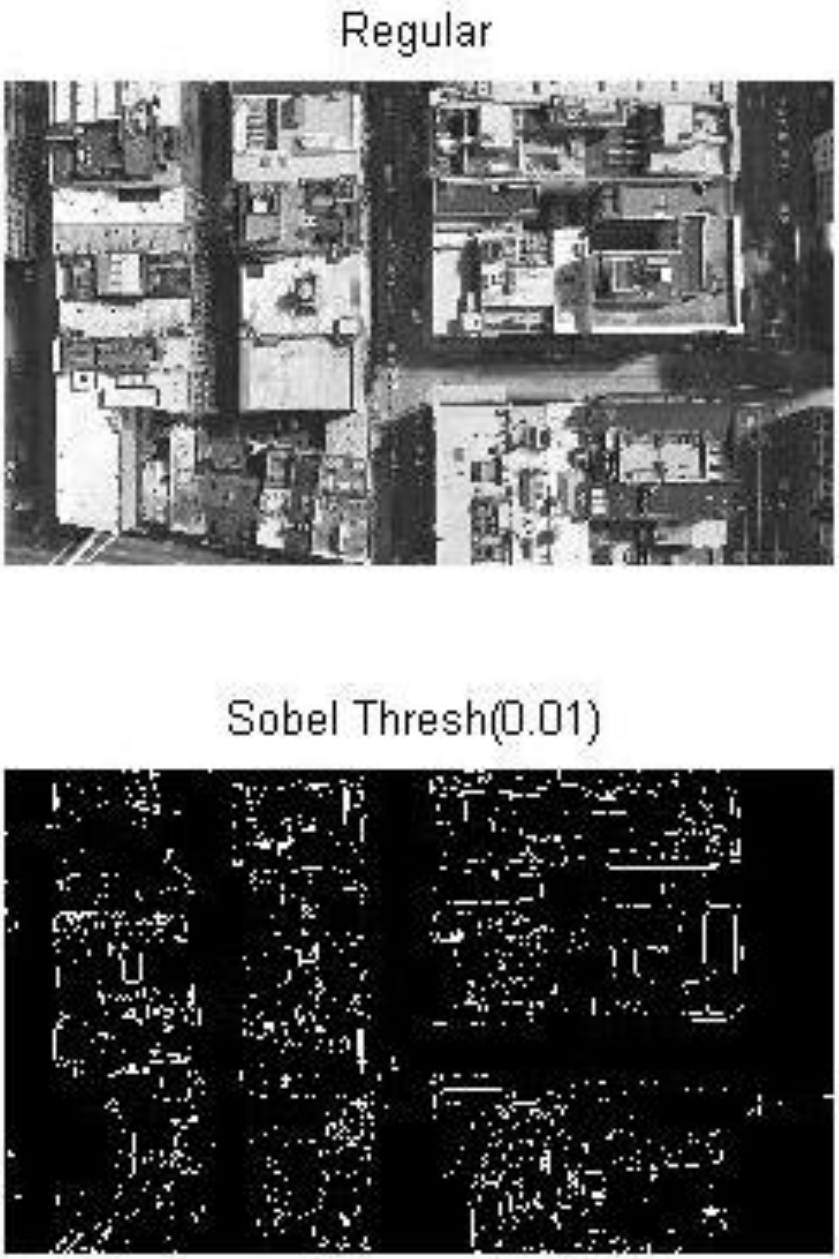

Figure 7-5: Original grayscale image and the Strobel edge finding method

The Prewitt Method

The Prewitt method finds the edges of an image using a discrete differentiation operator. Similarly, to the other edge detection algorithms, this method utilizes a 3x3 kernels to calculate the gradient intensity function of the image. G_x is the horizontal kernel and G_y is the vertical kernel. *A* is the pixel matrix of the selected image. In Eq.7.5 and 7.6 the (*) operator represents a 1-dimensional convolution operation which averages the gradients of *x* and *y* to compute the gradients contained in the image. Eq. 7.7 and 7.8 show the calculation method to determine the gradient (Θ) of the image. It returns edges at those points where the gradient of I is roughly equivalent to 0. The default threshold is chosen heuristically in a way that depends on the input data. The best way to vary the threshold is to run edge finding algorithm once, and then running the same code a second time to capture the calculated threshold as the second output argument. [35]

$$G_x = \left(\begin{bmatrix} +1 & 0 & -1 \\ +1 & 0 & -1 \\ +1 & 0 & -1 \end{bmatrix}\right) * (A) \tag{7.1}$$

$$G_y = \left(\begin{bmatrix} +1 & +1 & +1 \\ 0 & 0 & 0 \\ -1 & -1 & -1 \end{bmatrix}\right) * (A) \tag{7.2}$$

$$G = \sqrt{G_x^2 + G_y^2} \tag{7.3}$$

$$\Theta = \operatorname{atan} 2\left(G_y, G_x\right) \tag{7.4}$$

Regular

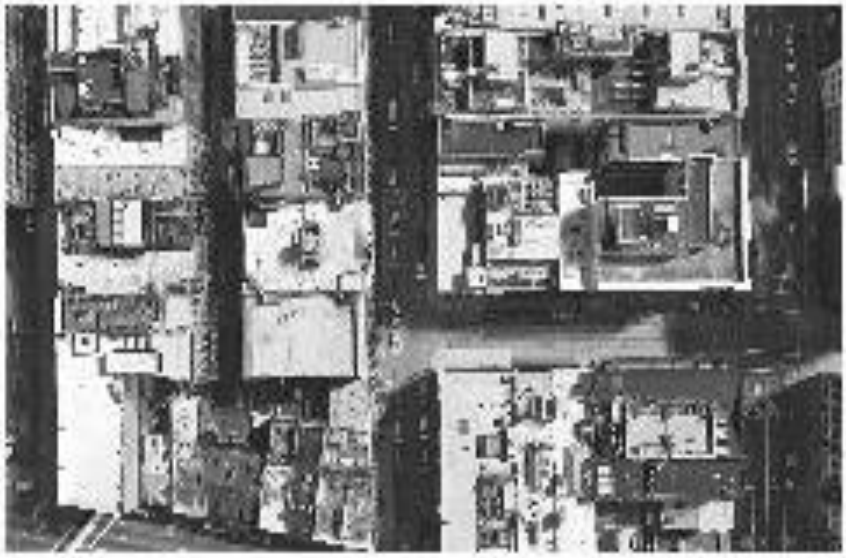

Prewitt

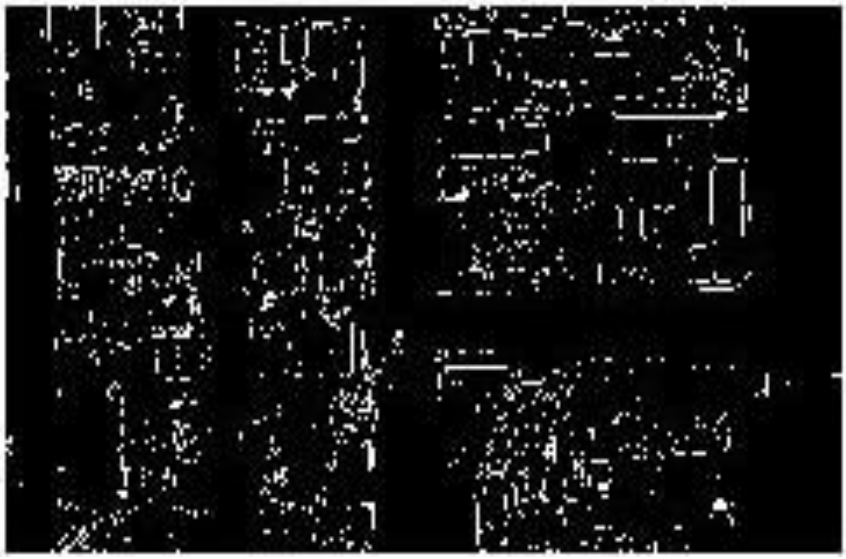

Figure 7-6: Original grayscale image and the Prewitt edge finding method

The Roberts Method

The Roberts method was one of the original edge finding methods used. It used a discrete differential operator that would approximate the gradient of the image. Different from the Sobel or Prewitt method, the Roberts method utilizes two, 2x2 kernels for vertical and horizontal analysis (Eq 7.9 and 7.10). Eq. 7.11 and 7.12 shows the calculation method to determine the gradient (Θ) of the image after the kernels are applied to the image. It returns edges at the points where the gradient of I is near 0. The default threshold is chosen heuristically in a way that depends on the input data. The best way to vary the threshold is to run edge finding algorithm once, and then running the same code a second time to capture the calculated threshold as the second output argument. [38]

$$G_x = \begin{bmatrix} +1 & 0 \\ 0 & -1 \end{bmatrix} * A \tag{7.1}$$

$$G_x = \begin{bmatrix} 0 & +1 \\ -1 & 0 \end{bmatrix} * A \tag{7.2}$$

$$\Delta I(x, y) = G(x, y) = \sqrt{G_x^2 + G_y^2} \tag{7.3}$$

$$\Theta(\mathrm{x}, \mathrm{y}) = \mathrm{atan}\left(\frac{G_y}{G_x}\right) - \frac{3\pi}{4} \tag{7.4}$$

Regular

Roberts

Figure 7-7: Original grayscale image and the Roberts edge finding method

The Laplacian of Gaussian Method

The Laplacian of Gaussian method finds edges by looking for zero crossings after filtering I with a Laplacian of Gaussian Filter.

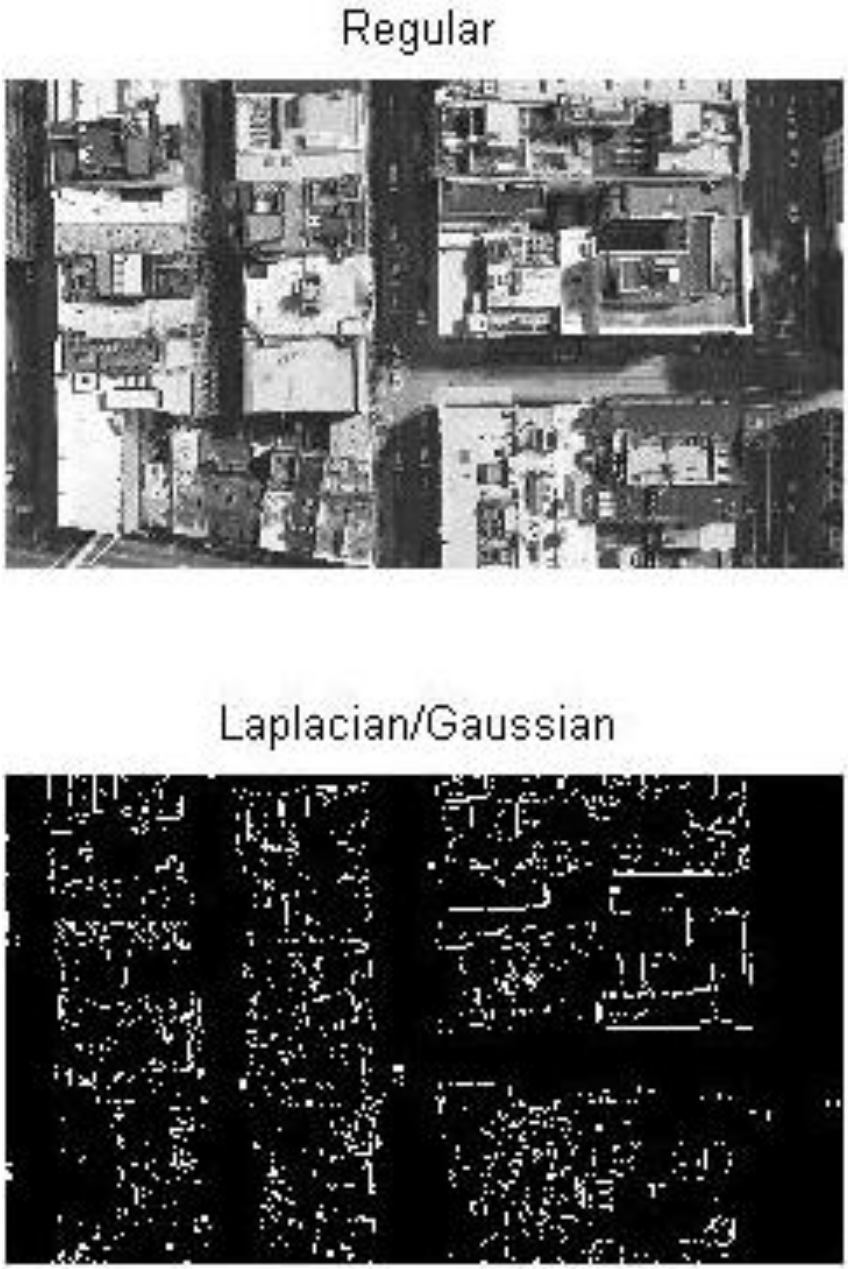

Figure 7-8: Original grayscale image and the Laplacian/Gaussian edge finding method

The Canny Method

The Canny method finds edges by looking for local maxima of the gradient of I. The gradient is calculated using the derivative of a Gaussian filter. The method uses 2 thresholds to detect strong and weak edges, and included the weak edges in the output only if they are connected to the strong edges. This method is, therefore, is less likely than the other methods to be fooled by slight fluctuations in the image. It is more likely to find less pronounced edges.

The Canny method applies 2 thresholds to the gradient: a high threshold for the low edge sensitivity and a low threshold for high edge sensitivity. Edge starts with the low sensitivity result and then grows it to include connected edge pixels from the high sensitivity result. This helped to fill in gaps in the detected edges. [38]

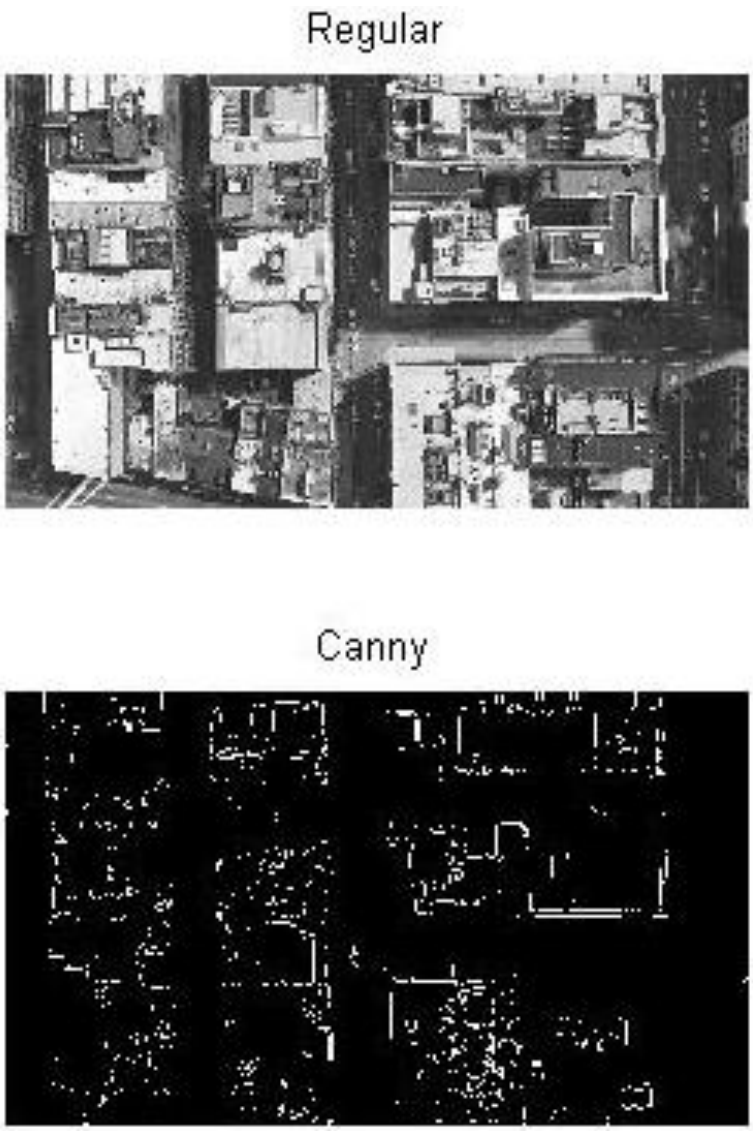

Figure 7-9: Original grayscale image and the Canny edge finding method

Chapter Summary

After an in-depth look at the different methods used for edge detection, each method can be optimized for a given image. Depending upon pixel size, coloration, and threshold settings, each method can accurately be used to find edges in very specific images. Since NUKES must be a versatile code for the lower 48 continental states, the large variation of urban environment design and color would render the edge finding methods insignificant. These methods depend upon a calibrated threshold setting to accurately determine edges. The user

would have to manually adjust the threshold each time a new GZ coordinate was entered in NUKES.

Even after proper threshold calibration, the user would have to manually scale the image where the detonation occurs. Depending upon yield size and fireball growth, the size of the image would drastically vary upon pixel dimensions. Therefore, the threshold of edge fitting algorithm would have to be changed depending upon the pixel size of the picture.

Assuming that the edge fitting method would provide accurate building dimensions and location, it would not provide height or internal composition data. By using an edge fitting filter, the image would have to be in a 2-D area. It is not possible to collect 3-D data from the imaging used in Google Earth. However, software updates and database changes might make this data available to users in the future, but currently it is not possible to collect 3-D data from Google Earth.

Finally, the edge fitting filters would not provide the user with the structural data needed to predict the composition of each building. The user would still have to manually enter the composition of the building effected by the nuclear blast. It can be concluded that this method of edge fitting is not a feasible method for NUKES to determine urban layout and composition.

Chapter 8: Results

Chapter Overview

In this chapter the output of the NUKES code is discussed. The first portion of the chapter will focus on the change in soil composition based upon the location of the burst, and the change in the crater dimensions based upon the type of soil where detonation occurs. The second portion of the code focuses on the results from detonating a surface burst in Annapolis, MD near the Naval Academy. The third portion of the chapter discusses the method used to validate the NUKES code. Currently the only easily attainable data for a near surface burst that includes some urban structures is the Trinity test. Therefore, a comparison between the composition of trinitite to the predicted composition output of NUKES will be made to help validate the code.

Soil Variation

As discussed in the previous chapter, NUKES references multiple soil libraries to predict the soil composition of a specific area. The weighting factor was applied to data points depending upon distance from burst. Points that are closest to the burst add more to the soil matrix than more distant points. The user can specify the radius surrounding the burst in which the data was collected. The smaller the radius, the better the simulation will be. It then uses the crater dimensions to help calculate the weighted averages from the multiple soil libraries. Figure 8-1 shows the structure composition of the soil; this is crucial because as melt glass manufacturing processes improve, the ability to melt actual rock might change the structure and formation of the rock. Therefore, a print out of the soil structure is included.

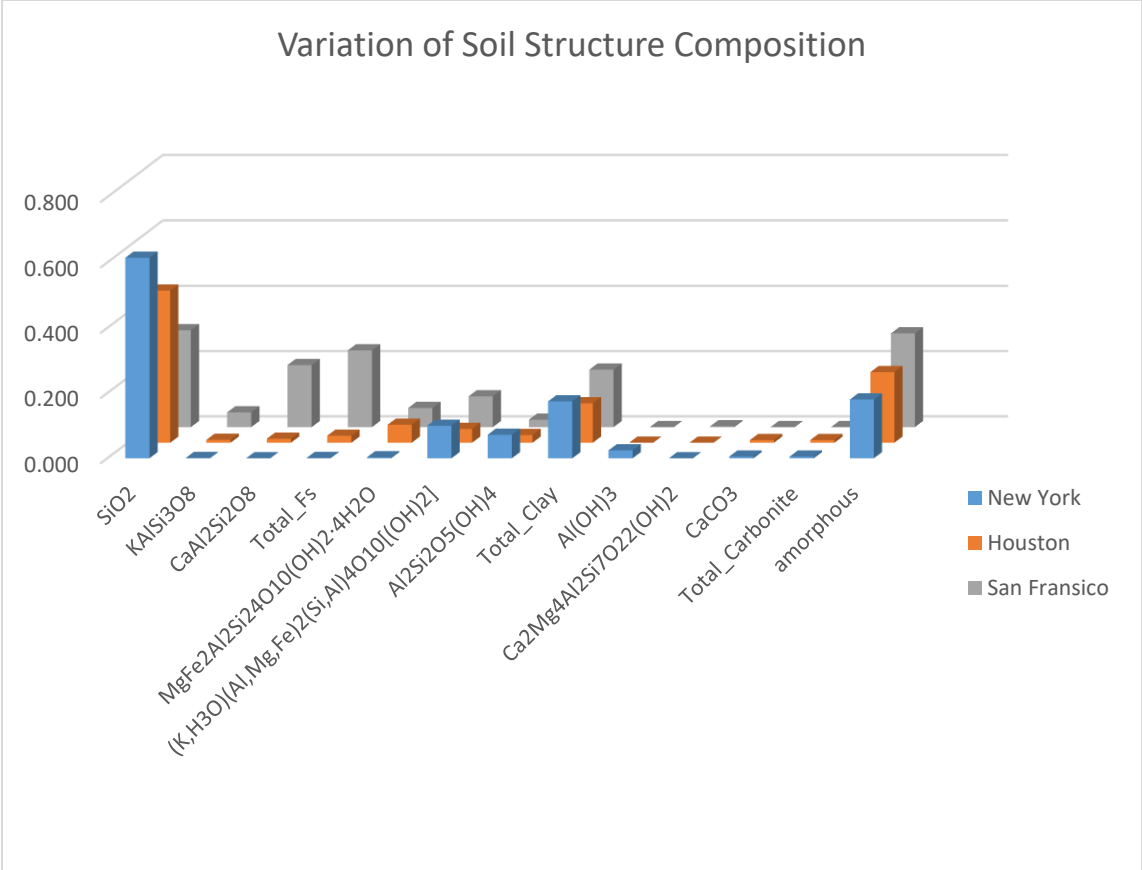

Figure 8-1: Soil structure composition from the soil and the chemical molecules are actual rock stratus that can be found

Soil composition data from Los Angeles, CA and Knoxville, TN was computed by the NUKES program. The differences between these soils are plotted below. Figure 8-2 and Figure 8-3 show the molecular variation within soil debris depending upon the location. Figure 8-4 and Figure 8-5 show the elemental variation of soil composition depending upon burst position in the US. NUKES is programmed to automatically normalize the value of the matrix to 100% in the case that the total soil composition falls under 100%. Additionally, if the sum of the soil composition falls below 98%, NUKES gives an error to inform the user that all soil composition was not accounted for.

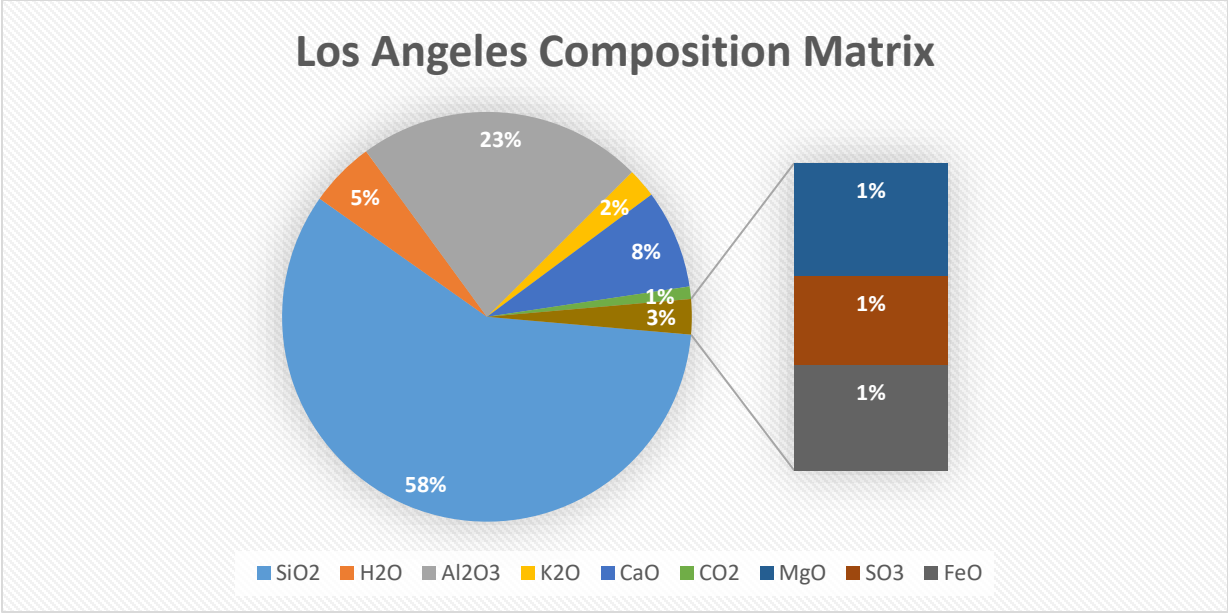

Figure 8-2: Soil molecular composition. This is the molecules that can be added from the laboratory facilities

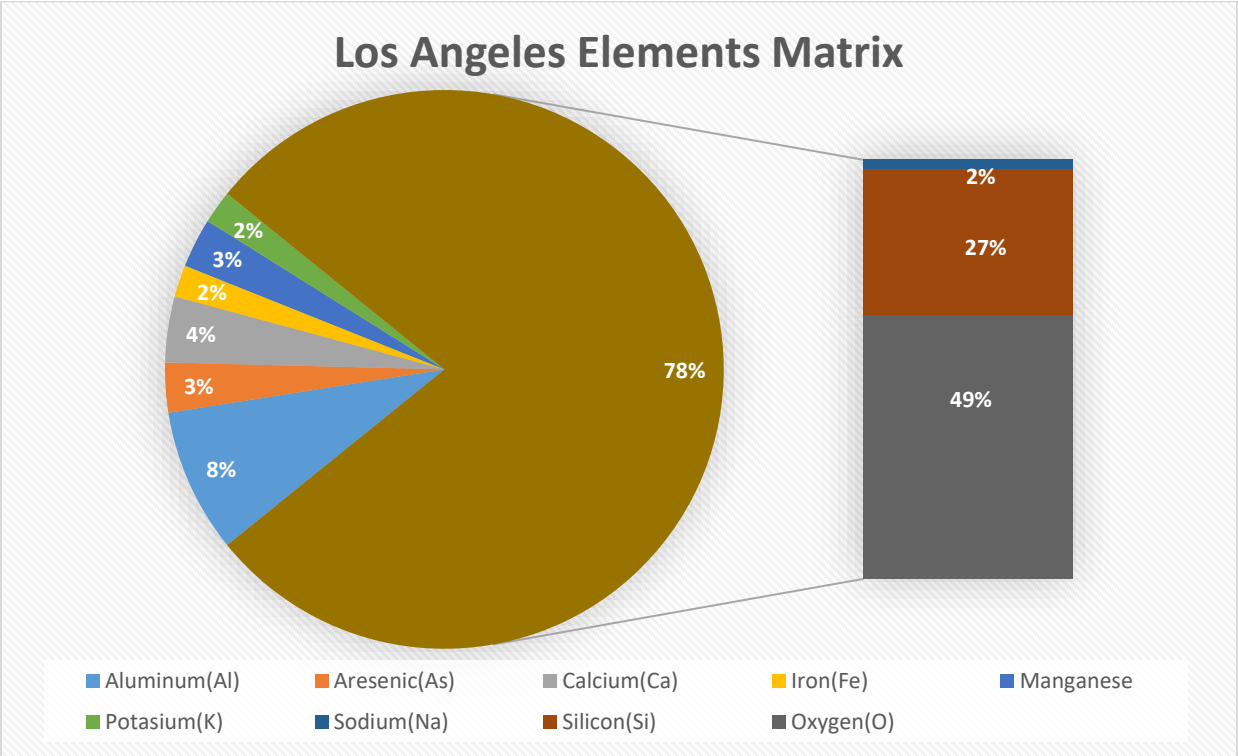

Figure 8-3: The elemental composition of the soil in Los Angeles, CA

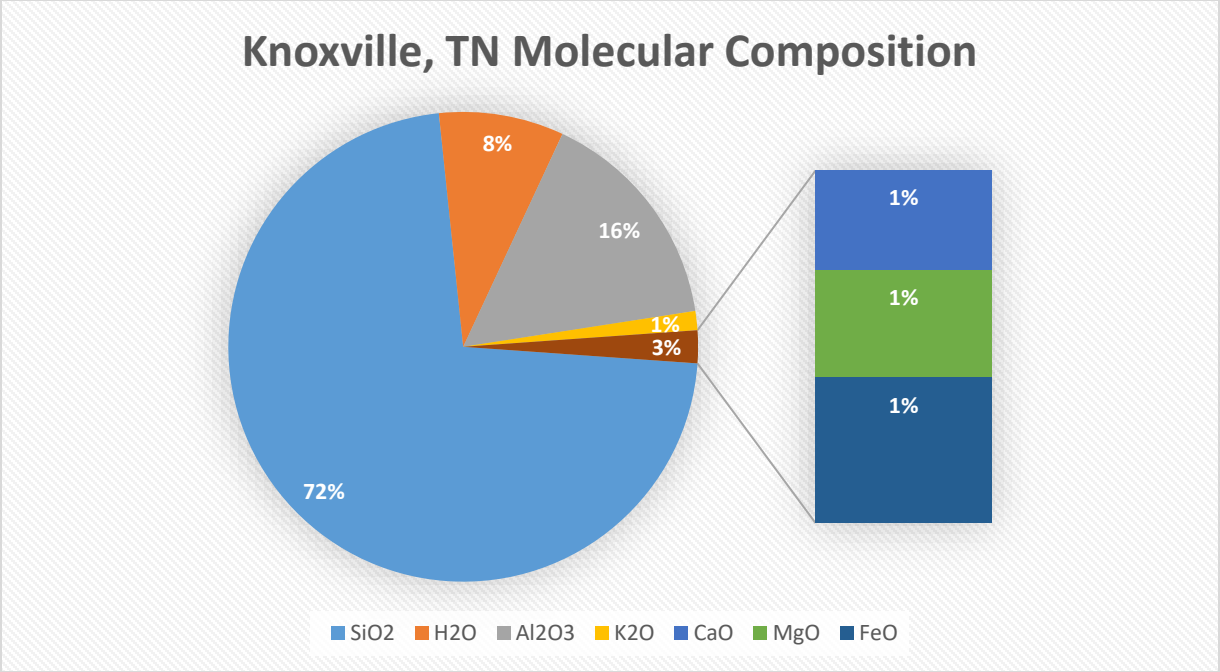

Figure 8-4: The molecular composition of the soil in Knoxville, TN

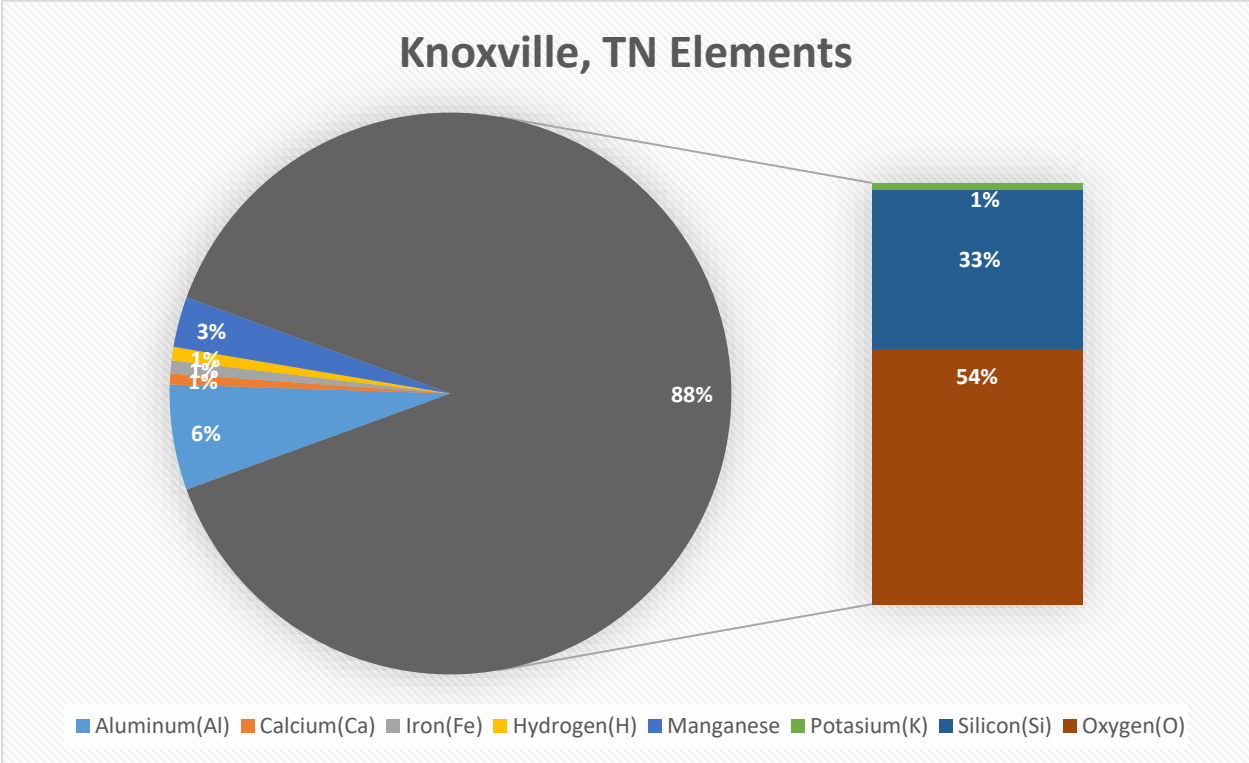

Figure 8-5: The elemental composition of the soil in Knoxville, TN

Crater Size Variation

Shown below are the three-dimensional models of the craters formed from a 20kt burst. The dimensions change based upon the type of soil where the weapons were detonated. NUKES also factors in the concentration of water in the soil. The water contained in the soil allowed better energy and heat transfer. This increases the amount of heat transferred to the soil, and this created a larger crater. Figure 8-6 shows the 3-dimensional crater that is generated from a 20KT surface burst in dry soil. Figure 8-7 shows the 3-dimenasional crater that is generated from a 20KT surface burst in in wet soil. Figure 8-8 shows the 3-dimensional crater that is generated from a 20KT surface burst in dry hard rock. Figure 8-9 shows the 3-dimensional crater that is generated from a 20KT surface burst in wet hard rock.

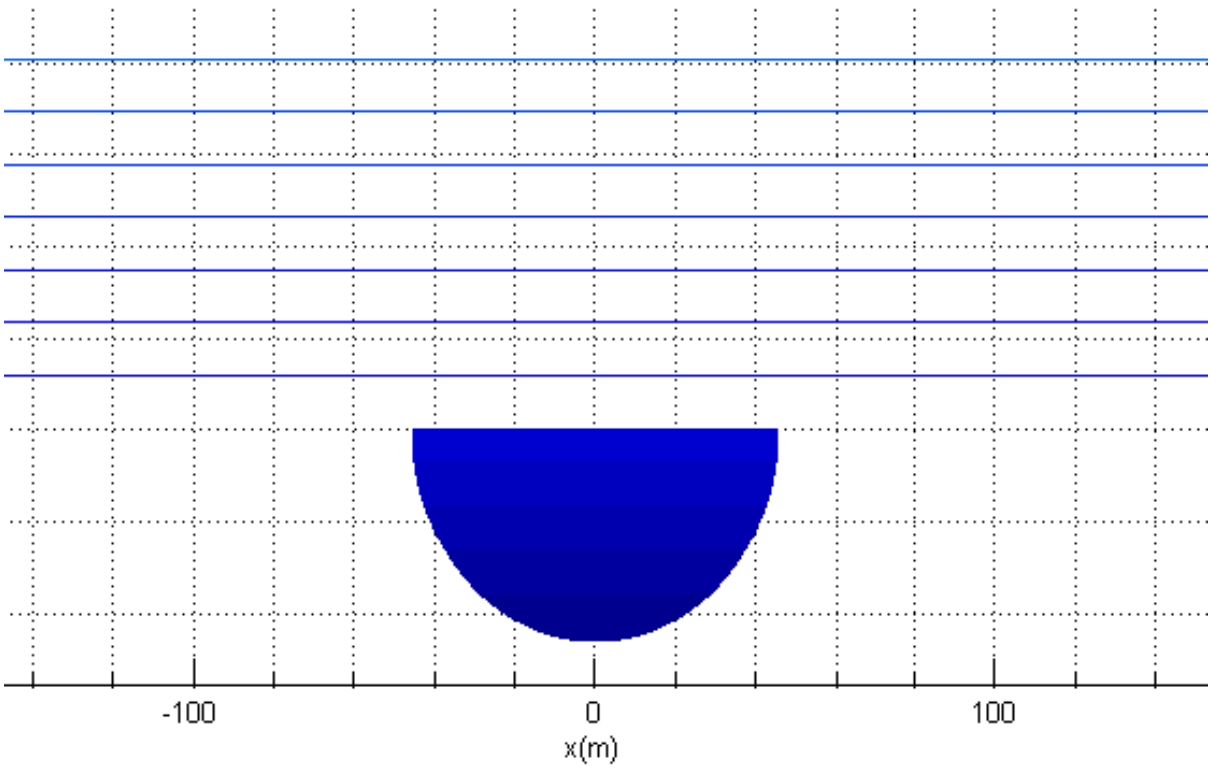

Figure 8-6: Crater Dimensions of a 20kt blast in dry soil (Dry Soft Rock)

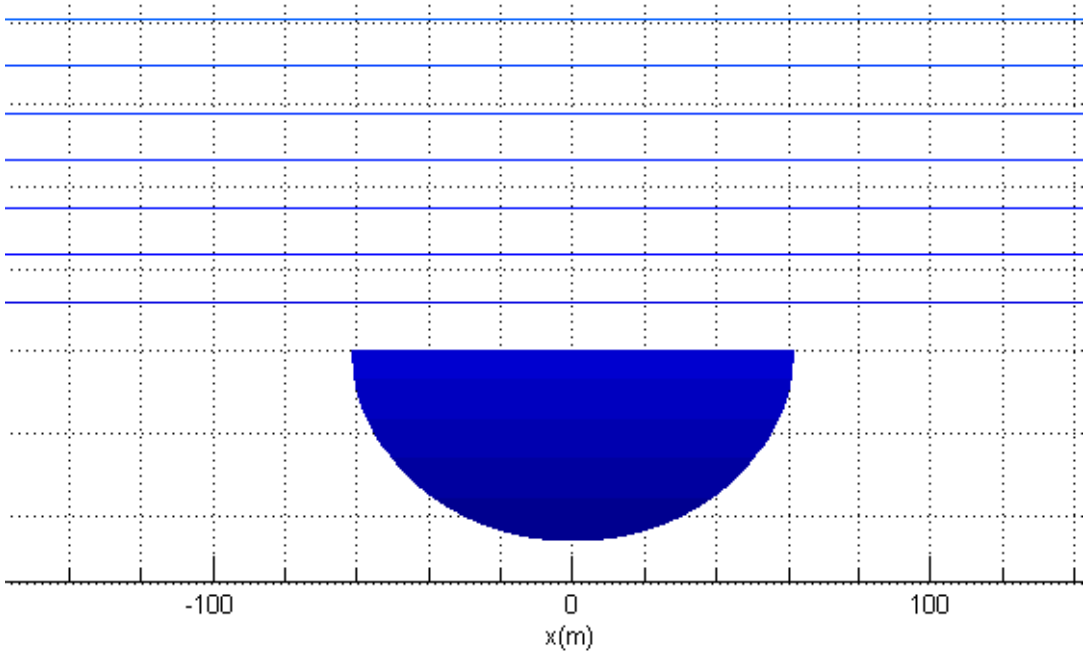

Figure 8-7: Crater Dimensions of a 20kt blast in wet soil (Wet Soft Rock)

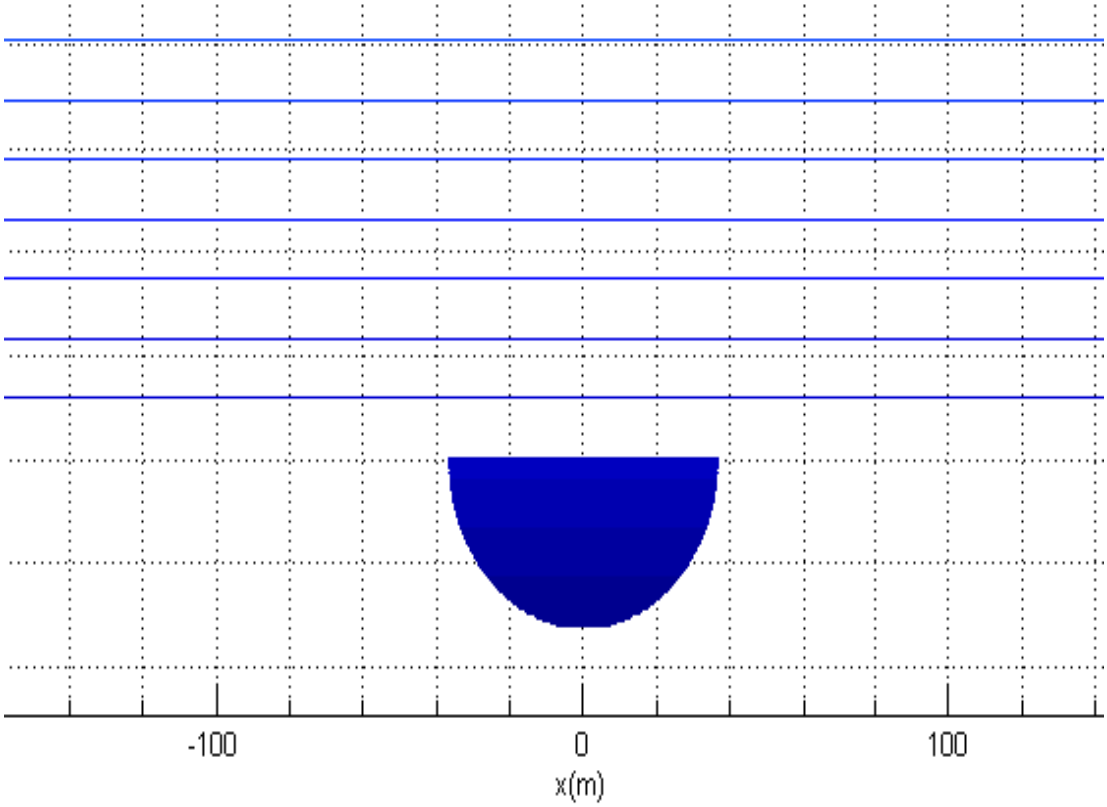

Figure 8-8: Crater Dimensions of a 20kt blast in dry hard rock

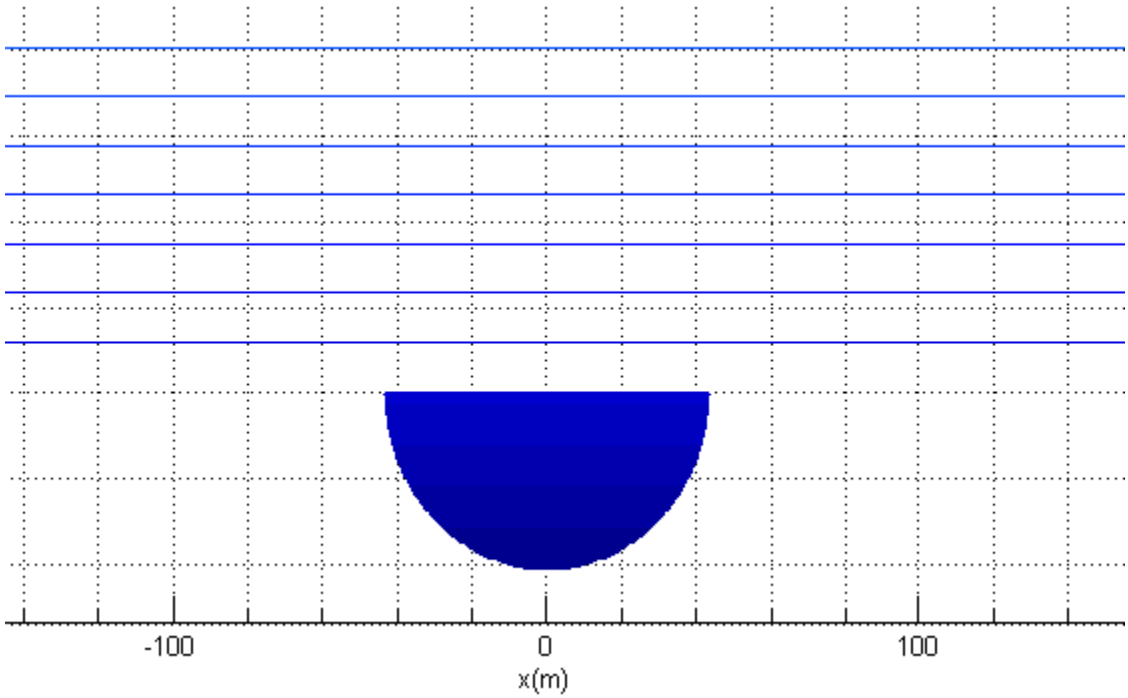

Figure 8-9: Dimensions of a 20KT weapon detonated in wet hard rock

Table 8-1 shows how the density and soil type affects the size of the formed crater. By understanding crater growth in various types of soil, the final melt glass composition can be accurately predicted. The crater dimensions and density of the soil is multiplied together to understand the mass of the soil that is mixed in with the vaporized urban environment. This will have improved the energy calculations performed by NUKES when applied to the urban environment.

Table 8-1: The change in crater dimensions as a function of soil type. The crater volume calculation utilizes the varying soil densities to predict the volume of vaporized soil

Wet Soil (20kt)				
Crater Radius(m)	**Crater Depth(m)**	**Crater Volume(m^3)**	**Soil Mass(kg)**	**Uninhibited Fireball Break Away Radius (m)**
61.40	23.21	34357.47	55035512.36	146.49
Dry Soil(20kt)				
Crater Radius(m)	**Crater Depth(m)**	**Crater Volume(m^3)**	**Soil Mass(kg)**	**Uninhibited Fireball Break Away Radius (m)**
45.67	23.21	76052.44	102536174.77	146.49
Wet Hard Soil(20kt)				
Crater Radius(m)	**Crater Depth(m)**	**Crater Volume(m^3)**	**Soil Mass(kg)**	**Uninhibited Fireball Break Away Radius (m)**
43.43	20.96	15525.51	37304222.19	146.49
Dry Hard Rock (20kt)				
Crater Radius(m)	**Crater Depth(m)**	**Crater Volume(m^3)**	**Soil Mass(kg)**	**Uninhibited Fireball Break Away Radius (m)**
36.69	16.47	8706.56	27893120.07	146.49

Annapolis Structure

After the soil and building libraries were compiled for NUKES the code was ready to be used to predict urban debris composition. As requested an urban environment was created that closely matched the Naval Academy located within Annapolis, MD. A 20KT surface bust was modeled right outside of the Naval Academy. Figure 8-10 shows the 3-dimensional simulation of this urban environment.

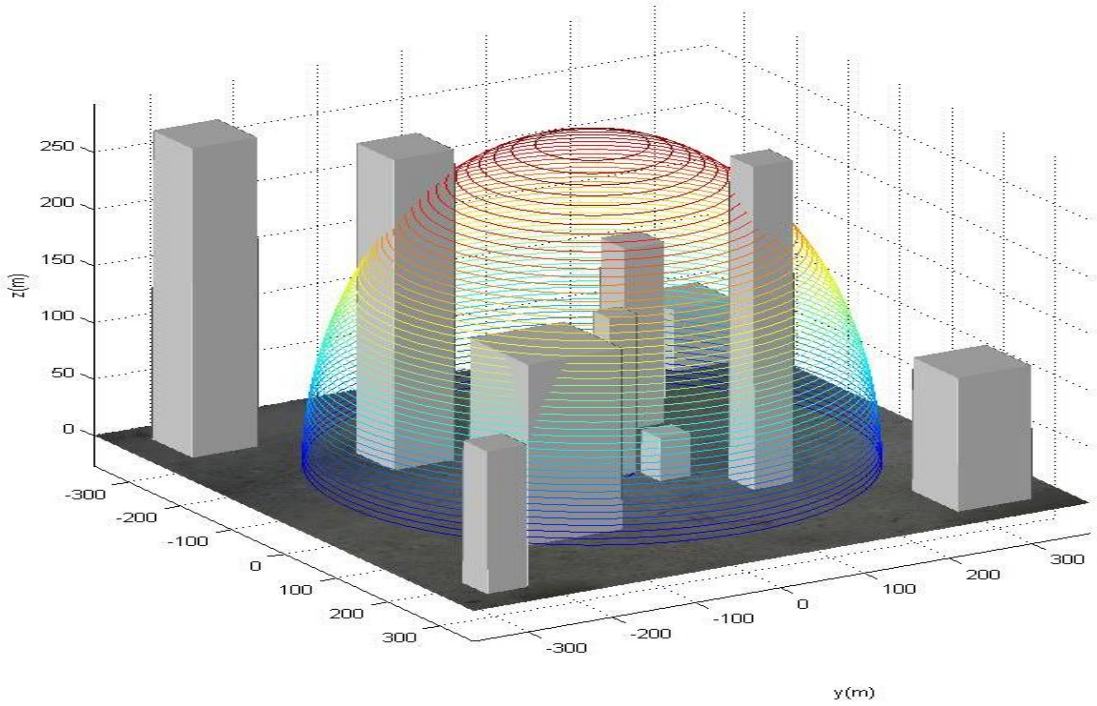

Figure 8-10: A simulated urban environment in which a 20KT fissile WMD was detonated

As the fireball progressed from GZ, the buildings that received enough photon flux to vaporize were factored into the final debris matrix. Figure 8-11 shows the elemental soil composition before the urban debris was accounted for in the matrix, and Figure 8-12 shows the elemental debris composition including both soil and urban environment. Figure 8-13 shows the molecular soil composition before the urban debris was accounted for in the matrix, and Figure 8-14 shows the molecular debris composition including both soil and urban environment. As the mass weighting factors were applied to the debris, it is interesting to watch the change in elements included in the matrix.

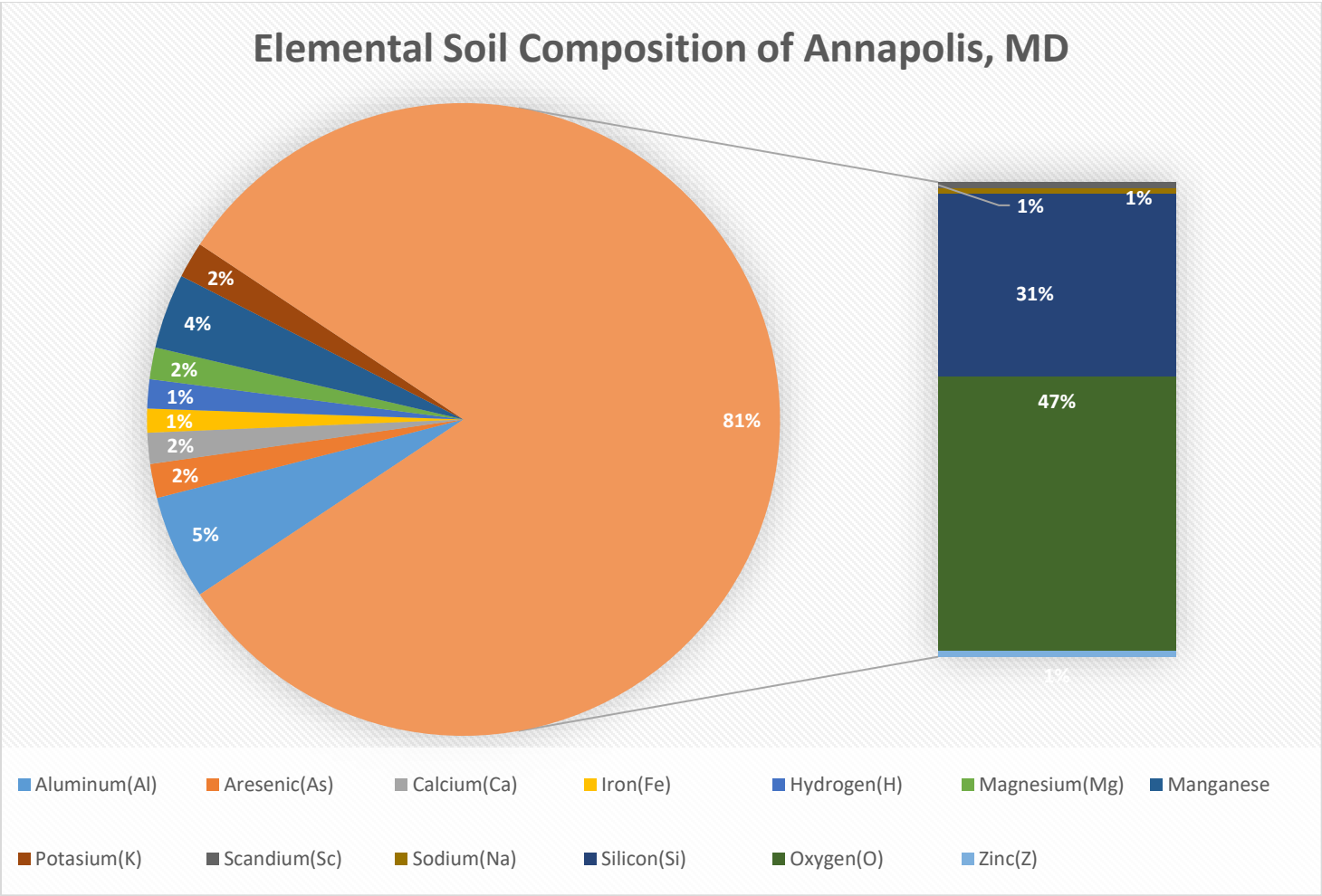

Figure 8-11: The elemental soil composition from Annapolis, MD

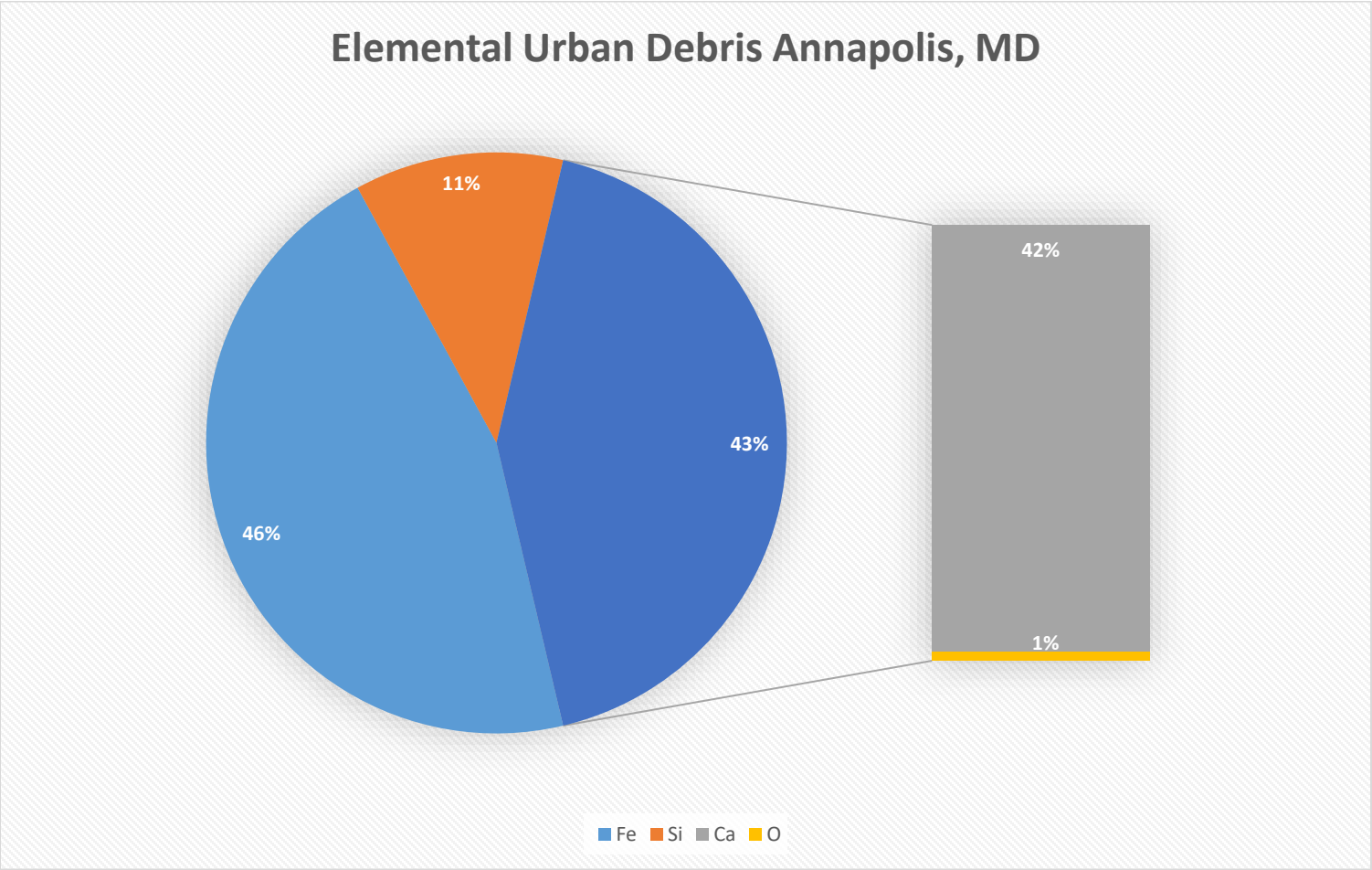

Figure 8-12: The elemental urban debris composition for Annapolis, MD

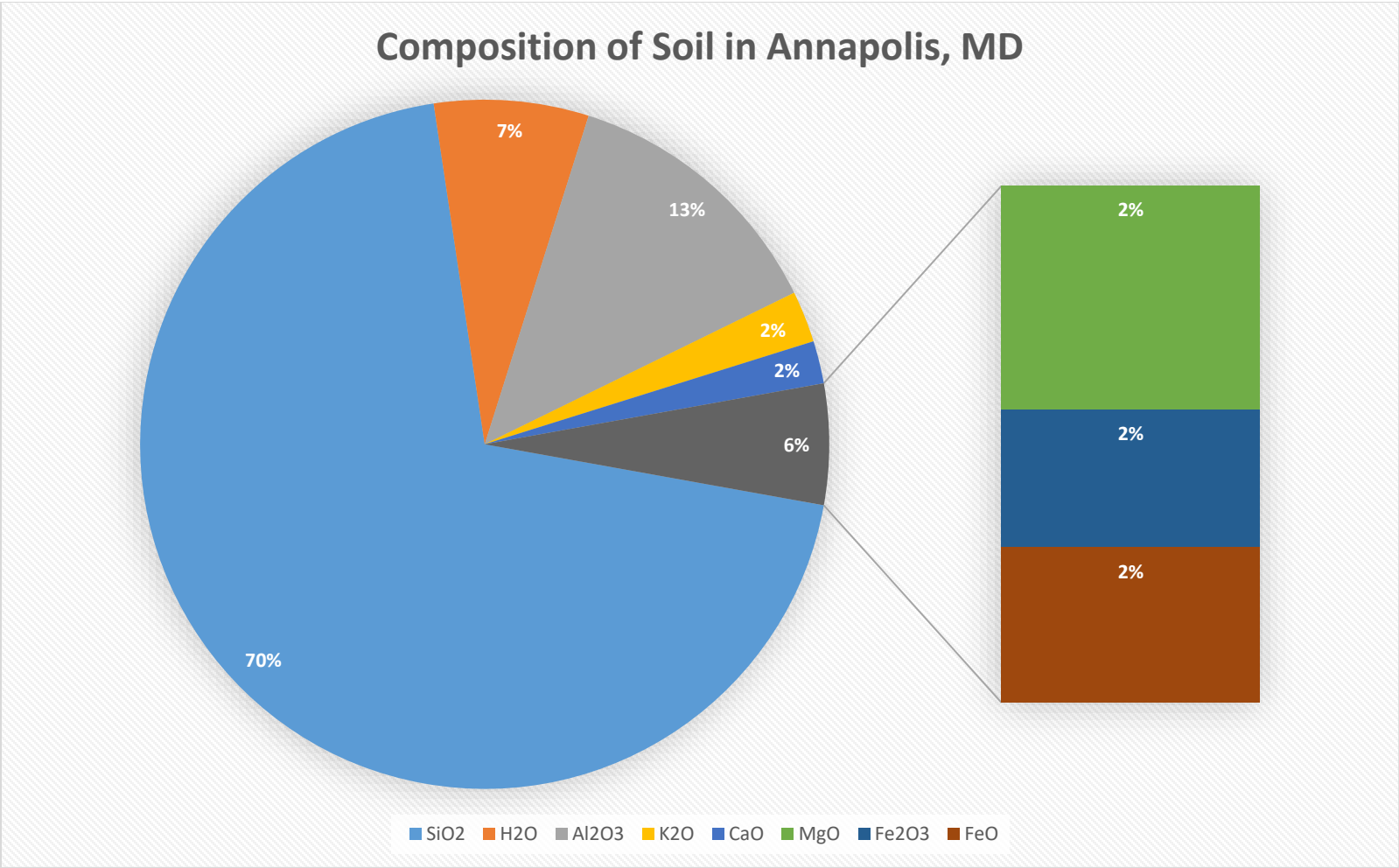

Figure 8-13: The molecular composition of the soil in Annapolis, MD

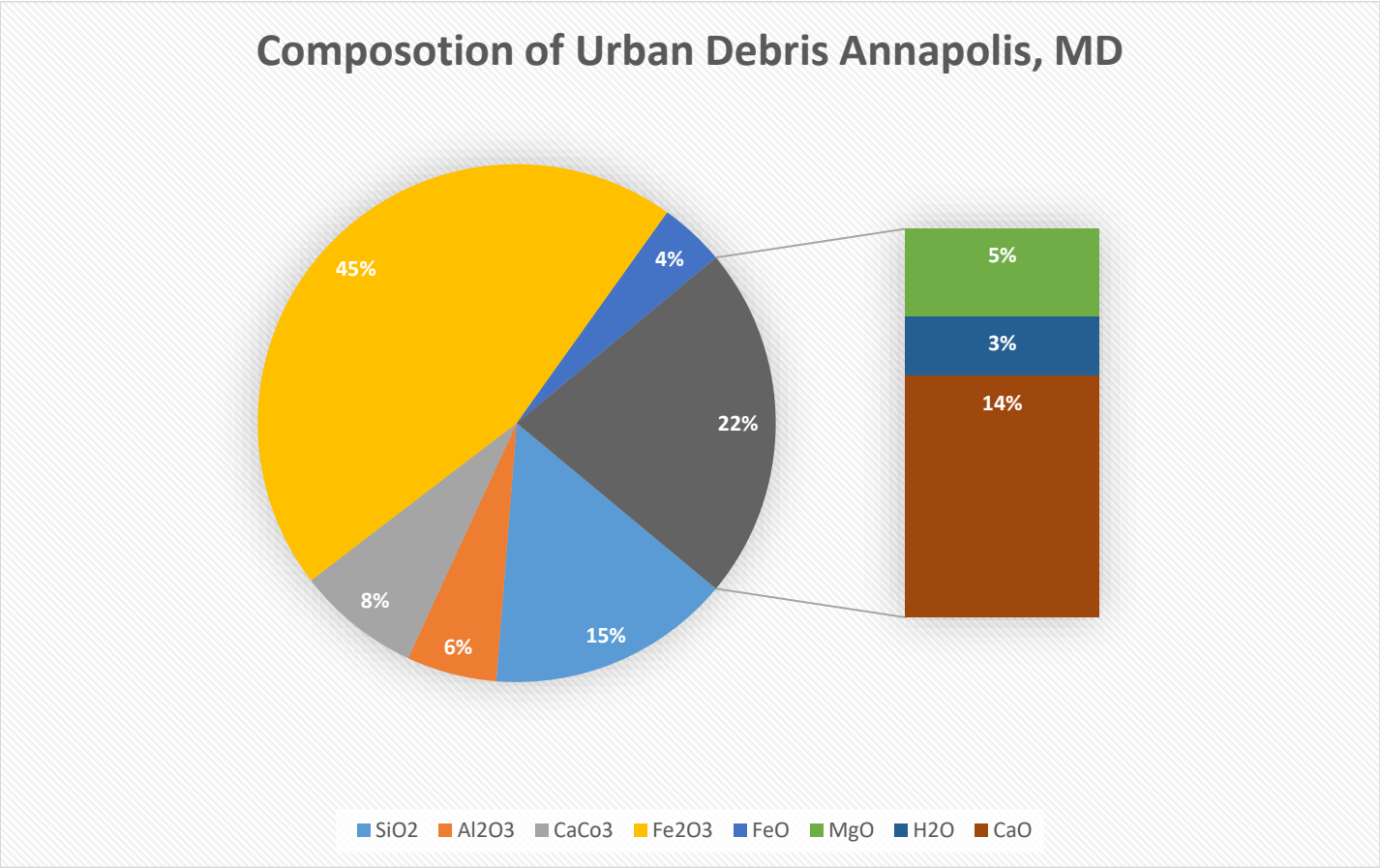

Figure 8-14: The molecular composition of the urban matrix from Annapolis, MD

Trinitite Comparison and Validation

In order to validate the NUKES soil libraries in conjunction with the newly added urban matrix blast calculations, a method was used to compare the simulated surface burst debris predicted by NUKES to actual debris from the NTS. Therefore, the NUKES output from a surface blast was compared to the debris composition from the Trinity test of July 16, 1945.

The Trinity test was the first nuclear weapons test that was conducted in Alamogordo, NM, on July 16, 1945. The “gadget”, as it was referred to, was loaded onto a 30m tower and was detonated. As the 20KT fireball engulfed the surrounding area, affected soil was vaporized and pulled into the mushroom cloud. As the temperatures decreased the vaporized soil cooled, condensing into large particulates of glass (Figure 8-15).

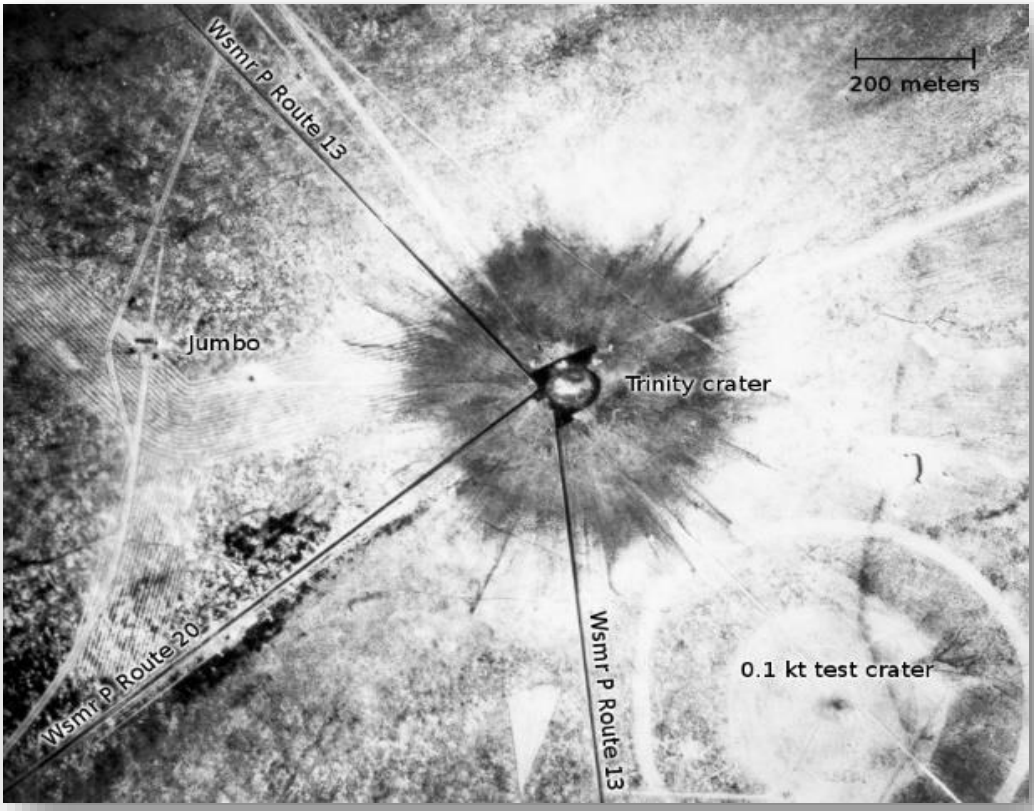

Figure 8-15: The Trinity crater, where the darker area surrounding the crater is the trinitite glass

The glass was collected and analyzed in multiple laboratories and Table 8-2 shows the lab analysis of the actual composition trinitite. These glass samples were compared to the soil debris receipt that NUKES outputs. (Table 8-3). Both compound and elemental composition was conducted to understand the percent variation.

Table 8-2: The composition difference between actual Trinitite and the debris output from NUKES

Compound	Trinitite	Synthetic	NUKES Prediction	Varying Percent (Trinitite vs. NUKES)	Varying Percent (Synthetic vs. NUKES)
SiO2	64.200	64.200	65.831	1.631%	1.631%
Al2O3	14.300	14.300	16.833	2.533%	2.533%
CaO	9.640	9.640	9.830	0.190%	0.190%
K2O	5.130	0.000	4.276	0.854%	4.276%
FeO	1.970	1.970	2.010	0.040%	0.040%
Na2O	1.250	1.250	1.649	0.399%	0.399%
MgO	1.150	1.150	1.304	0.154%	0.154%
MnO	0.505	0.505	0.000	0.505%	0.505%
TiO2	0.427	0.427	0.000	0.427%	0.427%
KOH	0.000	6.120	0.000	0.000%	6.120%
UNH	0.000	0.000	0.000	0.000%	0.000%
O2	0.000	0.000	0.000	0.000%	0.000%
H2O	0.000	0.000	0.000	0.000%	0.000%
CO2	0.000	0.000	0.000	0.000%	0.000%

Table 8-3: The elemental differences between actual trinitite and NUKES' debris output prediction

Compound	Trinitite	Synthetic	NUKES Prediction	Varying Percent (Actual vs. NUKES)	Varying Percent (Synthetic vs. NUKES)
O	46.000%	46.900%	50.079%	4.079%	3.179%
Si	30.000%	30.000%	29.480%	0.520%	0.520%
Al	7.550%	7.550%	7.360%	0.190%	0.190%
Ca	6.880%	6.880%	4.530%	2.350%	2.350%
K	4.260%	4.260%	4.270%	0.010%	0.010%
Fe	1.530%	1.530%	1.750%	0.220%	0.220%
Na	0.924%	0.924%	0.887%	0.037%	0.037%
Mg	0.690%	0.690%	0.780%	0.090%	0.090%
Ti	0.258%	0.258%	0.000%	0.258%	0.258%
Mn	0.039%	0.039%	0.100%	0.061%	0.061%
U	0.002%	0.000%	0.000%	0.002%	0.000%
U	0.002%	0.002%	0.000%	0.002%	0.002%
H	0.000%	0.110%	0.408%	0.408%	0.298%
N	0.000%	0.000%	0.000%	0.000%	0.000%
C	0.000%	0.000%	0.000%	0.000%	0.000%
As	0.000%	0.000%	0.000%	0.000%	0.000%

Table 8-3 shows how the soil debris receipt changes based upon the depth of the crater.

NUKES had to be modified to conduct this experiment due to the fact that NUKES only calculates the effects of surface blasts. Since the Trinity Test was detonated on a 30m tower, the blast calculations had to be slightly modified. After the modifications, the soil debris receipt closely compared to the actual trinitite. This data is shown in Table 8-4

Table 8-4: Table of debris composition vs crater depth. NUKES debris composition predictor based upon soil crater depth

Compound	Trinitite	NUKES Deeper Crater (NDC)	NUKES Shallow Crater (NSC)	Varying Percent (Trinitite vs. NDC)	Varying Percent (Trinitite vs. NSC)
SiO2	64.200	59.876	66.626	4.324	2.426
H2O	0.000	3.953	3.571	3.953	3.571
Al2O3	14.300	13.046	14.852	1.254	0.552
K2O	5.130	1.276	1.522	3.854	3.608
CaO	9.640	11.481	8.206	1.841	1.434
CO2	0.000	3.447	3.291	3.447	3.291
MgO	1.150	0.579	0.534	0.571	0.616
Fe2O3	0.000	0.000	0.000	0.000	0.000
FeO	1.970	0.173	0.541	1.797	1.429
Na2O	1.250	0.000	0.000	1.250	1.250
MnO	0.505	0.000	0.000	0.505	0.505
TiO2	0.427	0.000	0.000	0.427	0.427
KOH	0.000	0.000	0.000	0.000	0.000

The amount of iron, sodium, and magnesium oxide compounds significantly differ from the actual trinitite value; however, the soil algorithm that NUKES uses does not factor in the tower and other components contained in the “gadget” test; therefore, adding to the variance of composition from the actual trinitite to the NUKES output. The method discussed in Chapter 5 was developed to factor in the blast effects onto urban environments, and the corrected NUKES recipe is shown in Table 8-5. The model of the tower that was used in the NUKES code was constructed primarily from images similar to Figure 8-16.

Figure 8-16: The tower on which the gadget was placed.

Table 8-5 shows how the receipt changed based upon the soil and surrounding structures. The largest variation between Trinitite and the predicted composition from the NUKES program was in the K2O, CO2, and FeO. The K2O variation comes from the fact that NUKES used a prediction method and not the actual soil sample from the area. Although the NUKES' soil library utilized data from 4,282 soil samples, these soil samples were not collected exactly at the Trinity test site; therefore, some variation was expected. The FeO over prediction was from the fact that the actual size of steel components used to erect the tower was not known. Therefore, an over estimate of the FeO compound resulted.

Table 8-5: A molecular comparison between NUKES' deeper crater output and NUKES' shallow output with original tower modeled

Compound	Trinitite (%)	NUKES Deeper Crater (NDC) (%)	NUKES Shallow Crater with Tower (NSC) (%)	Varying Percent (Trinitite vs. NDC) (%)	Varying Percent (Trinitite vs. NSC) (%)
SiO2	64.200	60.709	64.123	3.491	0.077
Al2O3	14.300	13.880	14.612	0.420	0.312
K2O	5.130	2.109	1.755	3.021	3.375
CaO	9.640	12.314	8.201	2.674	1.439
CO2	0.000	4.280	3.509	4.280	3.509
MgO	1.150	1.412	0.802	0.262	0.348
Fe2O3	0.000	0.833	0.000	0.833	0.000
FeO	1.970	1.006	4.500	0.964	2.530
Na2O	1.250	0.833	0.980	0.417	0.270
MnO	0.505	0.833	0.463	0.328	0.042
TiO2	0.427	0.833	0.287	0.406	0.140
KOH	0.000	0.833	0.287	0.833	0.287

Conclusion

After running multiple models for different areas across the USA, it was found that the soil profile drastically changed depending upon the location of the surface burst. It is important to understand the change in elemental concentration to help update and improve upon current melt glass analysis techniques. Drastic change in elemental makeup (e.g. silicon or iron) bring along specific challenges when making synthetic melt glass and analyzing the compounds in the matrix. An accurate prediction of this composition can be made by utilizing the NUKES soil libraries and crater dimensional analysis.

The amount of urban debris that was added to the soil greatly depended upon the yield of burst and the altitude at which the burst occurred. By calculating the photon energy deposition on the face of the buildings, an accurate model was made to predict the amount of urban debris brought into the final melt glass matrix. By using a mass weight percent calculation, an accurate prediction of the soil and urban debris was made. This improved the blast progression calculations done in large urban environments and improved melt glass recipes.

Finally, the verification of NUKES or other WMD codes is challenging. There have not been any nuclear weapons that have been detonated at the surface of the earth in a dense urban environment. Therefore, comparing the predicted urban debris composition to a known composition is not possible. However, the tower that was used during the Trinity test can be used to validate the debris composition algorithm. The resulting perdition of the composition is accurate with the highest variant being less than 3.5%. By using this comparison, it can be accepted that this is an acceptable method to predict the resulting debris from a WMD detonation.

In conclusion, it has been shown that the NUKES algorithm can be used to predict urban debris composition. By developing accurate fallout composition codes, this will help to expedite analysis processes; and help predict where the large particulate fallout is dispersed. This will help shorten the collection time required for teams to find particulates that contain fragments

from the detonated weapon. This will in turn shorten the analysis time hence decreasing the required time for the USA to retaliate against potential nuclear attacks.

List of References

[1] A. Act, “One Hundred Seventh Congress of the United States of America,” *Exch. Organ. Behav. Teach. J.*, vol. H.R. 3763, p. HR 3801, 2002.

[2] A. V. Giminaro, S. A. Stratz, J. a. Gill, J. P. Auxier, C. J. Oldham, M. T. Cook, J. D. Auxier II, J. J. Molgaard, and H. L. Hall, “Compositional Planning for Development of Synthetic Urban Nuclear Melt Glass,” *Under Rev. J.Rad.Nucl.Chem.*, vol. 306, no. 1, p. 7, 2015.

[3] X. Yang, R. North, C. Romney, and P. G. Richards, “Worldwide Nuclear Explosions,” no. September 1979. Arlington, VA 22209, p. 92, 1998.

[4] G. R. Eppich, K. B. Knight, T. W. Jacomb-Hood, G. D. Spriggs, and I. D. Hutcheon, “Constraints on fallout melt glass formation from a near-surface nuclear test,” *J. Radioanal. Nucl. Chem.*, p. 17, 2014.

[5] J. J. Molgaard, J. D. Auxier II, C. J. Oldham, M. T. Cook, S. a. Young, and H. L. Hall, “Development of Synthetic Nuclear Melt Glass for Forensic Analysis,” *Submit to J. Rad. Nuc. Chem.*, 2015.

[6] B. O’Day, “ESTIMATION OF WEAPON YIELD FROM INVERSION OF DOSE RATE CONTOURS,” 2009.

[7] M. A. T. Hopkins, “DEVELOPMENT AND VALIDATION OF A NEW FALLOUT TRANSPORT METHOD USING VARIABLE SPECTRAl WINDS,” *Docorate Dissertation*. Air Force Institute of Technology, Wright-Patterson Air Force Base, Ohio, pp. 1–172, 1994.

[8] G. Sugiyama, J. Nasstrom, R. Baskett, and M. Simpson, “National Atmospheric Release Advisory Center (NARAC) Capabilities for Homeland Security,” *Llnl-Conf-425248*. Lawerence Livermore National Laboratory, p. 11, 2010.

[9] D. A. O’Brien, “Nuclear Weapon Incident and Radiological Weapon In HPAC 4.0.4.” Los Alamos, NM, p. 13, 2004.

[10] B. E. Moroz, H. L. Beck, A. Bouville, and S. L. Simon, “From Nuclear Testing Using the Noaa-Hysplit,” *Radiat. Saf. J. Heal. Phys.*, vol. 99, no. 2, pp. 1–32, 2013.

[11] J. K. Angell, D. H. Pack, L. Machta, C. R. Dickson, and W. H. Hoecker, “Three-Dimensional Air Trajectories Determined from Tetroon Flights in the Planetary Boundary Layer of the Los Angeles Basin.pdf,” *Air Resour. Lab. NOAA*, vol. 11, pp. 451–471, 1971.

[12] G. D. Rolph, F. Ngan, and R. R. Draxler, “Modeling the fallout from stabilized nuclear clouds using the HYSPLIT atmospheric dispersion model.,” *J. Environ. Radioact.*, vol. 136, pp. 41–55, 2014.

[13] A. D. Miller, “A COMPARISON IN THE ACCURACY OF MAPPING NUCLEAR FALLOUT PATTERNS USING HPAC, HYSPLIT, DELFIC FPT AND AN AFIT FORTRAN95 FALLOUT DEPOSITION CODE,” Air Force Institute of Technology, 2011.

[14] NARAC, LANL, and LLNL, “HotSpot,” 2013. .

[15] A. Bastrup-Birk, J. Brandt, and Z. Zlatev, “Real time predictions of transport, dispersion

and deposition from nuclear accidents," in *NATO Science Series*, 1st ed., vol. 57, no. 1, Denmark, 1998, pp. 53–62.

[16] S. Warner, J. F. Heagy, N. Platt, J. S. Nasstrom, and K. T. Foster, "Evaluation of Transport and Dispersion Models : A Controlled Comparison of HPAC and NARAC Predictions Form SF298 Citation Data," Livermore, CA, 2001.

[17] S. M. A. A. Hasnine, M. H. Rahman, and A. K. M. S. Islam, "Numerical Modeling of Wind effect on Plume Dispersion from a point source around Buildings," in *Proceedings of the 13th Asian Congress of Fluid Mechanics 17-21 December 2010, Dhaka, Bangladesh*, 2010, no. December, pp. 1–5.

[18] P. P. Povinec, M. Gera, K. Holý, K. Hirose, G. Lujanienė, and M. Nakano, "Dispersion of Fukushima radionuclides in the global atmosphere and the ocean," vol. 81, pp. 383–392, 2013.

[19] D. B. Smith, W. F. Cannon, L. G. Woodruff, F. Solano, J. E. Kilburn, and D. L. Fey, "Geochemical and mineralogical data for soils of the conterminous United States," p. 19, 2013.

[20] United States Department of Agriculture, "A Soil Profile," 2016. .

[21] S. Glasstone and P. J. Dolan, *The Effects of Nuclear Weapons*, Revised Ed. Washington D.C: United States Atomic Energy Commission, 1977.

[22] S. Glasstone and P. J. Dolan, "Thermal Radiation and Its Effects," *Eff. Nucl. Weapons*, pp. 276–323.

[23] C. J. Bridgman, *Introduction to the Physics of Nuclear Weapon Effects*, II., no. J. Belvoir, VA: U. S. Goverment Defense Threat Agency, 2001.

[24] U.S. Energy Information Administration, "Commercial Buildings Energy Consumption Survey (CBECS)." [Online]. Available: https://www.eia.gov/consumption/commercial/building-type-definitions.php.

[25] I. M. Lage, F. M. Abella, C. V. Herrero, J. Luis, and P. Ordóñez, "Estimation of the annual production and composition of C & D Debris in Galicia (Spain)," *Waste Manag.*, vol. 30, no. 4, pp. 636–645, 2010.

[26] F. Kleemann, J. Lederer, P. Aschenbrenner, H. Rechberger, and J. Fellner, "A method for determining buildings material composition prior to demolition," *Build. Res. Inf.*, vol. 44, no. 1, pp. 51–62, 2016.

[27] F. Kleemann, J. Lederer, P. Aschenbrenner, H. Rechberger, and J. Fellner, "A method for determining buildings' material composition prior to demolition," *Build. Res. Inf.*, vol. 3218, no. December 2014, pp. 1–12, 2014.

[28] F. Kleemann, J. Lederer, P. Aschenbrenner, H. Rechberger, J. Fellner, F. Kleemann, J. Lederer, P. Aschenbrenner, H. Rechberger, and J. Fellner, "A method for determining buildings ' material composition prior to demolition RESEARCH PAPER A method for

determining buildings ' material composition prior to demolition," vol. 3218, no. October, 2016.

[29] P. Villoria, R. Merino, A. S. González, and C. Porras-amores, "Resources , Conservation and Recycling Best practice measures assessment for construction and demolition waste management in building constructions," "*Resources, Conserv. Recycl.*, vol. 75, pp. 52–62, 2013.

[30] K. Cochran and T. Townsend, "Estimation of regional building-related C & D debris generation and composition : Case study for Florida , US," vol. 27, pp. 921–931, 2007.

[31] K. M. Cochran and T. G. Townsend, "Estimating construction and demolition debris generation using a materials flow analysis approach," *Waste Manag.*, vol. 30, no. 11, pp. 2247–2254, 2010.

[32] L. W. Cheah and J. B. Heywood, "Cars on a Diet : The Material and Energy Impacts of Passenger Vehicle Weight Reduction in the U . S .," 2010.

[33] "The City of New York Zola Zoning and Land Use." [Online]. Available: http://maps.nyc.gov/doitt/nycitymap/template?applicationName=ZOLA.

[34] "City of Houston's Planning and Development Department Loop 610 land Use." [Online]. Available: http://www.houstontx.gov/planning/Demographics/Loop610Website/landuse.html. .

[35] T. Lindeberg, "Edge Detection and Redge Detection with automatic scale selection," *Int. J. Comput. Vis.*, vol. 30, no. 2, pp. 117–154, 1998.

[36] J. P. Grotzinger, J. Crisp, A. R. Vasavada, R. C. Anderson, C. J. Baker, R. Barry, D. F. Blake, P. Conrad, K. S. Edgett, B. Ferdowski, R. Gellert, J. B. Gilbert, M. Golombek, J. Gómez-Elvira, D. M. Hassler, L. Jandura, M. Litvak, P. Mahaffy, J. Maki, M. Meyer, M. C. Malin, I. Mitrofanov, J. J. Simmonds, D. Vaniman, R. V. Welch, and R. C. Wiens, *Mars Science Laboratory Mission and Science Investigation*, vol. 170, no. 1–4. 2012.

[37] H. G. Barrow and J. M. Tenenbaum, "Interpreting line drawings as three-dimensional surfaces," *Artif. Intell.*, vol. 17, no. 1–3, pp. 75–116, 1981.

[38] S. E. Umbaugh, *Digital Image Processing and Analysis: Human and Computer Vision Applications with CVIPtools*, 2nd ed. Boca Raton, FL: CRC Press, 2010.

Appendix

This appendix contains the NUKES code and all its components.

```
% NUKES(Y,Lat,Lon)
%% Jerrad P. Auxier
% Diseration code Part 1
% Started November 5, 2015
% This portion of the code will be the GUI Interface
% which will ask the user for both the yeild and location of the weapon.
% The code will then calculate the blast sizes for weapons and crater size
% formed. Then it will use the coordinates given by the user to analyze the
% soil.
clc
clear all
close all

%% User Input via GUI interface and read data in from Excel================

yield=20; % This is the size of the weapon (kt)
lat = 40.709351; %Will have to look into better editing of this portion For
NYC 40.709351
lon = -74.010408; %See previous comment For NYC -74.010408
max_min=0.55;


%% Bomb Size and Calculations==============================================
% The portion of this code will allow the user to select the type of soil
% located near ground zero. It will calculate the crater depth and crater
% radius. I need to check on the densities of different soils to insure
accurate
% mass composition

FBR = (90*(yield^0.4)).*0.3048;
% Prints it out Fireball blast radius in meters
FBBR = 145*(yield^0.4).*0.3048;
% Prints fireball blast break-away radius out in meters
% and this will be the radius used for calculations.
FBBD = FBBR*2;
FBBRM = FBBR.*2; % According to glasstone, the fireball at max is
% twice the size of the break away radius.

soil = menu('Choose Soil Type','Dry Soil (Dry Soft Rock)','Wet Soil (Wet Soft
Rock)','Dry Hard Rock','Wet Hard Rock');
if soil==1 % For dry soil density is assumed to be 1348.23 kg/m^3
    R_ap = 61;
    %R_ap is the appearent radius of the crater. This is beacuse of the
fallback
    D_ap = 31;
    %D_ap is the appearent depth of the crater. This is beacuse of the
fallback
    R_a = R_ap*(yield^0.3).*0.3048;
    %R_a is the actual radius not including fall back
    D_a = D_ap*(yield^0.3).*0.3048;
    % Both are in meters
    Crater_V = (1./3).*(pi*(R_a^2)*D_a);
    % This will result in m^3
```

```
    Soil_M = 1348.23*Crater_V;
    %This result is in kg
elseif soil==2 %For wet soil density if assumed to be 1601.85 kg/m^3
    R_a = 82*(yield^0.3).*0.3048;
    D_a = 31*(yield^0.3).*0.3048;
    % Both are in meters
    Crater_V = (pi*(R_a^2)*D_a)/3;
    % This will result in m^3
    Soil_M = 1601.85*Crater_V;
    % THis will result in kg
elseif soil==3 %For hard rock density is assumed to be 3203.69kg/m^3
    R_a = 49*(yield^0.3).*0.3048;
    D_a = 22*(yield^0.3).*0.3048;
    % Both are in meters
    Crater_V = (pi*(R_a^2)*D_a)/3;
    % This will result in ft^3
    Soil_M = 3203.69*Crater_V;
    %This will result in kg
elseif soil==4 %For wet hard rock density is assumed to be 2402.77kg/m^3
    R_a = 58*(yield^0.3).*0.3048;
    D_a = 28*(yield^0.3).*0.3048;
    % Both are in meters
    Crater_V = (pi*(R_a^2)*D_a)/3;
    % This will result in ft^3
    Soil_M = 2402.77*Crater_V;
    %This will result in kg
end
NUKES_Elements(lat,lon,yield,max_min,D_a,FBBRM);
%% This will give the ejecta qulatiies for the code. This will help us
understand
% where the large projectile is sent

R_e=2.15*R_a; % already in meters

% Radius of ejecta from crater, this will give an idea of where large
% particles are sent
% Output of Blast in an Excel File. Hopefully all data will be put out on
% one excel file.
A = {'Crater Radius(m)','Crater Depth(m)','Crater Volume(m^3)','Soil
Mass(kg)',...
'Uninhibited Fireball Break Away Radius (m)','Radius of Ejecta (m)'...
;R_a,D_a,Crater_V,Soil_M,FBBR,R_e};
delete('C:\Users\Jerrad Auxier\Documents\Documents\Jerrads Stuff\Grad
School\Research\PhD Project\Blast Effect Code\Results\Crater
Dimensions.xlsx');
xlswrite('C:\Users\Jerrad Auxier\Documents\Documents\Jerrads Stuff\Grad
School\Research\PhD Project\Blast Effect Code\Results\Crater
Dimensions.xlsx',A);




%% Portray Actually Blast Radius and Crater Dimensions on Map
% The goal of this section is to print out a 3-d shape of the fireball
```

```
% and the crater size. This will help give an idea of comparison to
% size of buildings


%% This will hopefulley print out a google image of the area
%ge_test1
out=menu('Choose NUKES Output method','Google Earth Image','Matlab Code
Output','Both Options');
hold on
if out==1
    NUKES_GE_OUT(lat,lon,FBBRM);
elseif out==2
    %% THis will print out a 3-D image of the the fireball dimensions
    x=linspace(-pi./2,pi./2);
    [X1,Y1]=meshgrid(x);
    XA = FBBRM.*cos(X1).*sin(Y1);
    YA = FBBRM.*sin(X1).*sin(Y1);
    ZA = FBBRM.*cos(Y1); % Beacuse the fireball can be assumed to be
spherical
    %it will be assumer the hieght is the same as FBBRM
    %contour3(XA,YA,ZA,100); % Plots a 3-D contour plot
    contour3(XA,YA,ZA,50); % Plots a 3-D surface
    %% This will print out a 3-D image of the crater dimensions

    x=linspace(-pi./2,pi./2);
    [X1,Y1]=meshgrid(x);
    X_C = R_a.*cos(X1).*sin(Y1);
    Y_C = R_a.*sin(X1).*sin(Y1);
    Z_C = -D_a.*cos(Y1);
    contour3(X_C,Y_C,Z_C,100);% Plots a 3-D contour plot
    % surf(X_C,Y_C,Z_C);      %Plots a 3-D surface

    %% Now generate the X Y plane to show the ground. After fixing the
shading
    % I also need to add a time step so the wave is shown propagating
outward.
    Bound = linspace(-FBBRM*1.25,FBBRM*1.25); % Creates the ground boundary
    [X3,Y3] = meshgrid(Bound); % Creates the ground boundary
    a=0; b=0; d=0; Z=(d - a * X3 - b * Y3); % Creates the plane for the
ground
    [ground]=imread('Ground.jpg'); %Uploads the image data from google
    surf(X3,Y3,Z,ground,'edgecolor', 'none','FaceColor','texturemap')
    xlabel('x(m)'); ylabel('y(m)'); zlabel('z(m)')
else
    NUKES_GE_OUT(lat,lon,FBBRM)
 %% THis will print out a 3-D image of the the fireball dimensions
    x=linspace(-pi./2,pi./2);
    [X1,Y1]=meshgrid(x);
    XA = FBBRM.*cos(X1).*sin(Y1);
    YA = FBBRM.*sin(X1).*sin(Y1);
    ZA = FBBRM.*cos(Y1); % Beacuse the fireball can be assumed to be
spherical
    %it will be assumer the hieght is the same as FBBRM
    %contour3(XA,YA,ZA,100); % Plots a 3-D contour plot
    contour3(XA,YA,ZA,50); % Plots a 3-D surface
    %% This will print out a 3-D image of the crater dimensions
```

```
    x=linspace(-pi./2,pi./2);
    [X1,Y1]=meshgrid(x);
    X_C = R_a.*cos(X1).*sin(Y1);
    Y_C = R_a.*sin(X1).*sin(Y1);
    Z_C = -D_a.*cos(Y1);
    contour3(X_C,Y_C,Z_C,100);% Plots a 3-D contour plot
    % surf(X_C,Y_C,Z_C);      %Plots a 3-D surface

    %% Now generate the X Y plane to show the ground. After fixing the
shading
    % I also need to add a time step so the wave is shown propagating
outward.
    Bound = linspace(-FBBRM*1.25,FBBRM*1.25); % Creates the ground boundary
    [X3,Y3] = meshgrid(Bound); % Creates the ground boundary
    a=0; b=0; d=0; Z=(d - a * X3 - b * Y3); % Creates the plane for the
ground
    [ground]=imread('Ground.jpg'); %Uploads the image data from google
    surf(X3,Y3,Z,ground,'edgecolor', 'none','FaceColor','texturemap')
    xlabel('x(m)'); ylabel('y(m)'); zlabel('z(m)')
end

clear data B_l B_w_a B_H B_w inp Dif x2 y2 z2
[imageTest]=imread('brick.jpg');
    hold on
    grid on
%% This part of the code will load the building library and elemental
%   properties. It will also read in building locations and dimensions.
NUKES_Input = xlsread('C:\Users\Jerrad Auxier\Documents\Documents\Jerrads
Stuff\Grad School\Research\PhD Project\Blast Effect Code\NUKES_inp.xlsx');
% Excel Input Deck Format       BT X    Y   L   W   H
build_comp = xlsread('C:\Users\Jerrad Auxier\Documents\Documents\Jerrads
Stuff\Grad School\Research\PhD Project\Blast Effect Code\Soil
Library\NUKES_Build.xlsx');
build_prop = xlsread('C:\Users\Jerrad Auxier\Documents\Documents\Jerrads
Stuff\Grad School\Research\PhD Project\Blast Effect Code\Soil
Library\NUKES_Build_Prop.xlsx');

%% This is a sample matrix for trouble shooting
    % NUKES_Input = [ 50 150 randi([25,300]) 25 50
    %          -50 50 randi([25,300]) 10 10
    %          50 -50 randi([25,300]) 10 10
    %          -50 -50 randi([25,300]) 10 10];

%% Analysis of all the data in the excel sheets and creates 3-D visualition
for i=1:length(NUKES_Input(:,1))
% So I want to read in the general information from the excel sheet
    clear x2 y2 z2 L W
    % I want to clear all variables so the code runs better
    X_cor = NUKES_Input(i,2);
    Y_cor = NUKES_Input(i,3);
    L = NUKES_Input(i,4);
    W = NUKES_Input(i,5);
    B_H = NUKES_Input(i,6);
if X_cor<0 && Y_cor<0 % Both are negative values for buildings
    X_left  = X_cor-L/2; % Defining the left x boundary
```

```
    X_right = X_cor+L/2; % Defining the right x boundary
    inp_x = linspace(X_left,X_right);
    Y_down = Y_cor-W/2;
    Y_up = Y_cor+W/2;
    inp_y = linspace(Y_down,Y_up);
    [x2,y2] = meshgrid(inp_x,inp_y);
    Dif = length(inp_y);
elseif X_cor>=0 && Y_cor>=0 % Both are positive values for buildings
    X_left  = X_cor-L/2; % Defining the left x boundary
    X_right = X_cor+L/2; % Defining the right x boundary
    inp_x = linspace(X_left,X_right);
    Y_down = Y_cor-W/2;
    Y_up = Y_cor+W/2;
    inp_y = linspace(Y_down,Y_up);
    [x2,y2] = meshgrid(inp_x,inp_y);
    Dif = length(inp_y);
elseif X_cor>0 && Y_cor<0 % For positive x value and negative y value
    X_left  = X_cor-L/2; % Defining the left x boundary
    X_right = X_cor+L/2; % Defining the right x boundary
    inp_x = linspace(X_left,X_right);
    Y_down = Y_cor-W/2;
    Y_up = Y_cor+W/2;
    inp_y = linspace(Y_down,Y_up);
    [x2,y2] = meshgrid(inp_x,inp_y);
    Dif = length(inp_y);
elseif X_cor<0 && Y_cor>0 % For negative x vaule and positive y value
   X_left  = X_cor-L/2; % Defining the left x boundary
    X_right = X_cor+L/2; % Defining the right x boundary
    inp_x = linspace(X_left,X_right);
    Y_down = Y_cor-W/2;
    Y_up = Y_cor+W/2;
    inp_y = linspace(Y_down,Y_up);
    [x2,y2] = meshgrid(inp_x,inp_y);
    Dif = length(inp_y);
end
for R2=1:Dif; % This if loop creates the edges of the buildings
     for C2=1:Dif;
    if R2==1 || R2==Dif
        z2(R2,C2)=0.5;
    elseif C2==1 || C2==Dif
        z2(R2,C2)=0.5;
    else
        z2(R2,C2)=B_H;
    end
    end
end
        surf(x2,y2,z2,imageTest,'edgecolor', 'none','FaceColor','texturemap')
end
xlabel('X distance (m)')
ylabel('Y distance (m)')

%% Library of Building Composition materials
% This is where I format the Excel File Input into various matricies
% I need a Construction Material, Composition Matrix, and Elemental Matrix
```

```
%% Mass and Fracition Calculations
% This is where I calculate the amount of material that each building holds
% and its addition to the fireball

%% Building Energy Deposition Calculations
% 1) Know surface area covered by FBBRM
% 2) Know surface area covered by types of buildings
% 3) Determine mass of everything to find out mass ratio (input density of
% soil)
% 4) Create building libraires
%SAFB=pi.*(FBBRM^2); %Surface area of Fireball at max radius in m^2
```

NUKES_Elements

This portion of the appendix refers for the portion of the NUKES code that brings in the soil data and does crater calculations.

```
function NUKES_Elements(lat,lon,yield,max_min,D_a,FBBRM)
%% This code will utilize the soil data compiled to determine the
% the elemental print out of the soil. This code also contains the
% the soil horizon data to detemine which horizon to look at.

lat_min = lat-max_min;
lat_max = lat+max_min;
lon_min = lon-max_min;
lon_max = lon+max_min;

%% Reads in the XLS file from Excel
a_hor = xlsread('C:\Users\Jerrad Auxier\Documents\Documents\Jerrads
Stuff\Grad School\Research\PhD Project\Blast Effect Code\Soil
Library\a_horizon.xls');
c_hor = xlsread('C:\Users\Jerrad Auxier\Documents\Documents\Jerrads
Stuff\Grad School\Research\PhD Project\Blast Effect Code\Soil
Library\c_horizon.xls');
[ele_data_e, text_e, ele] = xlsread('C:\Users\Jerrad
Auxier\Documents\Documents\Jerrads Stuff\Grad School\Research\PhD
Project\Blast Effect Code\Soil Library\Elements.xls');
[ele_data_c, text_c, ele_c] =xlsread('C:\Users\Jerrad
Auxier\Documents\Documents\Jerrads Stuff\Grad School\Research\PhD
Project\Blast Effect Code\Soil Library\Composition.xlsx');
lat_d = a_hor(:,4);
lon_d = a_hor(:,5);

%% Now read soil data from Excel Sheet for coordinates close to the lat
% and lon specified.=========================================================
k=1;
if length(c_hor)==length(a_hor)
for i=1:length(a_hor)
 if lat_min<=a_hor(i,4) && a_hor(i,4)<=lat_max
    if lon_min<=a_hor(i,5) && a_hor(i,5)<=lon_max
        soil_dat_a(k,:)= a_hor(i,:);
    end
```

```
 end
 if lat_min<=c_hor(i,4) && c_hor(i,4)<=lat_max
    if lon_min<=c_hor(i,5) && c_hor(i,5)<=lon_max
        soil_dat_c(k,:)= c_hor(i,:);
        k=1+k;
    end
 end
end
else
    printf('Error')
end
soil_wt_a = soil_dat_a(:,10:35);
%Concolidating the evaluated data into one matrix
soil_wt_c = soil_dat_c(:,10:35);
% Concolidating the evaluated data into one matrix

%% Testing to see what soil matrix is more accurate
% No average between the size of the crater. We will use a volume ratio
% to calculate the weighted average.
%ave_wt = 1.*(mean(soil_wt_c)) + (0*mean(soil_wt_a));
% Vol_A= pi*(FBBRM^2)*0.150;
% Vol_C= (1/2)*pi*(FBBRM^2)*((D_a-0.150)/3);
% Ave_hora = Vol_A/Vol_C;
% Ave_horc = 1-Vol_A/Vol_C;
% % Average between A and C horizon.
% ave_wt = (Ave_horc.*(mean(soil_wt_c))) + (Ave_hora.*mean(soil_wt_a));
ave_wt = (0.1.*(mean(soil_wt_c))) + (0.9.*mean(soil_wt_a));
%Assume A goes from 0-20cm, and C goes from 20-100cm
%% Creating a structure martrix to of the different types of minerals
mineral = {'SiO2','KAlSi3O8','CaAl2Si2O8','Total_Fs',...
    'MgFe2Al2Si24O10(OH)2·4H2O',...
    'KMgFeAl2Si2O10H2O','Al2Si2O5(OH)4','Total_Clay','Al(OH)3',...
    'CaCO3','CaMg(CO3)2','CaCO3','Total_Carbonite',...
    'NaAlSi2O6','Ca2Al4Si14O36*12H2O','Total_ZEO',...
    'CaSO4','Mg3Si4O10(OH)2','Ca2Mg4Al2Si7O22(OH)2',...
    'Mg3Si2O5(OH)4','Fe2O3','FeO(OH)','pyroxene',...
    'FeS2','other','amorphous'};
%% Create a matrix with Average Minerals
%% A program to print out minerals that are greater than 0
j=1;
for i=1:length(ave_wt)
if ave_wt(1,i)>0
    C1(1,j) = mineral(1,i);
    C1(2,j) = num2cell(ave_wt(1,i));
    j=j+1;
end
end
C1=C1';
close
delete('C:\Users\Jerrad Auxier\Documents\Documents\Jerrads Stuff\Grad
School\Research\PhD Project\Blast Effect Code\Results\Minerals.xlsx');
xlswrite('C:\Users\Jerrad Auxier\Documents\Documents\Jerrads Stuff\Grad
School\Research\PhD Project\Blast Effect Code\Results\Minerals.xlsx',C1);
%% Create a matrix with Average elemtents of soil and mineral name

for i=1:length(ave_wt)
```

```
   E(i,:)=ele_data_e(i,:).*ave_wt(1,i)/100; % Creates a elemental matrix
end
%% Now create a matrix that prints out the elemental fractions
E=sum(E);
x=1;
for i=1:length(E);
if E(1,i)>0
    element(1,x)=text_e(1,i+1);
    element(2,x) = num2cell(E(1,i));
    x=x+1;
end
end
delete('C:\Users\Jerrad Auxier\Documents\Documents\Jerrads Stuff\Grad
School\Research\PhD Project\Blast Effect Code\Results\Elemental.xlsx');
xlswrite('C:\Users\Jerrad Auxier\Documents\Documents\Jerrads Stuff\Grad
School\Research\PhD Project\Blast Effect
Code\Results\Elemental.xlsx',element');

%% Creat the composition matrix

for i=1:length(ave_wt)
   C(i,:)=ele_data_c(i,:).*ave_wt(1,i)/100; % Creates a elemental matrix
end
%% Now create a matrix that prints out the composition fractions
C=sum(C);
x=1;
for i=1:length(C);
if C(1,i)>0
    comp(1,x)=text_c(1,i+1);
    comp(2,x) = num2cell(C(1,i));
    x=x+1;
end
end

delete('C:\Users\Jerrad Auxier\Documents\Documents\Jerrads Stuff\Grad
School\Research\PhD Project\Blast Effect Code\Results\Composition.xlsx');
xlswrite('C:\Users\Jerrad Auxier\Documents\Documents\Jerrads Stuff\Grad
School\Research\PhD Project\Blast Effect
Code\Results\Composition.xlsx',comp');
```

NUKES_GE_Out

This portion of the code shows the portion of the code that interfaces with Google Earth to display the blast propagation.

```
function NUKES_GE_OUT(lat,lon,FBBRM)
run('C:\Users\Jerrad Auxier\Documents\Documents\Jerrads Stuff\Grad
School\Research\PhD Project\Blast Effect
Code\Open_Earth\matlab\oetsettings.m')
%x=linspace(1,2);
%x=linspace(-pi./2,pi./2); % Creates a 100 evenly spaced matrix between two
values
x=linspace((-pi./2),(pi./2));
y=linspace((-pi./2),(pi./2));
[X1,Y1]=meshgrid(x,y);
```

```
%[X1,Y1]=meshgrid(x); % creates a rectangle for the plotting
XA = lat+(FBBRM*0.0000155*(cos(X1).*sin(Y1))); %for NYC 40.709351
YA = lon+(FBBRM*0.0000159*(sin(X1).*sin(Y1))); % for NYC -74.010408
ZA = FBBRM*.320529.*cos(Y1); %The tower One Chase Mahattan Plaza 813-foot-
tall tower
% OPT = KMLcontour3;
% OPT.zScaleFun   = @(ZA) (ZA+1)*2000;
% KMLcontour3(XA,YA,ZA+10,OPT)
KMLsurf(XA,YA,ZA,'fileName','NUKES_Blast2.kml','zScaleFun',@(z) z);


% z = sin(x1);
% z1 = sin(y1);
% contour3(x1,y1,z,100)
% colormap bone
% hold on
% contour3(x1,y1,z1,100)
% colormap hsv
```

NUKES_Build_Comp

This portion of the appendix shows the portion of the NUKES code that models building data and blast calculations.

```
% function NUKES_Build_Comp

clear data B_l B_w_a B_H B_w inp Dif x2 y2 z2
[imageTest]=imread('brick.jpg');
    hold on
    grid on
%% This part of the code will load the building library and elemental
%   properties. It will also read in building locations and dimensions.
NUKES_Input = xlsread('C:\Users\Jerrad Auxier\Documents\Documents\Jerrads
Stuff\Grad School\Research\PhD Project\Blast Effect Code\NUKES_inp.xlsx');
% Excel Input Deck Format       BT X    Y   L   W   H
build_comp = xlsread('C:\Users\Jerrad Auxier\Documents\Documents\Jerrads
Stuff\Grad School\Research\PhD Project\Blast Effect Code\Soil
Library\NUKES_Build.xlsx');
build_prop = xlsread('C:\Users\Jerrad Auxier\Documents\Documents\Jerrads
Stuff\Grad School\Research\PhD Project\Blast Effect Code\Soil
Library\NUKES_Build_Prop.xlsx');

%% This is a sample matrix for trouble shooting
    % NUKES_Input = [ 50 150 randi([25,300]) 25 50
    %          -50 50 randi([25,300]) 10 10
    %          50 -50 randi([25,300]) 10 10
    %          -50 -50 randi([25,300]) 10 10];

%% Analysis of all the data in the excel sheets and creates 3-D visualition
for i=1:length(NUKES_Input(:,1))
% So I want to read in the general information from the excel sheet
    clear x2 y2 z2 L W
    % I want to clear all variables so the code runs better
    X_cor = NUKES_Input(i,2);
```

```
    Y_cor = NUKES_Input(i,3);
    L = NUKES_Input(i,4);
    W = NUKES_Input(i,5);
    B_H = NUKES_Input(i,6);
if X_cor<0 && Y_cor<0 % Both are negative values for buildings
    X_left  = X_cor-L/2; % Defining the left x boundary
    X_right = X_cor+L/2; % Defining the right x boundary
    inp_x = linspace(X_left,X_right);
    Y_down = Y_cor-W/2;
    Y_up = Y_cor+W/2;
    inp_y = linspace(Y_down,Y_up);
    [x2,y2] = meshgrid(inp_x,inp_y);
    Dif = length(inp_y);
elseif X_cor>=0 && Y_cor>=0 % Both are positive values for buildings
    X_left  = X_cor-L/2; % Defining the left x boundary
    X_right = X_cor+L/2; % Defining the right x boundary
    inp_x = linspace(X_left,X_right);
    Y_down = Y_cor-W/2;
    Y_up = Y_cor+W/2;
    inp_y = linspace(Y_down,Y_up);
    [x2,y2] = meshgrid(inp_x,inp_y);
    Dif = length(inp_y);
elseif X_cor>0 && Y_cor<0 % For positive x value and negative y value
    X_left  = X_cor-L/2; % Defining the left x boundary
    X_right = X_cor+L/2; % Defining the right x boundary
    inp_x = linspace(X_left,X_right);
    Y_down = Y_cor-W/2;
    Y_up = Y_cor+W/2;
    inp_y = linspace(Y_down,Y_up);
    [x2,y2] = meshgrid(inp_x,inp_y);
    Dif = length(inp_y);
elseif X_cor<0 && Y_cor>0 % For negative x vaule and positive y value
   X_left  = X_cor-L/2; % Defining the left x boundary
    X_right = X_cor+L/2; % Defining the right x boundary
    inp_x = linspace(X_left,X_right);
    Y_down = Y_cor-W/2;
    Y_up = Y_cor+W/2;
    inp_y = linspace(Y_down,Y_up);
    [x2,y2] = meshgrid(inp_x,inp_y);
    Dif = length(inp_y);
end
for R2=1:Dif; % This if loop creates the edges of the buildings
     for C2=1:Dif;
    if R2==1 || R2==Dif
        z2(R2,C2)=0.5;
    elseif C2==1 || C2==Dif
        z2(R2,C2)=0.5;
    else
        z2(R2,C2)=B_H;
    end
    end
end
        surf(x2,y2,z2,imageTest,'edgecolor', 'none','FaceColor','texturemap')
end
xlabel('X distance (m)')
ylabel('Y distance (m)')
```

```
%% Library of Building Composition materials
% This is where I format the Excel File Input into various matricies
% I need a Construction Material, Composition Matrix, and Elemental Matrix



%% Mass and Fracition Calculations
% This is where I calculate the amount of material that each building holds
% and its addition to the fireball

%% Building Energy Deposition Calculations
% 1) Know surface area covered by FBBRM
% 2) Know surface area covered by types of buildings
% 3) Determine mass of everything to find out mass ratio (input density of
% soil)
% 4) Create building libraires
%SAFB=pi.*(FBBRM^2); %Surface area of Fireball at max radius in m^2
```

Vita

Jerrad Auxier was born in Aurora, CO to the parents of John and Ruby Auxier. He is the youngest of three siblings: John and Susanne. He was homeschooled until he reached high school, in which he began to attend Northern New Mexico College. He completed his associates degree in science from Northern New Mexico College, and moved to the University of Tennessee, Knoxville to pursue his bachelor's degree. Jerrad completed his bachelor's degree in Nuclear Engineering in May of 2013, and began graduate school at UTK in June. He received his masters degree from UTK in Nuclear Engineering, and began a post-masters position at Los Alamos National Laboratory. While at Los Alamos National Laboratory, he worked in the Applied Engineering and Technology group studying criticality curves for varying compositions of plutonium. This opportunity helped him develop his doctorates project on developing high fidelity models for post-detonation nuclear debris. He completed his PhD in May of 2017 and is planning on working at Los Alamos National Laboratory as a post-doc.